The Dissertation Committee for Dan Wang
certifies that this is the approved version of the following dissertation:

Real-time 3D Visualization of Organ Deformations Based on Structured Dictionary

Committee:

Ahmed H. Tewfik, Supervisor

Alan Bovik

Constantine Caramanis

Mia K. Markey

Stanislav Emelianov

James W. Tunnell

Real-time 3D Visualization of Organ Deformations Based on Structured Dictionary

by

Dan Wang, B.E., M.E., M.S.

DISSERTATION

Presented to the Faculty of the Graduate School of

The University of Texas at Austin

in Partial Fulfillment

of the Requirements

for the Degree of

DOCTOR OF PHILOSOPHY

THE UNIVERSITY OF TEXAS AT AUSTIN

May 2012

Dedicated to my family.

Acknowledgements

Over the last four years, I have had the privilege to work with a number of great people who have made my time during the PhD study enjoyable and rewarding. I'd like to take this opportunity to recognize them. Without them this dissertation would not be possible.

I am deeply grateful to my advisor, Prof. Ahmed Tewfik, for all his help and guidance during my Ph.D study. Dr. Tewfik is an outstanding signal processing expert with broad knowledge, sharp intuition, and grand vision. Dr. Tewfik is also a great mentor. He inspired me to be innovative and taught me how to be an efficient researcher. Thanks to his guidance, I experienced a great Ph.D journey which is made up of finding valuable problems, investigating innovative ideas and convincing yourself about the idea. His inspiration and warm personality have won my highest respect and trust.

I am extremely thankful for the time and invaluable advice from my committee members: Prof. Alan Bovik, Prof. Constantine Caramanis, Prof. Mia K. Markey, Prof. Stanislav Emelianov and Prof. James W. Tunnell. In addition, I would also like to thank Prof. Emad Ebbini, Prof. Mostafa Kaveh, Prof. Gerald Timm and Dr. Timothy Kinney from University of Minnesota for their help and advice during my study in UofM.

I would like to thank all my labmates in Minnesota and Austin, including Yingchun Zhang, Yunhe Shen, Vimal Singh, Youngchun Kim, Yingxi Liu, Vijay Tadipatri, Nikhil Kundargi, Neeraj Gaur, Rahul Iyer and Cheol-Hong Ming for their collaboration as colleagues and good memories as friends.

Life while studying abroad was not easy. I am so glad to have great friends who gave me company when I am feel lonely and homesick. Special thanks to Jingxue Lu, Beiyu Rong,

Yu Wang, Guojin He and Jie Yang. Gratitude to Ping Xia, Chao Chen, Jing Lin, Zheng Lv, Xun Cao, Hongbo Si, Nan Sun, Xiaohu Shen and Yuhuan Du.

Most importantly, none of this would have been possible without the constant source of encouragement and good advice from my family. I am deeply indebted to them for all the courage, strength and love they give me. I would like to thank my husband, Ziguo, who has shared with me all the sweet and bitterness of life in US. Without his trust and encouragement, I would have failed during the pursuit of my Ph.D degree. I feel so thankful to have him in my life.

Real-time 3D Visualization of Organ Deformations Based on Structured Dictionary

Publication No. _____

Dan Wang, Ph.D.
The University of Texas at Austin, 2012

Supervisor: Ahmed H. Tewfik

Minimally invasive technique (MIS) revolutionized the field of surgery for its shorter hospitalization time, lower complication rates, and ultimately reduced morbidity and mortality. However, one of the critical challenges that prevent it from reaching the full potentials is the restricted visualization from the traditional monocular camera systems at the presence of tissue deformations.

This dissertation aims to design a new approach which can provide the surgeons with real time 3D visualization of complete organ deformations during the MIS operation. This new approach even allows the surgeon to see through the wall of an organ rather than just looking at its surface. The proposed design consists of two stages. The first training stage identified the deformation subspaces from a training data set in the transformed spherical harmonic domain, such that each surface can be sparsely represented in the structured dictionary with low dimensionality. This novel idea is based on our experimental discovery that the spherical harmonic coefficients of any organ surface lie in specific low dimensional subspaces. The second reconstruction stage reconstructs the complete deformations in real-time using surface samples obtained with an optical device from a limited field of view while applying the structured dictionary.

The sparse surface representation algorithm is also applied to ultrasound image enhancement and efficient surgical simulation. The former is achieved by fusing ultrasound samples with optical data under proper weighting strategies. The high speed of surgical simulation

is obtained by decreasing the computational cost based on the high compactness of the surface representation algorithm.

In order to verify the proposed approaches, we first use the computer models to demonstrate that the proposed approach matches the accuracy of complex mathematical modeling techniques. Then ex-vivo experiments are conducted on freshly excised porcine kidneys utilizing a 3D MRI machine, a 3D optical device and an ultrasound machine to further test the feasibility under practical settings.

Contents

List of Tables

List of Figures

Chapter 1

Introduction

Along with the fast development of medical devices and personal computers, the recent two decades witnessed a rapid proliferation of Minimally Invasive Surgery (MIS) procedures and biopsies such as single-port laparoscopy and Natural Orifice Translumenal Endoscopic Surgery (NOTES) [1]. Single port procedures use a single small incision, and NOTES involves approaching the abdominal cavity (or other body cavities) through natural orifices such as the mouth or vagina using a flexible endoscope, without creating an incision on the abdominal wall. These MIS procedures show great promise for shorter hospitalization time, lower complication rates, and ultimately reduced morbidity and mortality from surgery. However, several challenges prevent these new approaches from reaching their full potentials. These challenges include limited visualization area, accurately tracking the instrument locations during the surgery, interpreting images from different modalities without ambiguity, high speed visualization of large amount image data, soft tissue deformation, among others [1]. This thesis focuses on the issue of restricted visualization of the surgical field at the presence of tissue deformations and also briefly touch on the topic of surgical simulation.

Successful MIS operations require clear visual feedback of the surgical scene and the instrument location and orientation to support the localization of anatomical targets, observation of critical structures and sparing healthy tissue. During an open procedure, the

surgeon can view the surgical field from different angles and perspectives and the haptic feedback provides a mental 3D image. Unfortunately, the flexible probes used in MIS procedures have limited visible angles due to the small incision size, which leads to the restricted visualization issue faced by the surgeons. Moreover, the flexibility of the endoscope further complicates the understanding of its distal orientation, so it becomes difficult to accurately locate the endoscope tip relative to nearby anatomic structures for safe operations. In this thesis, we tackle the restricted visualization problem by applying the advantages of sparse surface representation in a structured dictionary. In particular, we address the issues of real-time 3D visualization of organ deformations and intraoperative ultrasound image enhancement during MIS operations based on the technique of structured signal representation. The ultimate aim is to enhance the image-guided therapy by offering the MIS surgeons with a large field of view of the surgical field while deformations are reconstructed using limited data. This approach does not require additional incisions and multiple abdominal ports for inserting extra laparoscopic cameras. In addition, we propose to employ the structured representation technique to achieve real-time surgical simulation with high realism, in the hope of enriching the surgical training resources.

1.1 Research Motivations

Different imaging based visualization systems have been designed to provide invaluable assistance during the MIS procedures. Each technique plays different role during MIS operations according to its characteristics.

The preoperative computed tomography(CT) and magnetic resonance imaging(MRI) can not only be used for diagnosis but also provide pathoanatomical information and augment the surgeon's spatial orientation. However, preoperative imaging does not solve the restricted visualization problem in MIS surgery since the actual intraoperative scene differs from the preoperative imagery due to several factors, including patient positioning, gas insufflation to create a working space, tool-tissue interaction, and body movements such as

breathing and heart beat.

On the other hand, intraoperative image-guided systems [9]-[30][45]-[64] provide real-time information on spatial positioning and orientation as well as assistance with the identification of anatomy and localization of pathology. The imaging modalities can be ultrasound, CT, MRI or a combination of these modalities. Each modality has its strengths and weaknesses in terms of image acquisition quality, speed, visibility/access restriction and potential negative effects on the patient's health. For example, Intraoperative Ultrasound (IOUS) has merits of safe usage, low cost and high flexibility but suffers from limited field of view and relatively low image quality. Though promising, current intraoperative visualization systems are mostly used in rigid organ interventions, e.g., neurosurgery, otolaryngology, spine, and orthopedic procedures. They do not meet the requirements of high resolution, real-time, 3D visualization simultaneously, to support the recognition of anatomic structures and accurate instrument localization and orientation for safe abdominal MIS procedures [80, 81, 82]. To become widespread in intra-abdominal procedures, advances that will allow systems to adapt to moving and deforming anatomy are also needed.

Modeling approaches [65]-[76] have also been used to track organ deformation and correct preoperative imagery or intraoperative imagery between successive scans. Those method incorporate a patient-specific model to the image system, such that the preoperative image can be warped according to the estimated deformation based on the partial intraoperative data. Most modeling approaches are intrusive and computationally expensive to meet the real-time tracking requirement. To alleviate computational cost, systems typically use simpler but less accurate mathematical models, leading to reduced accuracy and resolution that is inadequate for safe surgical interventions. Therefore, deformation modeling is still in infancy for integration into a real image-guided system.

Shifting to the signal processing community, we notice that sparse signal representation have gained tremendous attentions in applications such as signal compression, image de-noising, blind source separation, and compressed sensing. However, very limited applications can be found for application related to 3D surface representation or modeling apart

from rapid MRI [83].

Realizing the challenges of current imaging-guided system used during the MIS procedures and the advantages of signal processing techniques, we design a generally applicable algorithm which aims to provide surgeons with real-time 3D visualization of complete organ deformations using 3D optical patch images with limited views and a single preoperative MRI or CT scan. From the perspective of signal processing, to achieve 3D visualization of organ deformations, the three fundamental problems to be solved are: (1) how to represent a 3D surface efficiently in terms of low description dimensionality with high accuracy; (2) how to sample an organ surface using as few samples as possible to capture the deformations; (3) how to reconstruct the deformation using limited surface information with high fidelity. Solving these three problems lays the theoretical foundation of this thesis, so we will elaborate our proposed solutions to these problems in the this thesis. Further, we will also demonstrate the application of such a theory to ultrasound image enhancement and real-time surgical simulation.

1.2 Research Objectives and Contributions

Our work makes contributions from four different perspectives. First, we design a novel algorithm of sparse surface representation using structured dictionary, based on which the latter three contributions are achieved. (1) The approach for real-time 3D visualization of deformable organs aims to provide the surgeons with complete visual feedback during the MIS surgery. (2) An ultrasound image enhancement method is proposed to increase the ultrasound image resolution. (3) Last, the structured surface representation technique is applied for surgical simulation to obtain high efficiency and high realism performance.

1.2.1 Sparse Surface Representation

The first contribution of this thesis is to represent a deformable surface efficiently with block sparseness based on a data driven subspace learning and clustering method [141][143][146].

Spherical harmonic decomposition is applied to decrease the training data size and increase the homology among the training data. The key idea of this method is to identify the subspaces from a training data set in the transformed spherical harmonic domain and then cluster each deformation into the best-fit subspace for fast and accurate representation. This is supported by the fact that organs only deform in limited ways due to their mechanical properties, so a representative training data set carries sufficient deformation variability to generalize the potential deformations. Such sparse structured representations allow for reconstructing arbitrary deformations of the organ using limited surface data acquired with a 3D probe from restricted view. This algorithm is also generalized into applications of organs with both interior and exterior surfaces. The algorithm is verified using both finite element models, ex-vivo and in-vivo experiments.

1.2.2 3D Visualization of Organ Deformations

The second contribution is a new approach of 3D visualization of organ deformations to provide the surgeon with a high resolution real-time 3D view of the organs as they deform during the MIS surgery [142, 147]. This algorithm consists of training stage and reconstruction stage. The training stage applies the aforementioned sparse surface representation method to identify a surface representation with three critical properties: (1) to be easily deployed, it must be learnable from a small set of organ 3D surface samples obtained from MRI or CT scans from different subjects; (2) it must be sparse to allow reconstruction from a limited field of view of 3D endoscopic scanners; (3) the representation must have a known structure since it can then yield a reconstruction method that is resilient to measurement uncertainty. The reconstruction relies on real-time limited optical imaging patches and a single preoperative MRI or CT scan. Besides thorough theoretical description, we also provide solutions to practical issues such as selection of limited optical views and the registration of images from different modalities.

1.2.3 Ultrasound Image Enhancement

As the third contribution of this thesis, we present a method of improving 3D intraoperative ultrasound image resolution based on structured dictionary and multi-modal image fusion [145]. Organ surfaces are reconstructed in the structured dictionary using fine samples obtained with high resolution imaging modality (e.g. optical device) from limited field of view and coarse samples obtained with ultrasound device from the hidden area observable to ultrasound only. The proposed approach relies on the fact that all deformations of an organ surface lie in low dimensional subspaces that can be learned from a representative training data set collected from different subjects and different image resources. In this approach, we introduce a novel segmented training method that takes into account the different significance of spherical harmonic coefficients at different harmonic levels, so it improves the representation precision of those more significant coefficients and ultimately enhances the generalization of the identified subspaces. The multi-modal fusion algorithm applies proper weights to account for differences in resolution and noise levels between samples from different modalities. Further, the iterative correction step after initial reconstruction improves the enhancement precision. Ultimately, our algorithm is able to reveal important surface details that are not visible on the original 3D ultrasound images.

1.2.4 Surgical Simulation

The fourth contribution is an efficient algorithm for real-time surgical simulation. It applies the technique of structured surface representation to achieve high simulation efficiency by reducing the computational cost involved in the regular ODE solver. Majority of the deformation is estimated by surface reconstruction in the best-fit subspace. The preliminary experimental results demonstrate the feasibility of the method. It achieves an accuracy of less than 2mm in terms of Hausdorff distance.

1.3 Thesis Organization

The rest of the thesis is organized as follows. Chapter 2 provides brief surveys about the techniques for MIS operations and approaches for sparse signal representation. Chapter 3 presents a method for sparse representation of deformable organs with spherical harmonics and subspace pursuit. Chapter 4 introduces a method to achieve real-time visualization of deformable organs with sparse sampling. Chapter 5 applies the sparse surface representation technique to ultrasound image enhancement. Chapter 6 proposes an efficient surgical simulation approach based on the sparse representation algorithm to achieve real-time performance. Finally, Chapter 7 provides concluding remarks, limitation discussion and an outlook on future research directions.

Chapter 2

Background and Related Work

Limited visualization of the surgical scene during the MIS operation is a critical challenge, especially at the presence of organ deformations. A lot of efforts have been devoted to addressing this problem. From the hardware perspective, various intraoperative imaging devices have been designed to enhance surgeon's visualization ability and support the recognition of important anatomic structures. These systems integrate different imaging modules such as ultrasound, CT, MRI or a combination to form a multi-modality system. On the other hand, from the perspective of signal processing, to achieve 3D visualization of organ deformations, we need to seek an efficient representation approach to describe 3D surfaces with low dimensionality and high accuracy. Based upon these two different perspectives, this chapter first briefly reviews the state-of-art medical systems used for MIS surgeries, followed by the survey of approaches for organ surface representation and modeling, as well as methods of sparse signal representation as an emerging technique developed in the signal processing community.

2.1 Image-Guided Techniques for Minimally Invasive Surgery

Medical imaging has played a key role in the guidance of MIS procedures to augment the surgeons' spatial orientation and aid with the identification of critical anatomy and

pathology. The common sequence of steps involved in a typical image-guided interventions using computers are:

1. Preoperative image is obtained for the patient to be operated, typically with CT;
2. The surgical instruments attached with tracking sensors are localized;
3. The patient anatomy and the tracking sensors are registered with the preoperative image to obtain a common coordinate system;
4. The information from the tracking sensors on the instruments is collected, so that the position is shown on the preoperative image corresponding to the patient anatomy;
5. The virtual display of instrument position help the physicians manipulate the surgical tool to finish the desired procedure.
6. A post-operative image is acquired to confirm the completion of the procedure.

This thesis aims to improve surgeon's visualization ability in the 4^{th} and 5^{th} steps by reconstructing the deformations encountered during the surgery, caused by patient positioning, tool-tissue interaction and body movements. We classify current image-guided techniques into two main categories: intraoperative imaging and modeling approach. The following two subsections review these two types of approaches, respectively.

2.1.1 Intraoperative Imaging

Intraoperative imaging devices can retrieve updated images to address the effects of organ shift and tissue deformation during the surgery. The imaging modalities can be ultrasound, CT, MRI or a combination of these modalities. Each modality has its strengths and weaknesses in terms of image acquisition quality, speed, visibility/access restriction and potential negative effects on the patient's health.

2.1.1.1 IOUS

Recent advances in transducer and real-time computing technologies have exerted significant impact on ultrasound imaging technologies, especially in the area of real-time 3D echocardiography (RT3DE) [2][3]. The convergence of developments in 2D matrix arrays and computing technology for real-time rendering has resulted in a number of RT3DE systems [4][5]. Multi-modal coded excitation (MMCE), in conjunction with parallel processing of echo data (pre- or post-beamforming), offers the promise of increasing the frame rates while improving the SNR[6]. The filter bank can be implemented in real-time using commercially available high performance computing platforms, e.g. field programmable gate arrays (FPGAs) and graphics processing units (GPUs).

IOUS systems used during laparoscopic interventions utilize a flexible laparoscopic 2D ultrasound probe for imaging the target area. Electromagnetic tracking sensors attached to the probe allow the computer to reconstruct a 3D volume dataset from the freehand 2D measurements [7][8]. IOUS systems have been applied in different applications, such as partial liver resection [9][10], laparoscopic radio frequency ablation [11][12], and cardiac interventions [13][14][15][16]. Beller *et al.* [9] and Nakamoto *et al.* [10] utilize IOUS for liver surgery. The former [9] develops a navigation technique for liver resection based on 3D ultrasound and an optical tracking system which can significantly increase the accuracy of navigated resections. The latter [10] integrates a magneto-optic hybrid tracker into the 3D IOUS system to track the flexible US probe tip. IOUS has also been used for laparoscopic radio frequency ablation [11][12], in which the ultrasound imaging guides the tip of the radio frequency ablation probe to the tumor with high precision. For cardiac interventions, the work in [15] uses transesophageal probes for navigation of the medical instruments and on-line representation of the spatial structures of the heart. To overcome the motion caused by beating heart, Yuen el al. [16] propose a novel 3D IOUS guided system that compensates the tissue motion. This is achieved with a real-time 3D ultrasound tissue tracker which is integrated with the surgical instrument and a real-time instrument tracker.

It is well known that ultrasound has the advantages of safe usage, low cost and high

flexibility. The main drawback of IOUS is its relatively low image resolution due to speckle noise, echoic reflections and distortions resulting from different tissue properties. There is a large body of methods proposed to improve ultrasound image resolution. For speckle removal, various adaptive filtering methods have been designed [17][18][19][20]. These methods identify the characteristic parameters of the local speckle statistics to examine the similarity degree of the local speckle to the fully developed speckle. In particular, the method in [17] reduces speckle in log-compressed ultrasound images where logarithmic function is used to compress the dynamic range of the input echo envelope signals. The more generalized enhancement methods rely on noise reduction using thresholding [21][22], de-noising or noise suppression with wavelets [23][24]. These algorithms first apply wavelet transform to obtain the description coefficients in the time-scale domain, and then try to discriminate between coefficients representing the signal and those representing the noise. The noise components are suppressed before transforming the signal back to the original domain. The enhancement performance depends on the selection of parameters, such as wavelet type and threshold rules. A recent field of ultrasound image processing is based on stochastic resonance (SR) [25][26]. The approach in [26] operates both as an enhancement process and a noise reduction operation using the SR wavelet transform.

Another challenge of ultrasound is caused by gas insufflated before the MIS operation to gain better working space. It is known that, due to the substantial differences in acoustic impedance, ultrasound scanning is difficult when gas exists between the transducer and the organ of interest. One simple solution is to scan the interested area from the back to avoid the gas layer. A more accurate solution is to apply the advanced laparoscopic ultrasound device [43] which provides direct contact imaging of the target organ with high frequency ultrasound. A balloon is usually integrated at the tip of the probe [29]. The balloon is deflated initially and is inflated with liquid before imaging to clear the air pocket between the probe and the tissue. To avoid gas insufflation completely, gasless laparoscopic surgery [27] is a new trend. Kihara et al. [27] applies special retractors to maintain the working space instead of infusing CO2 gas. Chiesa et al. [28] tests an isobaric single-port

laparoscopic technique for kidney and liver biopsy on standing bovine during which space is provided by suspension of kidneys and the liver.

IOUS also faces the issue of limited field of view. Furthermore, the temporal resolution for 3D volumetric acquisition is often limited when the sector size is large or the imaging target is far relative to the probe's position. For example, in 3D transesophageal echocardiographic ultrasound, the frame rate achieved in patients, for a given depth, is currently insufficient to accurately image the valve dynamics, so increased temporal resolution is necessary [30].

2.1.1.2 Intraoperative MRI

Compared to IOUS, intraoperative MRI is a more intrusive solution from the perspective of instrument size, but it provides much higher image resolution. With intraoperative MRI, the magnets can be located inside the operating room so that images can be taken at various time during the surgery. The works in [45][46][50][51] use intraoperative MRI systems to compensate brain shift, achieve accurate navigation, and verify the surgical plan right after the operation. The typical device for intraoperative MRI is the discontinued GE Signa SPS "double-donut" 0.5 Tesla MR scanner[50]. This device allows the surgeon to stand between the two halves of the magnet while surgery and imaging are taking place simultaneously. An overview of intraoperative MRI devices presently available for brain surgery and their potential future applications is provided in [48]. The navigation system presented in [47] applies open MRI to liver radio frequency ablation using an MR-compatible endoscope with a distally mounted CCD camera. For intra-cardiac procedures, Rickers et al. [44] were the first to use real-time MRI to guide the placement of an atrial septal defect closure device.

Intraoperative MRI also faces obstacles to achieve widespread applications. The first issue is that the long image acquisition time limits the ability of the system to deliver real-time performance [34]. The method in [49] targets at real-time MRI, but its application is restricted to organs with repetitive motions that can be captured during the first learning

step. The system in [35] combines high-quality preoperative images and real-time intraoperative images to present the surgeons with updated visual results. Such a system can reslice and display the preoperative 3D image with a time resolution of 10 Hz, but not for intraoperative image due to the long imaging and rendering time (6-20 seconds). Consequently, it cannot be applied to organs with fast movement such as respiration. To overcome imaging delay, approaches in [36][37] utilize navigator echo extracted in imaging during surgery to achieve real-time monitoring. This method corrects the motion artifacts in the intraoperative images, but the motion is only compensated in 2D and no 3D visualization is provided in real-time. Other disadvantages of intraoperative MRI are its high cost, the potential safety hazard from the high field magnet and the sensitive electromagnetic distortion.

2.1.1.3 Intraoperative CT

Intraoperative CT can also be used in image guided-surgeries. In particular, the well-established mobile CT [52] is promising in intraoperative imaging due to its flexibility. Feuerstein *et al.* [53] utilize an optically tracked mobile isocentric C-arm that features cone-beam CT imaging capability, to achieve intraoperative visualization of soft tissues. Their method provides a solution for precise port placement and achieves registration-free intraoperative visualization by optically bringing the C-arm and laparoscope into the same tracking coordinate system. Recently, Navab et al. developed a camera augmented mobile C-arm system in which the camera images the surface of the body with the same pose as the C-arm. Consequently, the system is able to provide a fused image showing the patient's surface. Since the instrument axis is aligned with the X-ray source, no extra image registration is required. CT has the advantage of high resolution in most instances, but it is limited to uniplanar imaging and has relatively long image acquisition time (e.g. 32 seconds for a small 3D volume of $20 \times 20 \times 15 cm^3$ using C-arm [53]). Further, CT exposes both the patient and the surgical crew to radiation. Therefore, it is currently not widely used for intraoperative applications.

2.1.1.4 Intraoperative Multi-modal Imaging

Another promising direction for image-guided surgery is the integration of multiple modalities to compensate for weaknesses of the individual modality. A common combination is preoperative CT/MRI with intraoperative ultrasound [55][56][57][63][64], where the CT/MRI image provides clear anatomy for guidance and the ultrasound provides real-time information of the surgical scene during the operation. Registration between different modalities is required [58][59] and the accuracy is critical for safe navigation.

For the combination of CT/MRI and ultrasound, Comeau et al. [57] present a surgical guidance system that incorporates preoperative MRI scan information with intraoperative ultrasound images to detect and correct brain tissue deformation during the image-guided neurosurgery. The deformation is corrected and warped based on the surgeon's qualitative assessment of the intraoperative brain shift before aligning images from the two modalities. Lange et al. [56] propose an approach to augmenting intraoperative 3D ultrasound with preoperative anatomical models and planning data. Their method utilizes both the iterative closest point algorithm and multilevel B-Splines for registration based on vessel center lines. The MR-guided focused ultrasound surgery in [63] performs thermal therapies by taking the advantage of MRI's ability of precise targeting, visualization, and quantification of temperature changes. The work in [64] addresses the issues of motion related thermometry artifacts and focal point relocation for treating a moving target while using the MRI-controlled high-intensity focused ultrasound.

In addition, an X-ray angiographic system can also be arranged with an MRI device in the operating room to form an XMR system. As proposed by Rhode et al. in [60], such a system allows MRI images to be readily registered with fluoroscopic images of the subject during the same surgery or imaging session. An extension to the XMR technique is the development of closed-bore XMR systems (CBXMR), in which the MR device integrates the X-ray system such that radiographic and MRI images can be acquired simultaneously [61][62].

The main challenge for these multi-modal imaging systems is the registration between

different modalities. Various studies have been conducted to evaluate the registration accuracy [55][58][59]. In particular, the registration of IOUS with preoperative imagery is often not accurate enough for it to play a role in the routine clinical diagnostic work-up [55]. Bao et al. [32] evaluate the registration accuracy between liver CT and laparoscopic ultrasound based on the marker point method. The reported mean target registration error (TRE) ranged from $4.35mm$ to $7.04mm$. Herline et al. [33] propose an approach of mapping the physical space into the CT image space, with achieved overall registration error of $2.9mm$. An automatic CT-ultrasound registration method is presented in [31]. This method registers the CT image to a simulated ultrasound to provide the physicians or sonographers with a feeling for the accessibility and optimal orientations even before the ultrasound exam. The resulted TRE level is $8.1mm$.

2.1.2 Modeling Approach

The second type of methods to tackle the problem of organ deformation during MIS procedures is based on modeling. These approaches characterize and simulate the deformation or motion of the organ with mathematical models, like B-spline, thin-plate splines and elastic body splines. The goal is to apply the deformation model into the image-guided system to warp the preoperative images and thus reflect the updated scene during the surgery. Tissue properties and measurements or images acquired during the surgery are fed into the model to constrain the model properly and produce deformation information with high fidelity.

The simplest biomechanical model of soft tissue deformation is the viscoelastic model which assumes that tissue is an isotropic linear elastic solid [65][66]. Ferrant et al. propose a new registration approach that applies surface based correspondences to drive a linear elastic biomechanical model of the brain rather than use estimates of forces that are often difficult to accurately determine. To address the computational cost issue, a parallel implementation of an intraoperative nonrigid registration algorithm is presented in [66]. This method first establishes the surface deformation using an active surface algorithm, followed by volumetric brain deformation based on a linear elastic model. The reported simulation time of a 3D

volumetric deformation is less than ten seconds. A more sophisticated method is the coupled fluid-elastic model which assigns different constitutive laws to different regions of the model. For example, in [67], Hooke's law is used to represent the behavior of the solid material and the Navier-Poisson law is applied for the fluid. Another representation for soft tissue is to consider it as a porous solid saturated by a fluid and the behavior is determined by changes in hydration and the introduced loads [68][68]. [70] provide an elaborative survey about biomechanical modeling of soft tissue based on finite elements in the context of image-guided surgery.

For organs with recurrent motions like heart beat and respiration, particular methods have been proposed to model these deformations. Huang et al. [97] propose a spatio-temporal shape modeling method based on spherical harmonics to represent the shapes sequence of anatomical structures in medical images with high efficiency and flexibility. However, this method has not been integrated into the real image-guided system for further verification. More practical solutions to compensating recursive motions are provided in [72] and [73]. The former [72] develops a navigation system for catheter interventions that combines magnetic catheter tracking and intraoperative ultrasound imaging to compensate the motion caused by heart beat and breathing. The latter [73] applies a multi-sensor prediction scheme that integrates the patient's electrocardiogram, respiration pressure signal and tracking data of natural landmarks on the heart surface for motion compensation. Motion caused by breath is tackled in [74] and [75]. Both methods build the respiratory motion model using external markers on the skin and/or internal fiducials to predict the internal organ motions. The motion tracking algorithm can be further improved using more complicated models. For example, the Kalman filter is adopted in [76] to predict multiple initial guesses for image registration which is further used for the instrument tracking.

Although deformation modeling is a well-developed research area, its integration into practical image-guided system is still in infancy because of the following two reasons. (1) Most modeling approaches are intrusive and require continuous measurements of organ motions using tracking sensors implanted or attached to organs to track organ deformations

and correct preoperative imagery or intraoperative imagery between successive scans. (2) The computational complexity of the modeling methods is usually incompatible with the real-time requirement for 3D organ deformation tracking in MIS. To alleviate this problem, systems typically use simpler but less accurate mathematical models, leading to reduced accuracy and resolution that is inadequate for safe surgical interventions. Due to these shortcomings, the application of biomechanical models in image-guided surgery is mainly restricted to open neurosurgery for compensating brain shift [77] and open liver surgery [78][79], where tracking devices are used to record the deformation at selected points and feed the deformations at limited locations into the FEM model to interpolate deformations at other locations. As pointed out by [79], the pitfall of these model-driven deformation compensation methods is that the incomplete surface data could result in misalignment and erroneous deformation warping when the coverage of the intraoperative imaging device is uneven and does not capture enough surface points.

2.1.3 Remarks

State-of-the-art techniques are promising and offer attractive advantages to improve surgical precision of MIS. However, according to several recent experimental and exhaustive literature survey studies, e.g., [38][39][40][41], current navigation and 3D intraoperative visualization systems do not meet the requirements of high resolution, real-time and 3D visualization simultaneously to support the recognition of anatomic structures and accurate instrument localization for safe abdominal MIS procedures. Today, image guided surgery is mostly used in rigid organ interventions such as otolaryngology and orthopedic procedures which essentially register instruments to the preoperative imagery for guidance. Unfortunately, these traditional methods, such as established rigid navigation approaches, defining anatomical reference points or surfaces with a tracked pointer device, have so far failed to deal with the challenges associated with the tissue motion and deformation [38].

The problem of accurately localizing the instruments [42] is beyond the scope of this thesis. But it is important to realize the navigation challenges during MIS procedures due to

the missing tactile feedback and limited degree of positioning, especially for ultrasonography considering its low image quality. An optical tracker can be used to estimate the pose of a transducer, but it fails to localize the flexible tip caused by the missing line of sight to the tip. Electromagnetic tracking is used for localizing flexible endoscopic instruments. However, it is susceptible to the interference from ferromagnetic materials. Recently, Feuerstein *et al.* [43] present a hybrid tracking setup which combines optical tracking of the transducer shaft with electromagnetic tracking of the flexible transducer tip to reduce the dynamic electromagnetic tracking errors. The applicability of this hybrid system in a clinical setup needs to be further validated. Despite the advantages of the existing techniques, challenges still remain to achieve higher tracking accuracy (e.g. sub-millimeter) and more robustness.

2.2 Organ Surface Representation and Modeling

Broadly speaking, there are two major categories of surface representation methods: local feature based models and global or parametric models. The work in [84] based on geometric partial differential equations (PDE) belongs to the former category which derives Euler-Lagrange equation and a geometric evolution equation (or geometric flow) to describe the surfaces. Similarly, the approach in [85] that treats the whole surface as a union of localized patches is also a local feature based method. On the other hand, global surface representation methods [86][88][89][90] decompose surfaces into other primitive shapes and each parameter after decomposition does not carry local feature information but affects the whole shape. Global surface representation are more appropriate for shape analysis and classification due to the lower dimensionality of the parameter space. The approach proposed in this thesis falls into the category of parametric global surface description.

2.2.1 Spherical Harmonic Representation

Parametric surface representation describes a surface in a single functional form, such that the surface is fully characterized by a set of parameters in a particular domain. Surface

harmonics such as spheroidal harmonics, cylindrical harmonics and spherical harmonics (SH) [86] are widely used as building blocks for global surface description. Each harmonic does not bear localized features but contributes to the entire shape description. Among those different types of harmonics, a well-known approach is the spherical harmonic decomposition(SHD), which has advantages of smoothness and high accuracy [86][91]. Spherical harmonics are solutions of Laplace's equation expressed in the spherical coordinates, which consists of infinite number of basic functions defined as:

$$Y_{lm}(\theta,\varphi) = (-1)^m \sqrt{\frac{2l+1}{4\pi}} \sqrt{\frac{(l-m)!}{(l+m)!}} P_{lm}(cos\theta) e^{im\varphi} \tag{2.1}$$

where l is the harmonic degree within $[0, +\infty]$, and m is the harmonic order varying in $[-l, l]$. P_{lm} is the associated Legendre function. Those spherical harmonics satisfy the orthogonal condition:

$$\int_{\varphi=0}^{2\pi} \int_{\theta=0}^{\pi} Y_{lm}(\theta,\varphi) Y_{in}(\theta,\varphi) sin\theta d\varphi d\theta \ = \delta_{lm}\delta_{in} \tag{2.2}$$

Then a 3D surface function with finite energy can be expanded with SH series as:

$$\mathbf{x}(\theta,\varphi) = \sum_{l=0}^{\infty} \sum_{m=-l}^{+l} f_{lm} Y_{lm}(\theta,\varphi) \tag{2.3}$$

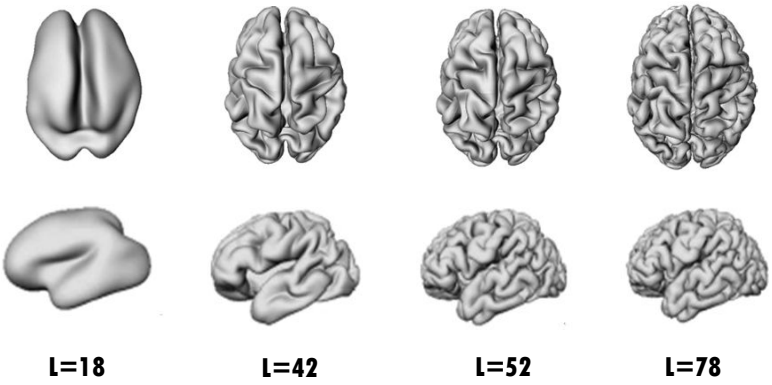

Figure 2.1: Representation of brain with different harmonic levels.

The harmonic coefficients in f_{lm} are approximated using the inner product of the function $\mathbf{x}(\theta, \varphi)$ and the basis $Y_{lm}(\theta, \varphi)$:

$$\begin{aligned} f_{lm} &= < \mathbf{x}(\theta, \varphi), Y_{lm}(\theta, \varphi) > \\ &= \int_{\varphi=0}^{2\pi} \int_{\theta=0}^{\pi} \mathbf{x}(\theta, \varphi) Y_{lm}(\theta, \varphi) sin\theta d\varphi d\theta \end{aligned} \tag{2.4}$$

Fig. 2.1 demonstrates the representation of a brain surface using spherical harmonics at different levels. More surfaces details are retained as higher level of harmonics is involved. With such a transformation, the 3D shape analysis can be performed in the harmonic domain with reduced data dimensions.

2.2.2 Spherical Parameterization

Initially, SHD can only be applied to star-shape or convex closed objects [86][87]. Brechbuhler et al. first introduced spherical parameterization to extend the harmonic representation to any genus-0 surface[1]. Such a surface parameterization process defines an one-to-one mapping from the original surface to the surface of a unit sphere, as shown in Fig. 2.2. As a mapping of convoluted surface structures onto the surface of a sphere introduces distortions, optimization of the distribution of nodes in parameter space becomes necessary. After Brechbuhler's work, various algorithms have been proposed to establish such a mapping by

[1]The genus of a connected surface is an integer representing the maximum number of cuttings along non-intersecting closed simple curves without rendering the resultant manifold disconnected. It is equal to the number of handles on it, so a sphere is genus 0 and a torus is genus 1.

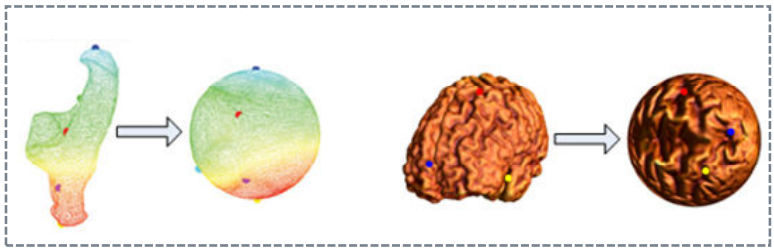

Figure 2.2: Spherical parameterization: one to one mapping from the object to the sphere.

imposing different constraints. Approach in [93] is based on conformal mapping by minimizing the harmonic energy. The control of area and length distortions (CALD) method in [92] starts from an initial mapping and alternately performs local and global smoothing until a stop criterion is met.

2.2.3 Organ Modeling with SHD

SHD has been widely used in organ modeling. Dillenseger et al. applied SHD to 3D kidney modeling [88] and reported ill-posed problem if only partial surface information was available. Chung et al. introduced the weighted fourier series representation for cortical surfaces [89][90], which essentially adds an additional exponential weight for quick converge and reducing ringing artifacts [94]. Meanwhile, an iterative residual fitting (IRF) algorithm [95] is proposed to lower the computational cost involved in the transformation process. SHD is also used to model dynamic motions of the heart [96][97]. The work in [97] specially targets for a spatial-temporal modeling method to represent the dynamic anatomical structure of left ventricular with known motion period. Further, for open surface such as left ventricle wall without top part, [98] introduces hemispherical harmonics for open surface representation with modified one-to-one hemisphere mapping.

Besides surface modeling, SHD has also been applied in 3D surface alignment and 3D model search engine. [99][100][101] propose different surface registration algorithms which are all based on the unique property of the SH coefficients under rotation. [102][103][104] utilize SHD for similarity retrieval from a database or sequence of 3D models, in which the SH coefficients are used as the feature vector for similarity comparison and searching.

2.2.4 Statistical Modeling

Different from the above mentioned modeling approaches, statistically motivated surface modeling methods have been proposed in [105][106][107][108][109]. Those methods are generally based on principle component analysis (PCA), which first compute the mean shape and then build the model by establishing legal variations learned from a set of training data

for a given type of images, such as bone [105][109]. With PCA, the major variations of the shape populations are described by the first few basis vectors, such that any surface of that shape population can be projected into an orthogonal subspace spanned by the retained vectors. Mathematically, a surface $\vec{x}_i$ can be represented as

$$\vec{x}_i = \overline{\vec{x}} + \mathbf{P}\vec{b}_i \tag{2.5}$$

where $\mathbf{P} = (\vec{p}_1\ \vec{p}_2\ ...\ \vec{p}_t)$ contains the first t eigenvectors of the covariance matrix generated from the training surfaces, and $\overline{\vec{x}}$ is the mean vector. $\vec{b}_i$ is the coefficient vector which can be calculated by

$$\vec{b}_i = \mathbf{P}^T(\vec{x}_i - \overline{\vec{x}}) \tag{2.6}$$

To address the challenge of small sample size encountered in practice, the work in [107] defines a multi-resolution integrated model which is able to capture the most significant deformations from a small training set and generate representative variation modes of the organ shapes.

2.2.5 Remarks

Current surface modeling/representation approaches show great promise under certain application conditions. However, most of the previous works are designed for either static models [88][89][90], or particular deformable organs with known physical properties (such as motion cycle) [97]. Further, computation bottleneck caused by large spherical harmonic basis prevents it from meeting the real-time requirement. In the area of surface registration and similarity retrieval, spherical harmonic coefficients are directly applied as the features, which usually results in large parameter dimensions. Taking brain SH representation as an example, more than 6000 spherical harmonic coefficients are involved to maintain surface structure details [89][90]. For PCA based statistical modeling methods, the resulting subspace that captures the variation in the population is either a super subspace including all

training data or a truncated subspace with sacrificed generalization. In addition, PCA tends to be computational expensive when performing eigenvector decomposition as training data dimension increases, and it does not lead to any structure in the representation.

2.3 Sparse Signal Representation

Sparse signal representation has steadily gained attention over the years in the signal processing community. The aim is to find a representation of a signal which is sparse, or compact, such that most of the energy of a signal can be captured with only a few non-zero coefficients in a given dictionary. For a signal $\vec{x}$ of dimension N, we wish to represent it using a linear combination of atoms in dictionary Φ of dimension $N \times K$. Usually, K is larger than N, so the representation is redundant. We seek an approximation of signal $\vec{x}$

$$\vec{x} = \Phi\vec{b} + \epsilon \tag{2.7}$$

where $\vec{b}$ is the sparse coefficient vector with zeros at most if its entries and ϵ is the approximation error. The sparse representation problem can be formulated in the exact sense as

$$\min_{\vec{x}} \|\vec{b}\|_0, \quad s.t \quad \vec{x} = \Phi\vec{b} \tag{2.8}$$

or alternatively, in the approximate sense

$$\min_{\vec{x}} \|\vec{b}\|_0, \quad s.t \quad \|\vec{x} - \Phi\vec{b}\|_2 \leq \epsilon \tag{2.9}$$

where $\|.\|_0$ is the L_0-norm counting the non-zero entries in the vector, and $\|.\|_2$ is the L_2-norm of the vector. Now the critical problems to obtain sparse representation become: (1) how to obtain the sparse vector $\vec{b}$, and (2) in which dictionary the representation is sparse. The following subsections summarize the possible approaches to these problems.

2.3.1 Sparse Representation Algorithms

Sparse representation is also known as atomic decomposition or subset selection. The goal is to find the active atoms in the dictionary for representation. The problem formed in Eq. 2.8 or Eq. 2.9 is non-differentiable and an exact solution has been shown to be NP-hard [110][111], so it is usually solved approximately.

The first widely applied methods to seek sparse representation are greedy approaches, including Matching Pursuit (MP) [112][113], Orthogonal Matching Pursuit (OMP) [114][115] and Orthogonal Least Square (OLS) [116][117]. Those methods iteratively first select the most correlated element from dictionary, and then remove the contribution of that element with de-correlation, before finding the next atom. Because of the iterative nature of the method, stopping criteria such as a maximum number of iterations, or signal approximation error, are usually required to terminate the greedy iterative process.

The second type is global optimization algorithms [118][119][120], which relaxes the sparseness constraint to L_p norm

$$\min_{\vec{x}} \|\vec{b}\|_p, \quad s.t \quad \|\vec{x} - \Phi\vec{b}\|_2 \leq \epsilon \tag{2.10}$$

such that the sparsity is a side-effect of the optimization. Methods such as Basis Pursuit (BP) [118], FOCUSS [119] and Iterative Thresholding [120] belong to global optimization. BP method approximates the l_0-norm sparsity constraint with an l_1-norm criterion, which effectively converts the problem into a convex optimization one, solved globally with linear programming. The orthogonal subspace pursuit (OSP) method [121] used in this thesis belongs to the greedy category, which does not require prior knowledge of the dimension of the subspaces and combines the learned subspaces to produce a data driven dictionary with good sparseness and generalizability. This method is also less computationally costly compared to the gold standard K-SVD algorithm [125].

2.3.2 Sparse Representation Dictionary Selection

Besides the first issue of sparse decomposition as mentioned above, the second equally important issue for sparse representation is how to select a dictionary for an application. The selection of dictionary directly affects the efficiency of the representation. For example, if the data is known to be rich in harmonics, a dictionary with Fourier basis is a good choice. Similarly if transients are expected to present in the signal, then a dictionary with wavelet waveforms would be more appropriate. In the case of a combination of both harmonics and transients, the dictionary should reflect both characteristics.

The two main groups for dictionary design methods are standard dictionaries built out of well-known bases, and trained dictionaries that are inferred from the training data. For the standard dictionary, it is well known that, the wavelet transform can be used to generate sparse multi-scale representations of images, the Short-Time Fourier Transform (STFT) generates sparse time-frequency representation of speech signals, and the DCT is another transform that has been used for compression in audio coding algorithms due to its good compaction property. In these cases, the standard dictionaries are composed of wavelet, STFT and DCT, respectively.

For dictionary learning, the applicable approaches include Maximum Likelihood Estimation (MLE) [122], Method of Optimal Directions (MOD) [123], and Maximum A-Posteriori (MAP) [124], etc.. Those methods attempt to generalize the type of considered signal with the basis identified from a representative training data set. The proposed approach in this thesis is based on trained dictionary, since, to the best of our knowledge, there is no common basis in which random surfaces can be sparsely represented.

2.4 Block Sparse Representation

With the conventional sparse representation, non-zero values in the coefficient vector $\vec{b}$ do not have any pattern. However, with block sparsity, we apply the representation structure such that a signal lie in a union of subspaces. Consequently, the nonzero coefficients are

not scattered randomly but occur in clusters [126][127][128]. For example, if there are J subspaces in a dictionary Φ, the structured dictionary Φ is defined as an union of the J subspaces. The vector $\vec{x}$ can be represented by some of the J subspaces, so $\vec{b}$ is a concatenation of blocks

$$\vec{b}^T = [\ \underbrace{b_1\ \ldots\ b_{d_1}}_{block1}\ \underbrace{b_{d_1+1}\ \ldots\ b_{d_1+d_2}}_{block2}\ \ldots \underbrace{b_{I-d_J+1}\ \ldots\ b_I}_{blockJ}\ ] \tag{2.11}$$

If $\vec{x}$ can be represented by the second block, then the coefficient vector has the following structure.

$$\vec{b}^T = [\ \underbrace{0\ 0\ \ldots\ 0}_{block\ 1}\ \underbrace{\times\ \times\ \ldots\ \times}_{block\ 2}\ \ldots \underbrace{0\ \ldots\ 0}_{block\ J}\ ] \tag{2.12}$$

where "×"s indicate non-zero values. Fig. 2.3 shows the block sparse structure, where "A1", "A2" and "A3" represent the subspaces in the dictionary.

Block-sparsity arises naturally, e.g., in measurements of gene expression levels [129], in dealing with multi-band signals [130], or in the problem of multiple measurement vector [131][132]. It is shown in [126] that applying the structure of block-sparsity can provably leads to better reconstruction results than treating the signal in the traditional fashion without assuming any inherent data structure.

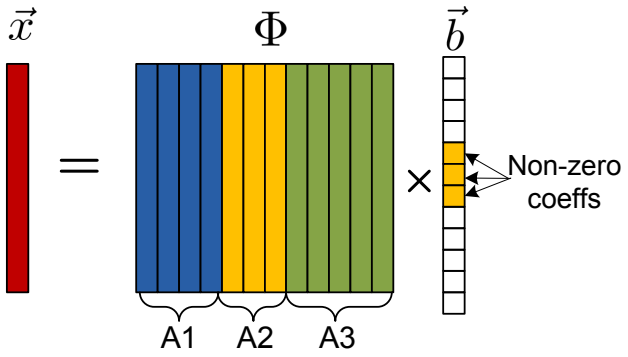

Figure 2.3: Block sparse structure.

2.4.1 Remarks

Although sparse representation has been widely applied in the fields of signal compression, image de-noising [133], blind source separation [134], and compressed sensing [135], few applications can be found for 3D surfaces. The work in [136] propose to solve the problem of denoising and occlusion restoration of 3D range data based on dictionary learning and patch sparse representations. The methods in [137][138] utilize sparse representation for 3D face recognition, where each face is represented by a set of features extracted from a training data set, and a face is recognized by solving a L_0-norm minimization problem based on the dictionary.

Our approach proposed in this thesis involves sparse surface representation and surface recovery from incomplete samples. This bears similarities to compressed sensing [135] that seeks to acquire signals - known to have sparse representations in a domain - using a minimal number of measurements. However, compressed sensing theory requires that measurements are random linear combinations of all signal samples. In other words, the entire signal space must be accessible although the number of acquired measurements is small. This is difficult to meet when only a part of the signal is within the acquisition range. Meanwhile, approaches for 3D scan completion or surface inpainting have been developed to fill small holes [139][140] existing in the scanned data. Example-based approaches can recover relatively large missing portion using patch warping and stitching [140] from an extensive 3D model library. These approaches still require the majority of surface information to be available. Besides, the warping and matching procedures are too computationally demanding to be implemented in real-time. In contrast, the proposed approach in this thesis identifies a structured sparse representation of each 3D surface. This allows the procedure to reconstruct arbitrary organ deformations using very limited observed data with high accuracy.

Chapter 3

Sparse Surface Representation

3.1 Chapter Introduction

This chapter proposes a novel algorithm of sparse representation of deformable surface (SRDS) based on spherical harmonic decomposition (SHD) and orthogonal subspace pursuit (OSP). This approach relies on the fact that because organs deform in limited ways due to their mechanical properties, it is possible to identify subspaces from a representative training data set to generalize the potential deformation variations of the organ to be considered. Therefore, each deformation of that organ can be represented in a best-fit subspace with low dimensionality and high accuracy. This feature of block sparseness enables reconstruction of arbitrary deformations of the surface using limited surface data as shown in the later chapters.

In our SRDS method, the SHD procedure is applied to transform the training surfaces into spherical harmonic domain to decrease the training vector size and reduce the high frequency components to promote the homology among the training data. For subspace identification, the OSP method does not require prior knowledge of the dimension of the subspaces and combines the learned subspaces to produce a data driven dictionary with good sparseness and generalizability while at a lower computational cost compared to the gold standard K-SVD algorithm. The main contributions of this chapter include:

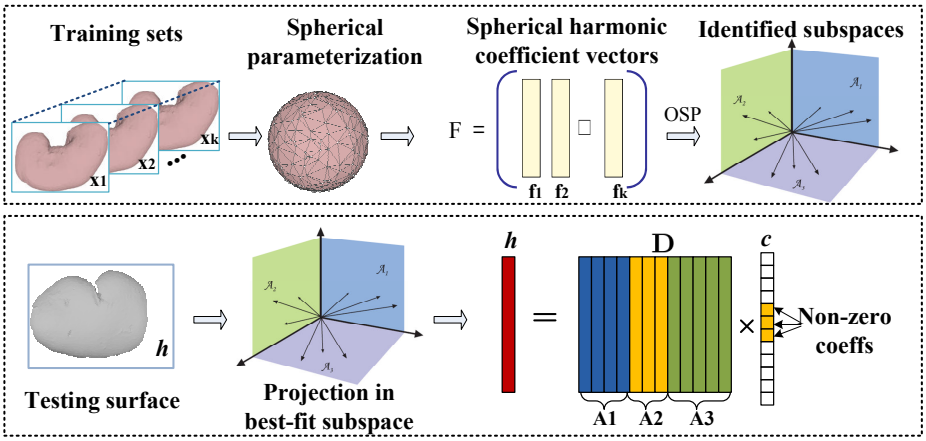

Figure 3.1: Overview of SRDS algorithm.

1. Propose a novel sparse surface representation method that features block sparseness and low subspace dimensionality.

2. Generalize the representation approach to include deformations occurred on multiple layers of surfaces.

3. Present evaluation results conducted using computer models, ex-vivo and in-vivo experimental data.

This chapter is organized as follows: in Section 3.2, we describe the details of the proposed SRDS algorithm. Section 3.3 presents some experimental results using finite element model (FEM) data, ex-vivo and in-vivo experimental data. Finally, Section 3.4 finishes this chapter with conclusions.

3.2 The SRDS Algorithm

The SRDS algorithm is outlined in Fig.6.1. The upper block describes steps involved in the training stage. The training surfaces can be from various data sources, such as MRI/CT scans and realistic computer models. SHR is first performed to represent the deformable surfaces in the harmonic domain to decrease the length of surface descriptor and filter out

the high frequency components for achieving better homology among the training surfaces. Then an efficient Orthogonal Subspace Pursuit (OSP) method [121] is applied to $\mathbf{F}$ in the transformed domain to identify the subspaces in which each SH coefficient vector $\vec{f}_k$ lies. The lower block in Fig. 6.1 indicates the representation of a testing surface h in the trained dictionary $\mathbf{D}$ with a block-sparse vector c. The main three steps of SRDS algorithm are described as followings.

3.2.1 Step 1: SHD

SHD is performed on each training surface using harmonics up to level L. For each level l, there are $2l+1$ harmonics that are ordered as $[-l \quad -l+1 \quad ... \quad 0 \quad ... \quad l-1 \quad l]$. Let $\mathbf{Y}$ denote the matrix composed of all $(L+1)^2$ harmonics, which is formatted as

$$\mathbf{Y} = \left| \begin{array}{ccccccc} \vec{Y}_{0,0} & \vec{Y}_{1,-1} & \vec{Y}_{1,0} & \vec{Y}_{1,1} & \cdots & \vec{Y}_{L,L} \end{array} \right|_{N\times(L+1)^2} \tag{3.1}$$

where N is the number of vertices on the object surface. With proper parameterization [91][92], a surface can be represented with harmonics as

$$\mathbf{x} = \mathbf{Y}\vec{f} \tag{3.2}$$

where $\mathbf{x}$ stands for a surface with N samples and $\vec{f} = [f_{0,0} \ f_{1,-1} \ f_{1,0} \ f_{1,1} \ \cdots \ f_{L,L}]^T$ is the harmonic coefficient vector. The linear system can be solved with the Least Square (LS) constraints outputting $\vec{f}$

$$\vec{f} = (\mathbf{Y}^T\mathbf{Y})^{-1}\mathbf{Y}^T\mathbf{x} \tag{3.3}$$

For a sequence of K deformed training surfaces $\mathbf{X}$, since the k^{th} surface is represented by $\vec{f}_k$ after SHD, the group of deformations can be described by a matrix $\mathbf{F}$

$$\mathbf{F} = \left| \begin{array}{cccc} \vec{f}_1 & \vec{f}_2 & \cdots & \vec{f}_K \end{array} \right|_{(L+1)^2\times K} \tag{3.4}$$

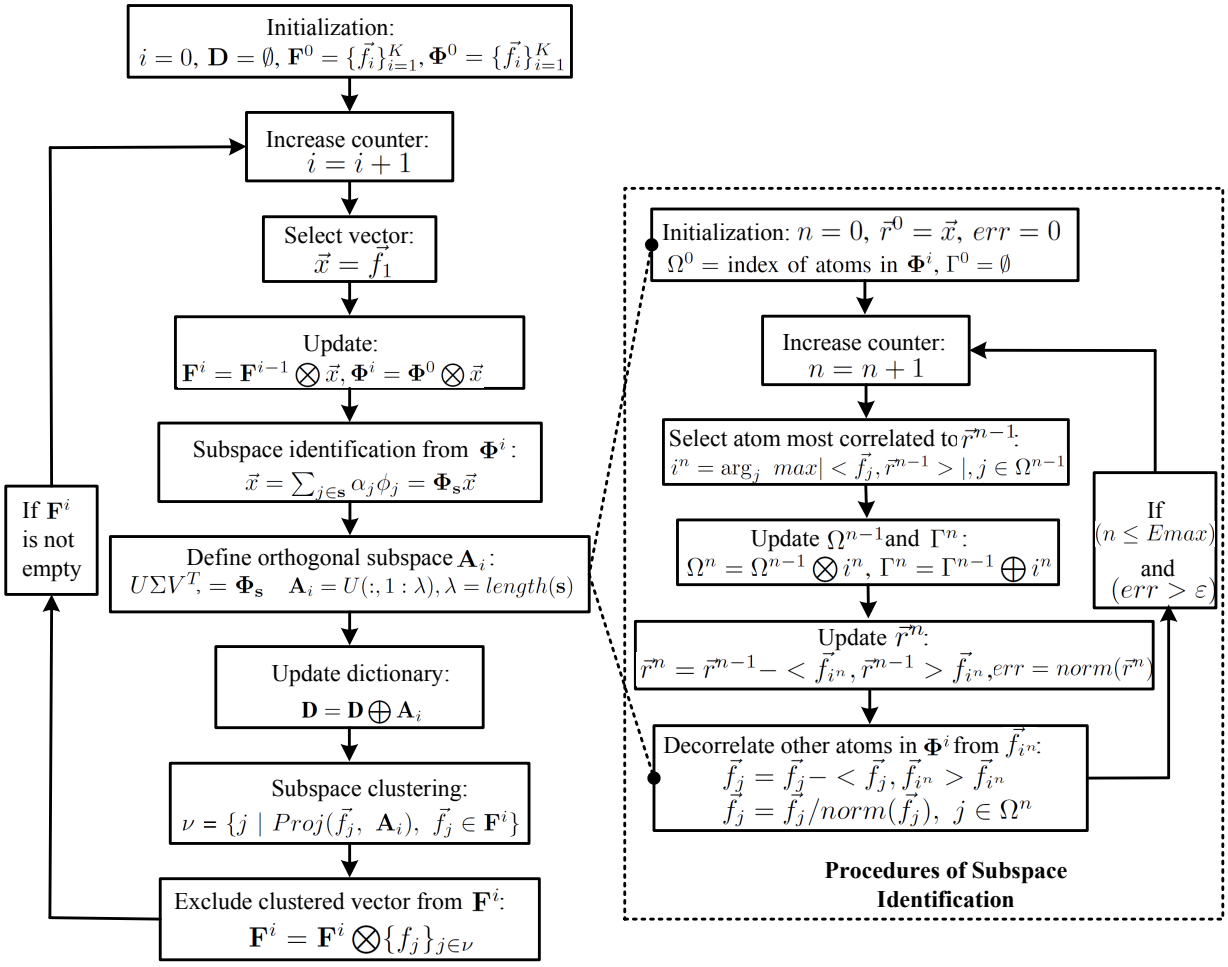

Figure 3.2: Overview of iterative orthogonal subspace pursuit method.

in the harmonic domain as

$$\begin{aligned} \mathbf{X} &= \Big| \ \mathbf{x}_1 \quad \mathbf{x}_2 \quad \cdots \quad \mathbf{x}_K \ \Big|_{N \times K} \\ &= \mathbf{YF} \end{aligned} \tag{3.4}$$

3.2.2 Step 2: Subspace Identification with OSP

The aim of the second step is to explore the structures in those training deformations in the transformed harmonic domain and recognize the inherent subspaces in which the SHD coefficient vectors of the training deformations can be projected with high accuracy.

The newly developed OSP algorithm [121] is adopted since it features better generalization and less computational cost compared to the gold standard K-SVD algorithm [125]. OSP is an iterative process that terminates when one of the pre-defined criteria is met. In this chapter, we specify the following two stopping criteria : 1) an error threshold ε for subspaces selection, 2) a maximum number of iterations E_{max} for both controlling the subspace dimensions and avoiding deadlock searching. Further, the threshold for vector clustering is denoted as η, that is, we declare that a vector lives in a subspace if it can be projected to that subspace with error (l_2 distance) no larger than η.

A. *Subspace Pursuit*

A more detailed description of the approach follows. Each vector $\vec{f}_k$ of length $(L+1)^2$ in $\mathbf{F}$ is normalized by its l_2 norm. For convenience, we still use $\mathbf{F}$ to denote the SH coefficient matrix after vector-wise normalization. The procedures of the subspace identification method are illustrated in Fig. 3.2. The left part of the flowchart shows the steps involved during the iterative searching of multiple subspaces. The right part corresponds to the detailed process of identifying each subspace. The algorithm is described as follows, where $A \bigotimes B$ means element exclusion and $A \bigoplus B$ stands for inclusion.

1. Initialization: iteration counter $i = 0$, learned dictionary $\mathbf{D} = \emptyset$, training set $\mathbf{F}^0 = \{\vec{f}_i\}_{i=1}^K$, training dictionary $\mathbf{\Phi}^0 = \{\vec{f}_i\}_{i=1}^K$

2. Subspace searching and clustering

   - $i = i + 1$;
     select a vector from $\mathbf{F}^i$, e.g. first column of $\mathbf{F}^i$, let $\vec{x} = \vec{f}_1$;
     exclude $\vec{x}$ from $\mathbf{F}^i$ and $\mathbf{\Phi}^i$, $\mathbf{F}^i = \mathbf{F}^{i-1} \bigotimes \vec{x}, \mathbf{\Phi}^i = \mathbf{\Phi}^0 \bigotimes \vec{x}$.
   - Find vectors from $\mathbf{\Phi}^i$ for representing $\vec{x}$ with errors no larger than ε within E_{max} iterations, such that $\vec{x}$ can be represented as $\vec{x} = \sum_{j \in \mathbf{s}} \alpha_j \phi_j = \mathbf{\Phi}_\mathbf{s} \vec{x}$, where $\mathbf{s}$ is a set containing the indices of selected atoms from $\mathbf{\Phi}^i$. The process of finding $\mathbf{s}$ is further outlined as follows.

(a) Initialization: iteration counter $n = 0$, residual $\vec{r}^0 = \vec{x}$, error level $err = 0$, $\Omega^0 =$ index of atoms in $\mathbf{\Phi}^i$, index set of selected atoms $\Gamma^0 = \emptyset$

(b) While $(n \leq Emax)\&(err > \varepsilon)$, conduct the following operations.

- $n = n + 1$.
- Select the atoms in $\mathbf{\Phi}^i$ with maximum correlation to residual $\vec{r}^{n-1}$:
  $i^n = \arg_j \ max| < \vec{f}_j, \vec{r}^{n-1} > |, j \in \Omega^{n-1}$.
- Remove atom index i^n from Ω^{n-1} and add it to Γ^n:
  $\Omega^n = \Omega^{n-1} \bigotimes i^n$, $\Gamma^n = \Gamma^{n-1} \bigoplus i^n$.
- Update residual $\vec{r}^n$ and calculate the current representation error:
  $\vec{r}^n = \vec{r}^{n-1} - < \vec{f}_{i^n}, \vec{r}^{n-1} > \vec{f}_{i^n}$;
  $err = norm(\vec{r}^n)$.
- Decorrelate remaining atoms in $\mathbf{\Phi}^i$ from $\vec{f}_{i^n}$:
  $\vec{f}_j = \vec{f}_j - < \vec{f}_j, \vec{f}_{i^n} > \vec{f}_{i^n}$;
  $\vec{f}_j = \vec{f}_j / norm(\vec{f}_j), \ j \in \Omega^n$

(c) $\mathbf{s} = \Gamma^n$ after the loop terminates.

- Define orthogonal subspace $\mathbf{A}_i$ via SVD decomposition:
  $U\Sigma V^T = \mathbf{\Phi_s}$, $\mathbf{A}_i = U(:, 1 : \lambda)$, where $\lambda = length(\mathbf{s})$ is the number of selected atoms.
- Update the trained dictionary $\mathbf{D} = \mathbf{D} \bigoplus \mathbf{A}_i$.
- Select vectors from $\mathbf{F}^i$ that can be represented by $\mathbf{A}_i$ with error less than η, and then remove them from $\mathbf{F}^i$:
  $\mathbf{F}^i = \mathbf{F}^i \bigotimes \{f_j\}_{j \in \nu}$, $\nu = \{j \mid Proj(\vec{f}_j, \ \mathbf{A}_i) \leq \eta, \ \vec{f}_j \in \mathbf{F}^i\}$, where ν is the index set of those vectors whose projection error in $\mathbf{A}_i$ is less than η.
- Repeat above steps until all the vectors are clustered.

B. *Subspace Pruning*

One disadvantage of the traditional OSP algorithm is the presence of "spurious" or redundant subspaces especially as the dimension of the training data set increases. Those

subspaces identified in the earlier iterations actually can be better represented by the later identified subspaces. Therefore a post processing step is used to identify and then discard the redundancy among the subspaces without decreasing the performance. This is implemented by repartitioning the training data among the initial subspaces and then eliminating subspaces in which very few or no vector is clustered. In some cases, where the subspace size is limited to some constraint, an optimization step can be applied in conjunction with the pruning step. The details of the subspace optimization design is described in [121].

C. *Matrix* $\boldsymbol{F}$ *Factorization*

After identifying the inherent subspaces, the coefficient matrix $\mathbf{F}$ of training set can be partitioned into two parts - union of subspaces and corresponding coefficients - via the following procedures.

Since each vector $\vec{f_k}$ has been clustered into the belonging subspace during the subspace identification process, the corresponding coefficients for each $\vec{f_k}$ can be obtained accordingly. Suppose $\vec{f_k}$ lives in subspace $\mathbf{A}_i$ which is spanned by n_i orthogonal basis, so its corresponding coefficients $\vec{c}_k$ can be calculated using LS estimator:

$$\vec{c}_k = (\mathbf{A}_i^T \mathbf{A}_i)^{-1} \mathbf{A}_i^T \vec{f_k} \tag{3.5}$$

Then $\vec{f_k}$ can be characterized by $\vec{c}_k$ in its subspace

$$\vec{f_k} = \mathbf{A}_i \vec{c}_k \tag{3.6}$$

If there are totally J subspaces identified from $\mathbf{F}$, a structured dictionary constructed by concatenating all deformation subspaces is established as $\mathbf{D} = \bigcup_{i=1}^{J} \{\mathbf{A}_i\}$, with dimension $I = \sum_{i=1}^{J} n_i$. Since each vector $\vec{f_k}$ lies in one of the subspaces, $\vec{f_k}$ can also be represented in the structured dictionary with a block sparse vector $\{\tilde{\vec{c}}_k\}$, which is obtained via extending the coefficients $\{\vec{c}_k\}_{k=1}^{K}$ by zero padding in positions corresponding to other subspaces in $\mathbf{D}$. If $\vec{f_1}$ lies in subspace $\mathbf{A}_2$ which are spanned by the 5^{th}, 6^{th} and 7^{th} columns in $\mathbf{D}$, then

$\tilde{\vec{c}}_1$ has nonzero values only at index of 5, 6 and 7. Consequently, $\mathbf{F}$ can be factorized as

$$\mathbf{F} = \mathbf{DC} \tag{3.7}$$

where $\mathbf{C} = \left| \begin{array}{cccc} \tilde{\vec{c}}_1 & \tilde{\vec{c}}_2 & \cdots & \tilde{\vec{c}}_K \end{array} \right|_{I \times K}$ is the corresponding coefficient matrix with block sparsity.

3.2.3 Step 3: Structured Sparse Surface Representation

A. *Sparse Representation of Training Surfaces*

Integrating the subspace pursuing results in the harmonic domain in Eq. 6.2 with the initial SHD process in Eq. 5.3, the training deformations $\mathbf{X}$ can be sparsely represented in the original spatial domain as:

$$\begin{aligned} \mathbf{X} &= \mathbf{YDC} \\ &= \mathbf{GC} \end{aligned} \tag{3.7}$$

where $\mathbf{G} = \mathbf{YD}$ with size of $N \times I$ is the desired structured dictionary in the spatial domain. Since $\mathbf{D} = \bigcup_{i=1}^{J} \{\mathbf{A}_i\}$, $\mathbf{G}$ is inherently structured by subspaces of $\mathbf{G} = \bigcup_{i=1}^{J} \{\mathbf{G}_i\}$ with $\mathbf{G}_i = \mathbf{YA}_i$ of size $N \times n_i$.

Up to this point, with matrix $\mathbf{G}$ that captures the deformation features in the considered population, each training deformation $\mathbf{x}_k$ in $\mathbf{X}$ can be fully characterized by a sparse coefficient $\tilde{\vec{c}}_k$ as:

$$\mathbf{x}_k = \mathbf{G}\tilde{\vec{c}}_k \tag{3.8}$$

B. *Sparse Representation of Testing Surfaces*

For the testing deformations beyond the training set, we utilized the fact that the dictionary identified from an extensive training data features good generalization such that any deformation of that particular population can be represented in the subspaces with

high accuracy. This is justified because organs only deform in limited ways due to their mechanical properties, so the deformation variations can be fully learned from a training data set. This applied structure allows fast deformation representation in subspaces of low dimensionality.

The testing set is denoted as $\mathbf{H} = \{\mathbf{h}_m\}_{m=1}^{M}$, where M is the number of deformations to be represented. The straightforward strategy is to find a best-fit subspace for $\mathbf{h}_m$ by projecting it to every subspace $\{\mathbf{G}_i\}_{i=1}^{J}$ and choose the subspace with minimal projection error. Since the number of subspaces J and the dimension of each subspace $\{n_i\}_{i=1}^{J}$ are both small with the post-processing of subspace pruning, this best-fit strategy still results in low computational cost. However, when the number of subspaces is too large, an alternative threshold approach can be applied by finding a subspace $\mathbf{G}_i$ in which $\mathbf{h}_m$ can be represented with an error level smaller than η. The former best-fit method is implemented in our experiments for performance validation.

Suppose $\mathbf{G}_{i^*}$ is the chosen subspace, so coefficient vector $\vec{c}_m$ can estimated with LS as:

$$\vec{c}_m = (\mathbf{G}_{i^*}^T \mathbf{G}_{i^*})^{-1} \mathbf{G}_{i^*}^T \mathbf{h}_m \tag{3.9}$$

Then block sparse vector $\tilde{\vec{c}}_m = [0\ 0\ \cdots\ \vec{c}_m \cdots\ 0\ 0\ 0]$ is obtained according to the rules described in Subsection 3.2.2. Further, the sparsity of $\tilde{\vec{c}}_k$ or $\tilde{\vec{c}}_m$ can be increased by trimming off non-zero elements with absolute value lower than a given threshold δ.

Note that the subspace dimension n_i is substantially smaller than either N or $(L+1)^2$. Further, different from the traditional learning approaches based on Orthogonal Least Square (OLS) or Matching Pursuit (MP) algorithms which pick atoms from the training data and re-combine them for each surface description, we avoid this heavy overload of re-shuffling all the atoms by applying the block structure of the dictionary learned from a training data set. This structure and the low dimensionality of subspaces essentially enable the reconstruction of the complete surface from incomplete sparse samples with high accuracy and low computational cost.

3.2.4 Extended Sparse Surface Representation

For an organ with both interior and exterior surfaces, such as bladder, deformations can take place on both layers. The above theory can be extended to achieve sparse surface representation for deformations occurred on both interior and exterior wall of the object.

Initially, spherical parameterization is conducted on interior and exterior parts separately. We denote $\vec{x}_k^{\,in}$ and $\vec{x}_k^{\,ex}(1 \leq k \leq K)$ as the corresponding interior and exterior of each training surface $\vec{x}_k$. Then each pair of $\vec{x}_k^{\,in}$ (with N_1 vertices) and $\vec{x}_k^{\,ex}$ (with N_2 vertices) can be approximated by spherical harmonic basis as

$$\vec{x}_k = \begin{bmatrix} \widehat{\vec{x}_k^{\,in}} \\ \widehat{\vec{x}_k^{\,ex}} \end{bmatrix} = \begin{bmatrix} \mathbf{Y}^{in} & O \\ O & \mathbf{Y}^{ex} \end{bmatrix} \cdot \begin{bmatrix} \vec{f}_k^{\,in} \\ \vec{f}_k^{\,ex} \end{bmatrix} \tag{3.10}$$

where $\mathbf{Y}^{in}$ of size $N_1 \times (L+1)^2$ and $\mathbf{Y}^{ex}$ of size $N_2 \times (L+1)^2$ denote the spherical harmonic basis for inner and outer surfaces respectively. L is the highest degree of harmonics included. $\vec{f}_k^{\,in}$ and $\vec{f}_k^{\,ex}$ are the corresponding harmonic coefficient vectors. Therefore, each deformation is represented by vector $\vec{f}_k = \begin{bmatrix} \vec{f}_k^{\,in} \\ \vec{f}_k^{\,ex} \end{bmatrix}$, and all K training frames can be characterized by $F = \bigcup\{\vec{f}_k\}_{k=1}^{K}$ as

$$\mathbf{X} = \mathbf{YF} = \begin{bmatrix} \mathbf{Y}^{in} & O \\ O & \mathbf{Y}^{ex} \end{bmatrix} \begin{bmatrix} \vec{f}_1^{\,in} \ ... \ \vec{f}_K^{\,in} \\ \vec{f}_1^{\,ex} \ ... \ \vec{f}_K^{\,ex} \end{bmatrix} \tag{3.11}$$

The following procedures of subspace identification and sparse surface representation as described in Sec. 3.2.2 and Sec. 3.2.3 can be applied straightforwardly. After identifying J subspaces $\mathbf{D} = \bigcup_{i=1}^{J}\{\mathbf{A}_i\}$ from SH coefficient matrix $\mathbf{F}$, each training deformation can be

sparsely represented with block sparse coefficient vector $\tilde{\vec{c}}_k$ as:

$$\vec{x}_k = \begin{bmatrix} \widehat{\vec{x}_k^{\,in}} \\ \widehat{\vec{x}_k^{\,ex}} \end{bmatrix} = \begin{bmatrix} \mathbf{Y}^{in} & O \\ O & \mathbf{Y}^{ex} \end{bmatrix} \mathbf{D}\tilde{\vec{c}}_k = \mathbf{G}\tilde{\vec{c}}_k = \mathbf{G}_i\vec{c}_k \tag{3.11}$$

where $\mathbf{G}_i = \begin{bmatrix} \mathbf{Y}^{in} & O \\ O & \mathbf{Y}^{ex} \end{bmatrix} \mathbf{A}_i$ is the subspace with size of $(N_1+N_2)\times n_i$ and $\mathbf{G} = \bigcup_{i=1}^{J}\{\mathbf{G}_i\}$ is the desired structured dictionary. Accordingly, $\tilde{\vec{c}}_k$ is the block sparse vector, and $\vec{c}_k$ is the non-zero coefficient values in the selected subspace.

3.3 Experiment

Three types of experiments are conducted to demonstrate the feasibility of the proposed SRDS algorithm. The computer generated FEM data is first used to demonstrate that the SRDS approach matches the accuracy of complex mathematical modeling techniques, then an ex-vivo experiment is conducted using 3D MRI scans of porcine kidneys for evaluation in practical settings, and finally in-vivo experiment is carried over dynamic cardiac MRI scans for evaluation in real patients.

3.3.1 Experiment with FEM Data

Three representative organs are employed in this FEM experiment: 3D cortical mesh as an example of complicated shapes, gallbladder as an instance with geometrically simple shape, and bladder consisting of both interior and exterior walls.

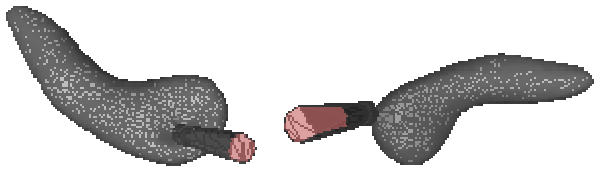

(a) (b)

Figure 3.3: Gallbladder deformation generated by surgical simulator.

3.3.1.1 Computer Model Setup

The initial 3D models of different organs are fed into a FEM based surgical simulation tool to generate deformation data for testing. For instance, Fig.4.9 demonstrates two examples of shape distortions due to the endoscope poking and grasping one side of the gallbladder.

Table 4.1 lists the FEM experimental setup of the three organs including number of vertices N, SH level L, number of deformations for training K and testing M. "GBL" stands for gallbladder in all the tables. The maximum SH level used for brain model is chosen according to [89], and the levels for gallbladder and bladder are determined when the SHD representation error is below 0.1% (EOF). The complex brain structure requires more vertices and higher SH level for surface representation to achieve sufficient accuracy. To evaluate the representation precision qualitatively, an evaluation parameter EOF is defined as the normalized Euclidean distance between the original surface and the reconstructed surface

$$EOF = \frac{\| \hat{\mathbf{x}}_k - \mathbf{x}_k \|_2}{\| \mathbf{x}_k \|_2} \tag{3.12}$$

All surfaces are centered to the origin of the coordinate system so that EOF will not be heavily affected by the denominator.

Table 3.1: FEM Model setup

	Vertices N	SH level L	Training K	Testing M
Brain	40962	80	35	35
GBL	3038	25	250	114
Bladder	N1=4434, N2=4274	30	74	46

3.3.1.2 Results

With the FEM data, the proposed SRDS algorithm is evaluated from three perspectives: (1) subspace dimensionality, (2) sparsity and accuracy of representations, and (3) the effect of subspace pursuit threshold ε and coefficient truncation threshold δ on the performance.

The sparsity is defined as the l_0 norm of the coefficient vector $\tilde{\vec{c}}_m$.

A. *Training Results*

During training stage, we set $\varepsilon = 0.005$ for subspace detection, $\eta = 0.01$ for clustering, $E_{max} = 50$ as the maximum iteration times and $\delta = 0.005$ for coefficient truncation. Subspaces on X, Y and Z axis are identified separately. Table 3.2 shows that the subspace number J and dimensions of resulting dictionary ($dim(G) = I$) are markedly small relative to N or L^2 in all three tests. We notice that the subspace dimensions of brain are relatively smaller than the other two. This is because of smaller training data size and minor extent of deformation considered in the brain experiment, which results in smaller dictionary size to capture the deformation features.

Table 3.2: Dimension of dictionary(J/I)

	Brain	GBL	Bladder
Subspace on X (J/I)	2/13	2/39	1/37
Subspace on Y (J/I)	2/6	2/48	1/30
Subspace on Z (J/I)	1/3	1/42	1/34

Table 3.3: Sparsity(μ/σ) and accuracy evaluation

	X (μ/σ)	Y (μ/σ)	Z (μ/σ)	EOF(%)
Brain Train(SRDS)	3.1/0.2	3.4/0.9	3.0/0.2	1.31
Brain Test(SRDS)	3.5/0.5	3.9/0.4	3.0/0.0	1.32
Brain Test(OSP)	4.1/0.6	4.5/0.5	3.9/0.8	1.30
GBL Train(SRDS)	25.8/12.2	4.8/1.8	32.3/7.3	0.13
GBL Test(SRDS)	33.2/1.0	44.1/1.1	40.8/1.3	0.15
GBL Test(OSP)	44.4/4.0	48.3/2.3	43.9/4.5	0.13
Bladder Train(SRDS)	24.1/3.7	20.8/2.9	24.8/4.0	0.076
Bladder Test(SRDS)	24.6/2.7	21.0/2.5	25.6/3.2	0.073
Bladder Test(OSP)	22.5/4.3	16.3/6.5	23.0/5.2	0.070

B.*Sparsity and Accuracy Evaluation*

Sparsity is examined in terms of (μ/σ), where μ is the average l_0 norm of the coefficient vector $\tilde{\vec{c}}_k$(training) or $\tilde{\vec{c}}_m$(testing) and σ is the corresponding standard deviation. To verify that whether our method achieves equivalent sparsity and precision when applying the structure of the dictionary, we also test the case without relying on any structure learned from training set, during which sparse representation of each deformation in the testing set is

re-pursued from the training set using OSP approach. In the following tables, we use "OSP" to refer to the results obtained using such a re-pursuing process. Table 3.3 summarizes the sparsity of the SRDS representation of three organs for both training and testing set. It illustrates that the number of atoms needed for representing the complex deformations is much smaller than the dimension of spherical harmonic vectors ($(L+1)^2$), and particularly the sparsity and accuracy via SRDS is very close to that from OSP re-pursuit for the testing deformations, which indicates the good generalization of the structured dictionary.

The reconstruction error in terms of EOF is further compared with that from standard SHD method, as shown in Fig.3.4. In general, the accuracy of SRDS is equivalent to that of SHD method. Specifically, it shows that the SRDS method achieves average EOF of 1.32% (brain) and 0.14% (gallbladder) versus 1.29% (brain) and 0.13% (gallbladder) with SHD method. For bladder model with deformations on multiple layers, the overall representation error with SRDS is 0.07%, very close to 0.06% with SHD. Fig.3.8 - Fig.3.9 show typical reconstructed deformations of the testing data for the three organs with SHD and SRDS methods. Fig.3.9(e) and Fig.3.9(f) demonstrate the interior and exterior representation of the bladder at a same time instance. From those results, we can see that the SRDS algorithm achieves the accuracy equivalent to complex mathematical modeling techniques while significantly lowers the representation dimensionality.

C. *Effect of* ε

The performance of SRDS algorithm is examined as the subspace pursuit threshold ε varies. Specifically, we study the effect of ε on the dimensionality (I) of the structured dictionary G, sparsity and accuracy of the surface representation. Fig.3.5 shows how the subspace dimensions on three axis change during the training stage as ε increases from 0.001 to 0.01. Fig.3.6 displays the influence of ε on the average sparsity μ of the surface representation results for both training and testing data sets. In general, smaller ε leads to larger subspace size and less description sparsity, since lower ε usually leads to more recruited atoms to meet the desired representation accuracy. Therefore, there is a tradeoff between representation accuracy and desired sparsity. Fig.3.7 reveals the representation EOF as a

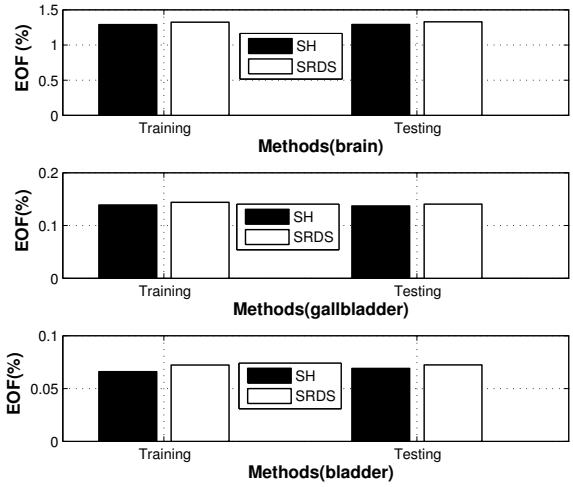

Figure 3.4: EOF of brain, gallbladder and bladder reconstruction with SHD and SRDS methods. The left pair is for training set; the right pair is for testing set.

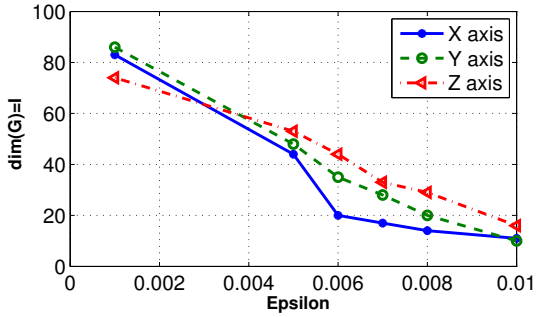

Figure 3.5: Dimension I of trained dictionary G decreases on all three axis as ε increases.

function of ε. Not surprisingly, the reconstruction error is increased as ε becomes larger. An empirical point can be chosen according to the training curve when space dimension I expands significantly but only trivial EOF improvement is gained, i.e. $\varepsilon = 0.005$ is a preferred value in this test according to Fig.3.7.

D. *Effect of* δ

The influence of coefficient truncation threshold δ on the performance of SRDS algorithm is also tested, while δ is varied among [00.0001 0.0005 0.001 0.005 0.01 0.05 0.08 0.1]. Fig. 3.10 shows the effect of δ on the average sparsity μ of the surface representation results. We can see that, as the truncation threshold δ enlarges, the sparsity of the representation

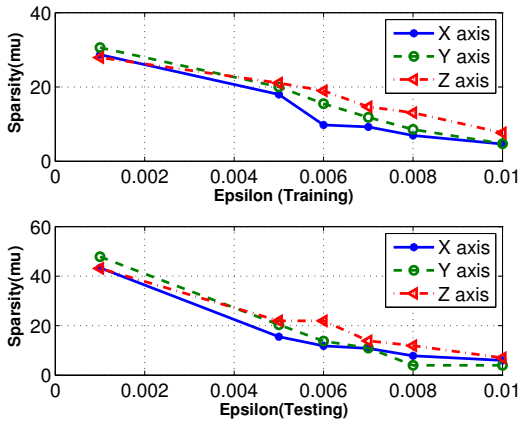

Figure 3.6: Sparsity (μ) of surface representation changes with different ε on three axis: the top graph is for training set; the bottom graph is for testing set.

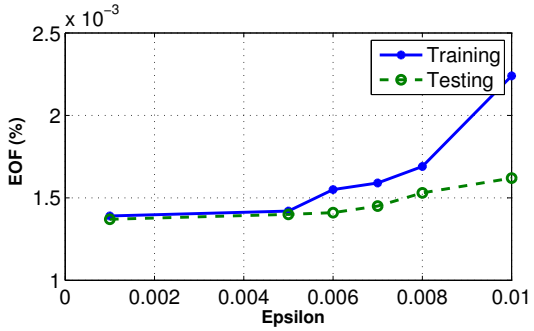

Figure 3.7: EOF of gallbladder reconstruction increases as ε gets larger for both training and testing sets.

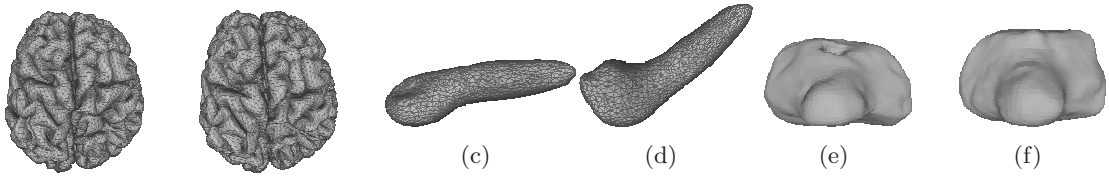

(a) (b) (c) (d) (e) (f)

Figure 3.8: Reconstructed brain deformations using SHD approach: (a) is the initial brain shape and the circle marks one typical area under deformation, (b)-(e) are the reconstructed brain deformations.

is increased for both training and testing data sets at the price of decreased representation error as shown in Fig. 3.11, so there is tradeoff between sparsity and accuracy. Empirically, one can choose the δ value when the representation precision remarkably deteriorates while

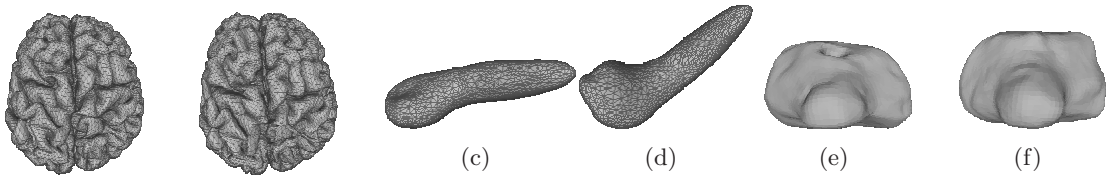

Figure 3.9: Reconstructed brain deformations using SRDS approach: (a) is the initial brain shape, (b)-(e) are the reconstructed brain deformations.

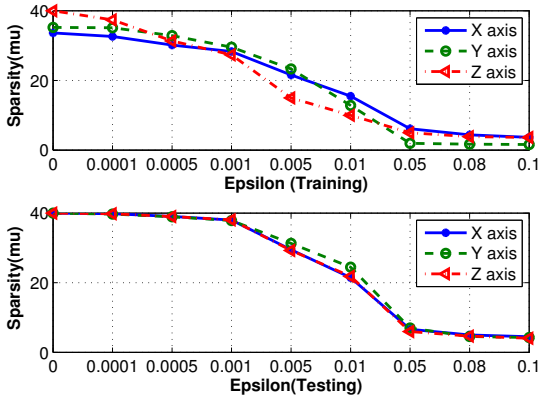

Figure 3.10: Sparsity (μ) of surface representation changes with different δ on three axis: the top graph is for training set; the bottom graph is for testing set.

the sparsity is still increasing. Therefore, according to Fig. 3.10 and Fig. 3.11, an appropriate value for δ is between 0.005 and 0.01.

3.3.2 Ex-vivo experiment using MRI

To evaluate the proposed algorithm in real applications, an ex-vivo experiment using three porcine kidneys were conducted at the Center for Interdisciplinary Applications in Magnetic Resonance (CIA-MR) of University of Minnesota. Deformations imposed to each kidney were controlled and maintained still during imaging by a customized non-magnetic mechanical device as shown in Fig.3.12. Each deformed kidney shape was scanned in 3D MRI mode with spatial resolution of 1.2 mm to generate both training set and testing set. The SH degree L of the organ representation is set to be 20, and each 3D kidney mesh after surface correspondence has $N = 4002$ vertices.

Both intra-model and inter-model experiments are conducted. The former uses training

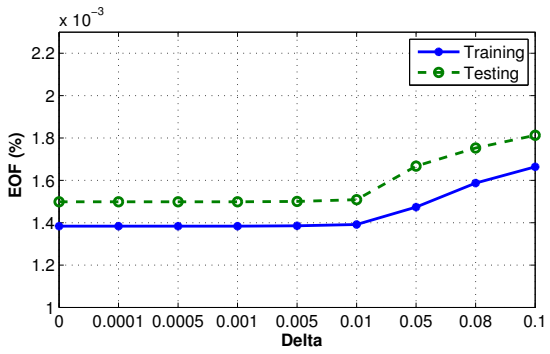

Figure 3.11: EOF of gallbladder reconstruction increases as δ gets larger for both training and testing sets.

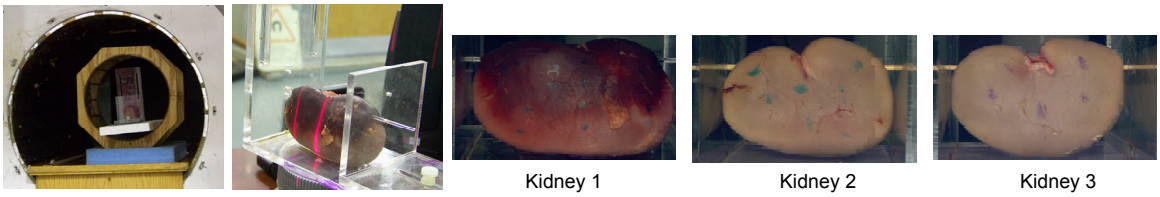

Figure 3.12: Images of three porcine kidneys for experiment.

and testing deformations from the same kidney; the later utilizes two out of the three kidneys for training and the third one for testing in a cross evaluation fashion. Besides sparsity and EOF, Hausdorff distance between the represented shape and corresponding MRI surface is also examined as a physical measurement of error. The Hausdorff distance between surface x and $x^{'}$ is defined as

$$d(x, x^{'}) = \max_{p \in x} d(p, x^{'}) \tag{3.13}$$

where $d(p, x^{'})$ is defined as the distance between a point p on surface x and the closest point on surface $x^{'}$, i.e.

$$d(p, x^{'}) = \min_{p^{'} \in x^{'}} ||p, p^{'}||_2 \tag{3.14}$$

with $||.||_2$ denoting the Euclidean norm.

3.3.2.1 Intra-model Test

In the intra-model experiment, 31 deformations of the same kidney were generated and scanned by the MRI machine, among which 20 frames were randomly selected as training set and the other 11 were applied for testing the generalization of the learned subspaces.

Table 3.4 shows the trained subspace dimensions (J as number of subspace, I as dictionary size of $\mathbf{G}$), the sparsity of the descriptors in each axis for both training set and testing set, and the corresponding errors in terms of EOF and Hausdorff distance. Similar to the FEM experiment, the sparsity is also evaluated with OSP re-pursuit process in the testing set for comparison. The table shows that the sparsity and the accuracy achieved with SRDS is very close to that from OSP re-pursuing process. However, the SRDS method features delay-free surface representation by applying the structure in the identified dictionary. Further results about computational efficiency are shown in Sec. 3.3.4. One may notice that the size of training data in the MRI experiment is smaller than that in FEM test due to the less availability of 3D MRI images. As a rule of thumb, larger training set carries richer deformation information and thus leads to better generalization of the dictionary. However, given the size of training data and extent of deformation involved in the ex-vivo experiment, high representation precision is still achieved.

Table 3.4: Subspace dimension and sparsity (μ/σ) for intra-model experiment

	X (μ/σ)	Y (μ/σ)	Z (μ/σ)	EOF (%)	Haus (mm)
J/I	1/17	2/31	2/31		
Train(SRDS)	16.9 / 0.4	15.5 / 1.5	15.8 / 1.5	0.24	0.55
Test(SRDS)	17.0 / 0.0	16.9 / 0.3	16.7 / 0.9	0.64	0.87
Test(OSP)	16.6 / 1.5	16.3 / 0.9	17.1 / 0.8	0.60	0.85

Fig.3.13 illustrates the accuracy of the surface representation in the intra-model test. The average EOF in Fig.3.13(a) for training set is 0.24% and 0.64% for testing set, with maximum rate less than 1%. Further, error as Hausdorff distance (shown in Fig.3.13(b)) is 0.55 ± 0.23 mm with $95th$ percentile error of 0.86 mm for the training set, and 0.87 ± 0.10

mm with $95th$ percentile error of 0.96 mm for the testing set. This intra-model experiment demonstrated that the SRDS algorithm identifies subspaces generalizable enough to accurately represent deformations beyond the training set for the same object.

Fig.3.14 visualizes the color-coded error distribution at all vertices on the represented surface with SRDS relative to the actual MRI scans. Fig.3.14(a) illustrates the error range for different colors. Fig.3.14(b) and Fig.3.14(d) show the error distribution for a typical reconstruction in the training and testing set, respectively. Fig.3.14(c) and Fig.3.14(e) show maximum 90% level reconstruction errors, i.e., 90% of all deformations in the training or testing set have representation point errors less than the values shown in the figures. Consistent with the EOF and Hausdorff distance results, the color diffusion in Fig.3.14 indicates that the precision in the testing group is relatively lower than that in the training group. However, among all the pixel-wise errors shown in Fig.3.14(e), less than 3% of all the surface points have error distance larger than 0.5 mm.

3.3.2.2 Inter-model Test

Three inter-model experiments are performed to further validate the proposed SRDS method applied to organs from different subjects. In the following context, "Ex1" stands for the experiment training on Kidney 2 & 3 plus one initial shape of Kidney 1 while testing on deformations of Kidney 1, and the like for "Ex2" and "Ex3". In each experiment, both sparsity and accuracy are examined.

The number of subspaces (J) and dimensions (I) of the identified dictionary are listed

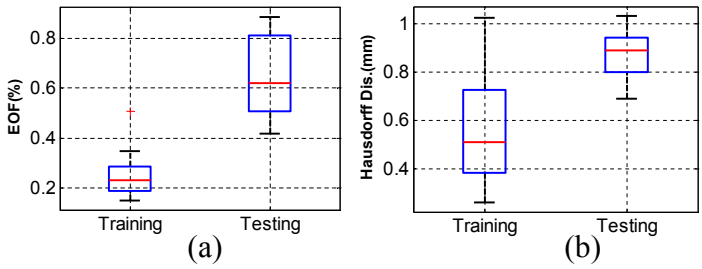

Figure 3.13: Boxplots of representation error in intra-model experiment: (a) EOF of training and testing set, (b) Hausdorff distance of training and testing sets

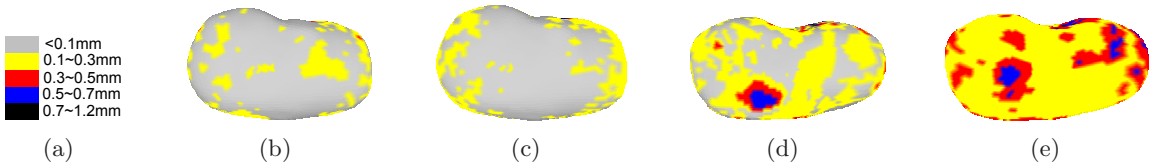

(a) (b) (c) (d) (e)

Figure 3.14: Representation error in intra-model experiment: (a) color-coded scales, (b) example representation error in training set, (c) 90% representation error in training set, (d) example of representation error in testing set, (e) 90% representation error of testing set

Table 3.5: Subspace dimension (J/I) in inter-model experiments

	X axis	Y axis	Z axis
Ex1 (J/I)	1/36	1/37	1/37
Ex2 (J/I)	2/87	2/86	2/87
Ex3 (J/I)	3/79	2/88	3/83

Table 3.6: Sparsity (μ/σ) and accuracy evaluation for inter-model experiment with kidneys

	X (μ/σ)	Y (μ/σ)	Z (μ/σ)	EOF (%)	Haus (mm)
Ex1 Train (SRDS)	34.7/5.5	35.6/5.5	36.4/1.6	0.32	0.69
Ex1 Test (SRDS)	35.7/1.3	36.7/0.9	36.7/1.8	2.01	2.08
Ex1 Test (OSP)	36.7/2.4	36.0/2.4	35.9/2.6	1.94	1.94
Ex2 Train (SRDS)	42.8/4.5	42.8/2.2	43.5/3.7	0.26	0.59
Ex2 Test (SRDS)	47.0/3.1	44.5/1.8	46.3/2.4	1.02	1.27
Ex2 Test (OSP)	44.0/2.2	41.9/12.1	45.9/2.0	0.95	1.22
Ex3 Train (SRDS)	37.1/9.1	43.3/2.2	40.8/1.3	0.25	0.59
Ex3 Test (SRDS)	41.4/6.5	45.1/1.7	40.4/1.3	0.90	1.18
Ex3 Test (OSP)	41.2/8.4	42.7/9.7	39.3/10.6	0.83	1.16

in Table. 4.4. The training results vary among the three experiments but all features low subspace dimensions. Table. 3.6 shows the sparsity of the inter-model experiments using the SRDS algorithm, and the error level is evaluated in terms of EOF and Hausdorff distance.

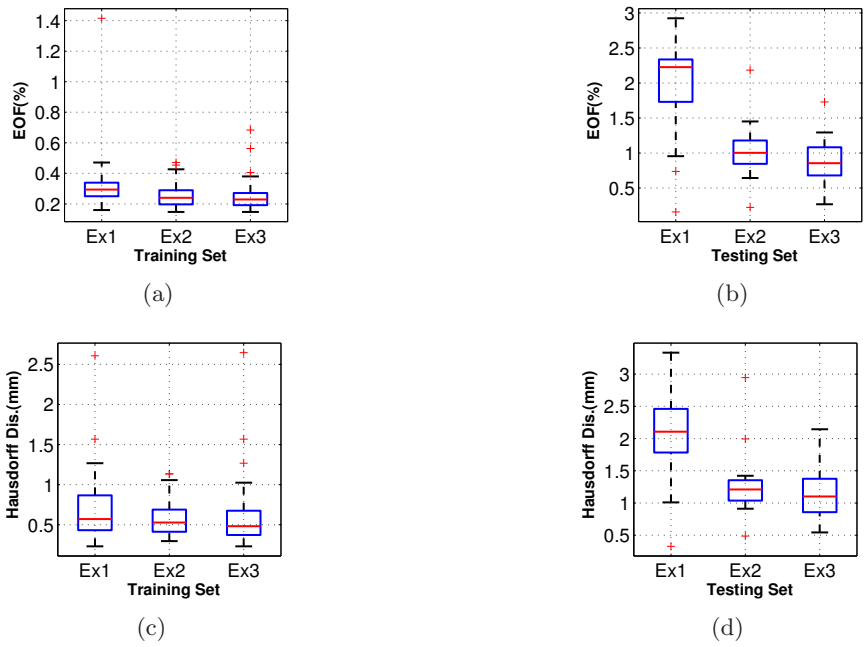

Figure 3.15: Boxplots of representation error in inter-model experiments: (a) EOF of training set, (b) EOF of testing set, (c) Hausdorff distance of training set, (d) Hausdorff distance of testing set

Each testing deformation is also sparsely re-trained using OSP for comparison. We can see that the sparsity and representation error resulting from SRDS method is very close to that using OSP.

Fig.3.15 shows the representation accuracy using SRDS algorithm in training and testing sets for the three tests. In general, the error in testing set is larger than that in the training set. Particularly, as for EOF evaluation, "Ex1" leads to the largest EOF error relative to "Ex2" and "Ex3" but the average error rate is still as low as 0.3% for training set and 2.0% for testing set. Table 3.7 lists the specific Hausdorff measurements corresponding to boxplots in Fig.3.15(c) and Fig.3.15(d), including minimum, $95th$ percentile and mean. We can see that the $95th$ percentile Hausdorff distance across all experiments is below 3 mm and the mean is belong 2.1 mm. Comparing those error levels with the intra-model test, one can see that the homology existing among the training and testing deformations contributes to better dictionary generalization and thus leads to higher representation accuracy.

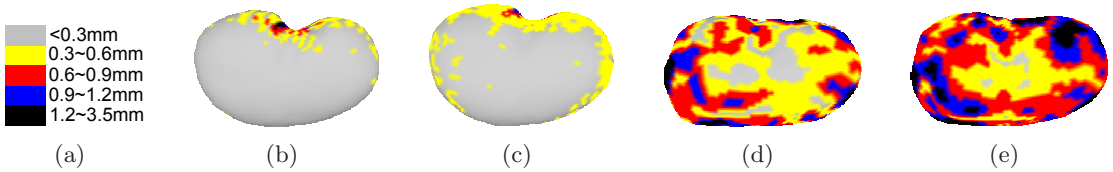

Figure 3.16: Representation Error in inter-model Ex1: (a) color-coded scales, (b) example of color-coded point error in training set, (c) 90% color-coded point error in training set, (d) example of color-coded point error in testing set, (e) 90% color-coded point error of testing set

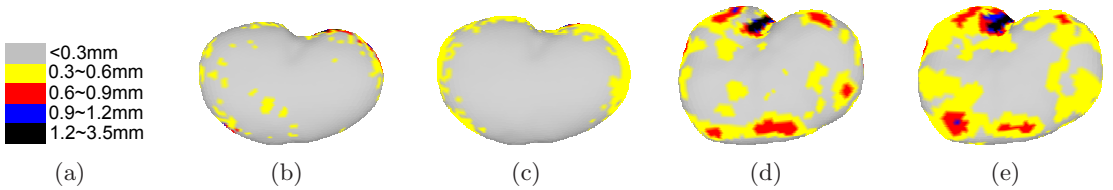

Figure 3.17: Representation Error in inter-model Ex2: (a) color-coded scales, (b) example of color-coded point error in training set, (c) 90% color-coded point error in training set, (d) example of color-coded point error in testing set, (e) 90% color-coded point error of testing set

Table 3.7: Hausdorff distance for inter-model experiment with kidneys

	Min(mm)	$95th$(mm)	Mean(mm)
Ex1 Train	0.23	1.14	0.69 ± 0.42
Ex1 Test	0.33	2.81	2.08 ± 0.61
Ex2 Train	0.30	1.03	0.59 ± 0.23
Ex2 Test	0.49	1.99	1.27 ± 0.49
Ex3 Train	0.23	1.03	0.59 ± 0.39
Ex3 Test	0.54	1.74	1.18 ± 0.44

Fig.3.16, Fig.3.17 and Fig.3.18 show the color-coded error fields of a typical representation and at the maximum 90% level for the three inter-model experiments. In either training set or testing set, it is observed that large errors are mostly distributed around the edge area where local details are rich. Consistent with the previous EOF and Hausdorff distance measurements, the color diffusion in Fig.3.16-Fig.3.18 indicates that errors in testing set is larger than that in training set and "Ex1" generates relatively larger error comparing to "Ex2" or "Ex3".

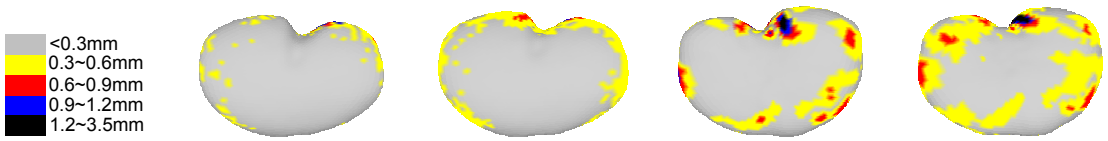

(a) (b) (c) (d) (e)

Figure 3.18: Representation Error in inter-model Ex3: (a) color-coded scales, (b) example of color-coded point error in training set, (c) 90% color-coded point error in training set, (d) example of color-coded point error in testing set, (e) 90% color-coded point error of testing set

3.3.3 In-vivo experiment using MRI

The proposed approach is also tested over the in-vivo cardiac MR images [151], consisting of automatically segmented images from volumetric MRI scans of a diastole-systole-diastole cycle. For each patient, there are around 22 phases in a cardiac cycle. Since the generated surfaces from automatic segmentation software are quite rough, we use the spherical harmonic representation as a filter to smooth out those surface noises, and then apply the smoothed surfaces as training and testing data. Therefore, the demonstrated error in this section is relative to the SHD surfaces, not to the original raw surfaces. The iter-patient results are reported as follows.

Similar to the ex-vivo test, we use the segmented left ventricles (LV) of 2 different patients plus an initial LV surface for the third patient as training data, and the remaining LV shapes in a beating cycle of the third patient are used to test the generalization of the

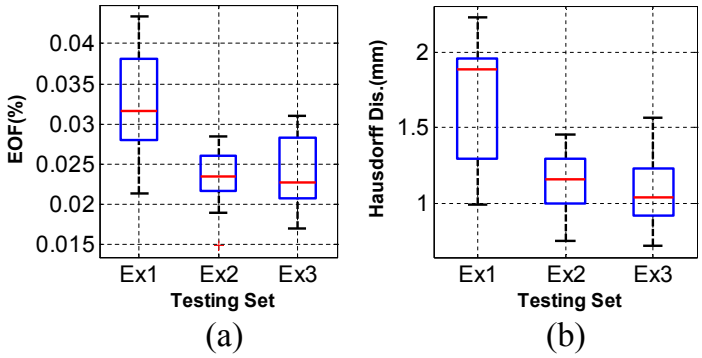

Figure 3.19: Boxplots of representation error in LV inter-patient experiments: (a)EOF, (b)Hausdorff distance

Table 3.8: Sparsity (μ/σ) along X, Y, Z axis and accuracy of in-vivo LV tests

	X (μ/σ)	Y (μ/σ)	Z (μ/σ)	EOF (%)	Haus (mm)
Ex1 Train (SRDS)	37.0/0.0	35.4/0.5	31.7/9.0	0.13	0.08
Ex1 Test (SRDS)	37.0/0.0	36.0/0.0	34.6/1.5	3.21	1.07
Ex1 Test (OSP)	33.3/10.5	36.8/2.6	33.8/9.2	2.92	0.98
Ex2 Train (SRDS)	35.4/7.4	32.8/14.1	32.4/3.3	0.17	0.10
Ex2 Test (SRDS)	38.0/0.0	37.0/0.0	34.0/0.0	2.31	1.15
Ex2 Test (OSP)	32.1/6.3	24.0/10.5	32.3/6.5	1.93	1.07
Ex3 Train (SRDS)	36.7/3.2	38.8/1.5	38.4/0.5	0.12	0.07
Ex3 Test (SRDS)	39.6/1.2	40.0/0.0	38.8/0.4	2.33	1.09
Ex3 Test (OSP)	32.7/11.5	33.4/11.3	30.1/12.2	1.98	0.99

Table 3.9: Hausdorff distance for in-vivo experiment with LV

	Min(mm)	$95th$(mm)	Mean(mm)
Ex1 Train	0	0.50	0.08 ± 0.18
Ex1 Test	0.99	2.16	1.67 ± 0.39
Ex2 Train	0	0.63	0.10 ± 0.24
Ex2 Test	0.75	1.37	1.14 ± 0.18
Ex3 Train	0	0.60	0.07 ± 0.21
Ex3 Test	0.72	1.46	1.09 ± 0.24

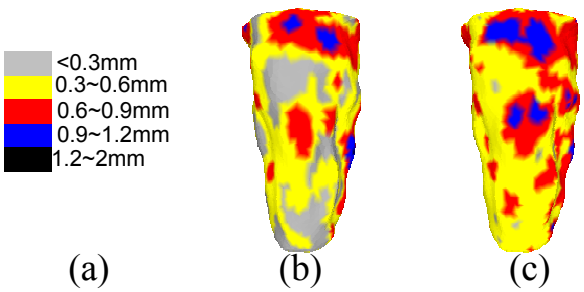

Figure 3.20: Representation error in in-vivo LV experiment: (a) color-coded scales, (b) example representation error in testing set, (c) 90% representation error of testing set

identified subspaces. The formulated tests are noted as "Ex1", "Ex2" and "Ex3". Table 3.8 lists the sparsity test results of the three cross validations for both training and testing sets. We can see that the sparsity in the training set is close to that in the testing set, but the former achieves much higher accuracy. This is because that the identified subspaces generalize perfectly for those elected atoms among the training set after spherical harmonic smoothing. Consistent with the previous experiments, the representation of testing surfaces using SRDS is also compared with that using re-pursuing OSP. According to the results, SRDS achieves performance slightly worse than but close to that of OSP. However, as demonstrated in Sec. 3.3.4, without relying on the structured dictionary learned from the training population, OSP is a computational expensive task since for each testing surface it requires to research for atoms from the training set to achieve sparse representation.

Fig. 3.19 provides boxplots for the representation accuracy of the testing set in terms of EOF and Hausdorff distance. Table 3.9 provides the minimum, $95th$ percentile and mean Hausdorff measurements corresponding to Fig. 3.19(b). In coincidence, "Ex1" leads to slightly larger errors than the other two tests, with average EOF of 3.2% ("Ex1"), and mean Hausdorff distance of 1.67 ± 0.39 mm. The $95th$ percentile Hausdorff distance across all experiments is below 2.2 mm. Fig. 3.20(b)(c) shows the color-coded error field of a typical representation and at the maximum 90% level for the testing set in one inter-patient experiment (c). As indicated by the color distribution, majority of the point errors are below 0.9 mm. Particularly, in the 90th percentile evaluation in Fig. 3.20, only 3% of all the point-wise errors are above 0.9 mm.

3.3.4 Efficiency

To examine the efficiency of the proposed SRDS method quantitatively, the computational time to represent each surface in the testing set using SRDS method is compared with that resulting from OSP re-pursuing approach for the above five organs. The results are summarized in Table. 3.10, including training set size K, maximum SH level L, average time(in seconds) required with SRDS(t_1) and OSP(t_2) respectively, and the ratio between

the two. As shown in Table. 3.10, the time consumption for seeking sparse representation of the testing surfaces using the SRDS is at least 10 times lower than that using the original OSP method which does not rely on the dictionary structure learned from the training data set. The advantage is more pronounced when the training data size K or the SH level L is large. For example, in the brain model, the high SH level L leads to substantial computational delay during the search for proper atoms for representation, such that the SRDS achieves a speed orders of magnitude faster than the OSP method without training. On the other hand, for the case of gallbladder, the large training size also increases the time used by re-pursuing OSP, so it runs 65 times slower than SRDS.

To summarize, considering the test results for sparsity, accuracy and efficiency given in this experiment section, we can see that the proposed SRDS method achieves sparse surface representation with high computational efficiency and accuracy.

Table 3.10: Computational time of SRDS and OSP

	Training K	SH level L	SRDS (sec) t_1	OSP (sec) t_2	t_2/t_1
Brain	35	80	0.3	51.2	170.7
GBL	350	25	0.6	39.1	65.2
Bladder	74	30	2.5	57.2	22.9
Kidney	52	20	0.8	9.2	11.5
LV	51	25	0.5	6.9	13.8

3.4 Conclusion

This chapter introduced an algorithm for block sparse representation of deformable organ surfaces with high accuracy. The proposed SRDS design first identifies the deformation subspaces from the training data set in the transformed spherical harmonic domain, and then represents each deformed surface with a block sparse vector in the structured dictionary. SRDS is generalized to applications involving organs with multiple surface layers, such as bladder. The algorithm has been validated with FEM data and real 3D MRI scans under both ex-vivo and in-vivo conditions. The FEM test results demonstrate that SRDS

achieves accuracy matching that of complex mathematical modeling techniques. Further, the maximum representation error in ex-vivo experiment is below 1 mm for intra-model test and below 3 mm for inter-model test. For the in-vivo experiment, the SRDS achieves an accuracy of better than 2.5 mm.

The structured representation feature of SRDS algorithm enables efficient surface recovery from limited samples, as shown in Chapter 4 and Chapter 5. In addition, the merits of block sparse surface representation presented here can be applied to various medical organ modeling, shape classification, and similarity retrieval where reduced parameter dimension can potentially speed up the implementations.

Chapter 4

3D Visualization of Intraoperative Organ Deformations

4.1 Chapter Introduction

Restricted visualization of the surgical field is one of the most critical challenges for Minimally Invasive Surgery (MIS). Current intraoperative visualization systems are promising. However, they can hardly meet the requirements of high resolution and real-time 3D visualization of the surgical scene to support the recognition of anatomic structures for safe MIS procedures. This chapter presents a new approach for real-time 3D visualization of organ deformations based on optical imaging patches with limited field of view and a single preoperative MRI or CT scan. This approach aims to provide surgeons with real-time 3D visualization of complete organ deformations with high accuracy. The idea for reconstruction is motivated by the SRDS theory introduced in the previous Chapter. 3, which indicates that the spherical harmonic coefficients corresponding to distorted surfaces of a given organ lie in lower dimensional subspaces in a structured dictionary that can be learned from a set of representative training surfaces. The preoperative MRI or CT scan is used for registration and dictionary building, while the intraoperative optical patch images from limited views are used for real-time deformation reconstruction based on the trained dictionary.

The following are the main contributions of the chapter.

1. We develop a novel algorithm for real-time 3D reconstruction/visualization of the deformable organ shapes from the limited field of view based on the SRDS theory for structured surface representation.

2. The proposed algorithm is extended to reconstruct the interior structures of an organ by only sampling on the exterior surface.

3. We propose an implementation framework using MRI/CT scans and optical devices to achieve real-time 3D visualization of organ deformations. In particular, we address the involved issues of multi-modal surface registration and surface correspondence.

4. For verification, we provide evaluation results with both FEM and ex-vivo experiments. The latter are based on freshly excised porcine kidneys tested utilizing an MRI machine and a portable laser scanner. Practical issues of error propagation and computational cost during the reconstruction stage are also addressed.

The rest of the chapter is organized as follows. Section 4.2 describes the proposed algorithm of 3D surface reconstruction in details and Section 4.3 provides a framework for implementation by addressing the encountered practical issues. Section 4.4 presents some verification results using both FEM data and ex-vivo experiments. Finally, Section 4.5 concludes this chapter.

4.2 Algorithm

The framework of the proposed approach for 3D visualization of intraoperative organ deformations is outlined in Fig. 4.1. The intraoperative signal acquired with a limited field of view 3D laparoscopic or endoscopic camera is used in conjunction with a single preoperative MRI or CT scan, to display the reconstructed 3D organ images on a computer screen in real-time. Specifically, this approach consists of the following three steps.

1. Identifying deformation subspaces to construct a structured dictionary in which deformable surfaces can be represented sparsely with high accuracy;

2. Designing sampling strategies under different access constraints to determine appropriate sampling positions for reconstructing the deformations;

3. Reconstructing the surface of an organ in real-time with samples from the limited field of view using the structured dictionary.

This section describes the design details for each step, and generalizes the algorithm to applications involving organs with both interior and exterior surfaces.

4.2.1 Sparse Surface Representation

The sparse representation of the deformable organ surface is achieved via the SRDS approach introduced in the previous chapter. Here we briefly recall the SRDS method. It first transforms the training surfaces into the harmonic domain to decrease the training vector size and remove the high frequency components. Then OSP subspace pursuit is conducted in the transformed harmonic domain to identify the subspaces that can generalize deformation variations in the potential population. Finally, the sparse representation of each surface is obtained by combining the first two steps. Each surface $\mathbf{x}_k$ is described in the

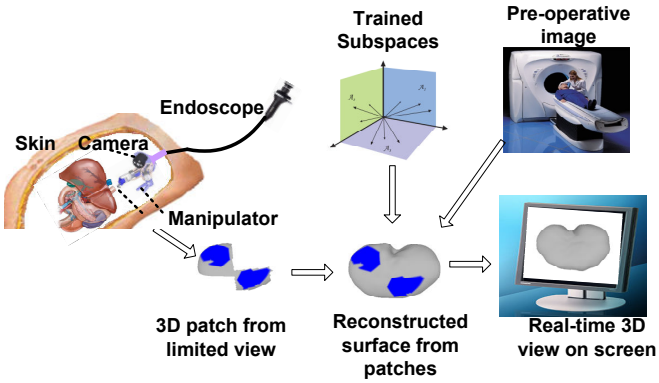

Figure 4.1: Framework of real-time 3D visualization of deformable organs.

original spatial domain by a sparse coefficient vector $\tilde{\vec{c}}_k$ as:

$$\mathbf{x}_k = \mathbf{G}\tilde{\vec{c}}_k = \mathbf{G_i}\vec{c}_k \tag{4.1}$$

where $\mathbf{G} = \bigcup_{i=1}^{J}\{\mathbf{G}_i\}$ with size of $N \times I$ is the desired structured dictionary in the spatial domain, and $\mathbf{G}_i$ is one of the J subspaces of size $N \times n_i$. $\tilde{\vec{c}}_k$ features block sparseness, and $\vec{c}_k$ is the corresponding non-zero coefficients.

4.2.2 Sampling Strategy Design

With the identified deformation dictionary $\mathbf{G}$ from the training procedure and the assumption that $\mathbf{G}$ is generalizable enough to catch the variations occurred in the testing population to be reconstructed, the sampling strategy design is to determine sampling locations to reconstruct new deformations using sparse surface samples in real-time. Three sampling strategies are studied in this chapter, as illustrated in Fig. 4.2. We first consider a completely random sampling method (Fig. 4.2(a)) assuming that the entire surface is accessible. Then we introduce patch sampling (Fig. 4.2(b)) and localized sampling (Fig. 4.2(c)) by imposing different constraints on the sampling location. The latter two methods are designed to address the visualization challenges of restricted access to the organ and limited field of view, encountered during the MIS operation.

4.2.2.1 Random Sampling

Since intersections may exist among those subspaces $\{\mathbf{G}_i\}_{i=1}^{J}$, orthogonality holds true only among atoms within each subspace $\mathbf{G}_i$. Thus sampling positions are designed based on each subspace $\mathbf{G}_i$. The philosophy behind the sampling position design is to find a well

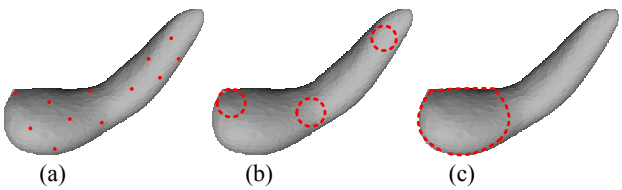

Figure 4.2: Three sampling strategies: (a) random, (b) patch, (c) local.

conditioned sub-matrix $\widetilde{\mathbf{G}}_i$ for each subspace, such that the coefficient vector $\vec{c}_{t,i}$ can be stably estimated with the LS estimator from the following linear system

$$\widetilde{\mathbf{h}}_{t,i} = \widetilde{\mathbf{G}}_i \vec{c}_{t,i} \tag{4.2}$$

where $\widetilde{\mathbf{h}}_{t,i}$ is the m_i sparse surface samples (m_i must be larger than n_i) and $\widetilde{\mathbf{G}}_i$ stands for the sub-matrix containing corresponding m_i rows of $\mathbf{G}_i$. Then the current deformation $\mathbf{h}_t$ can be reconstructed completely in the proper subspace with estimated coefficients $\hat{\vec{c}}_{t,i}$. The issue of finding an optimal subspace for final deformation reconstruction will be addressed in Sec. 4.2.3.

Since the basis in $\mathbf{G}_i$ is orthogonal, chances of getting a $\widetilde{\mathbf{G}}_i$ with a small condition number are high. Finding the $\widetilde{\mathbf{G}}_i$ with the smallest condition number is optimal in terms of numerical accuracy. However the searching complexity grows exponentially with the size of matrix $\mathbf{G}_i$ for exhausting all the possible $\widetilde{\mathbf{G}}_i$. A "random walk" approach is applied instead. We randomly pick m_i rows from $\mathbf{G}_i$ to form $\widetilde{\mathbf{G}}_i$ for a predefined number of tries (e.g., 1000 times in our experiments), choose the sub-matrix $\widetilde{\mathbf{G}}_i$ with the smallest condition number and record the index set of the chosen rows of that sub-matrix as $S_i = \{s_{i,1}, s_{i,2}, \cdots, s_{i,m_i}\}$. Ideally, such a random walk process should be run for each subspace to obtain its unique S_i. A more economic but less accurate approach is to conduct random walk on all subspaces simultaneously. That is, the indices of chosen rows for all sub-matrices $\{\widetilde{\mathbf{G}}_i\}_{i=1}^{J}$ are the same. Then the index set leading to the least condition number (averaging across all sub-matrices) is chosen as the common S_i for all subspaces.

4.2.2.2 Patch Sampling

In reality, only a small number of observation instruments (such as fiber optics) or limited field of view of the organ surface are available, so completely random sampling is hard to implement. To meet those practical constraints, patch sampling (Fig. 4.2(b)) and localized sampling (Fig. 4.2(c)) strategies are introduced for determining sampling locations with the

imposed restrictions.

With patch sampling, all the surface vertices are initially grouped into small patches so that samples within each patch can be retrieved using a miniature instrument such as a single fiber optic camera. In Fig. 4.2(b), the three circles correspond to three patches. Each patch contains n nearest vertices, so there are $R = floor(N/n)$ patches, where $floor(a)$ stands for the integer that is closest to but smaller than a. The number of patches to be chosen is $r = ceiling(m_i/n)$ with $ceiling(a)$ as the smallest integer that is larger than a. Note that when patches are too close to each other, the linear problem of Eq. 6.2 becomes ill-conditioned. To seek a well-conditioned sub-matrix $\widetilde{\mathbf{G}_i}$, we randomly select r out of R patches for a predefined times and choose the r patches generating $\widetilde{\mathbf{G}_i}$ with the smallest condition number as desired sampling locations. The r chosen patches generate the indices recorded as S_i.

4.2.2.3 Localized Sampling

Localized sampling is the combination of completely random sampling and patch sampling. It takes random samples from one concentrated area. In Fig. 4.2(c), the area inside the dash line is a localized area for sampling. The key issue in localized sampling is to choose the "best" local area in terms of numerical stability, from which samples are obtained for reconstruction. Each local area is defined by a center vertex and its proximity size n, so there are N possible local areas overlapping with each other. The indices of vertices inside each local area are recorded as S_{loc}^q $(1 \leq q \leq N)$. This determines indices of rows in sub-matrix $\widetilde{\mathbf{G}}_i$. Usually, when the proximity size n is too small, the linear problem of Eq. 6.2 becomes ill-conditioned. Two factors - the location and the size n of the "best" local area - are determined interactively via the following process:

(1) The starting value for proximity size n is empirically set to some value. In our experiment, that value was chosen to be four times the maximum subspace dimension.

(2) For each n value, the tentative "best" local area $S_{loc}^{q^*}$ is chosen as the one leading to the smallest condition number among all possible sub-matrix $\widetilde{\mathbf{G}}_i$. If the number of vertices

N on the surface is too large, a random walk can be applied to try out a subset of all possible local areas, and choose the one with the smallest condition number as the desired sampling area.

(3) If the smallest condition number obtained from step (2) is still larger than a threshold, the proximity size n is increased.

(4) Repeat step (2) and step (3), until the proximity size n is large enough such that the condition number of the "best" local area is smaller than the threshold. Fig. 4.4 gives an example of how the condition number of sub-matrix $\widetilde{\mathbf{G}}_i$ changes as the proximity size n increases from 100 to 700.

(5) The index set of the "best" local area with determined proximity size n is applied as the desired sampling location S_i ($S_i = S_{loc}^{q^*}$) for the localized sampling strategy.

One interesting observation from our experiments is that the chosen "best" local area always corresponds to the area with the most deformations. Fig. 4.3 demonstrates the correlation between deformation levels and condition numbers in all possible local areas S_{loc}^q, using the gallbladder model. The left figure shows the color-coded rank of shape variations in each area S_{loc}^q, which is measured by first evaluating the coordinate variations at each vertex among the training surfaces and then obtaining the mean variation of vertices in area S_{loc}^q. The right figure shows the rank of the condition numbers for all corresponding sub-matrices $\widetilde{\mathbf{G}}_i$. The rank in the left picture is from the highest variation to the lowest variation, so the low ranked areas feature higher deformation levels. The rank in the right picture is from low to high, so the low ranked areas have lower condition numbers. The color distribution indicates that the area in contact with the instrument has the most deformation, which coincides with the "best" local area (lowest condition number) for sampling. This coincidence is in favor of the applicability of the proposed method, since the area observable from the imaging system during the surgery is exactly the area under operation.

Once S_i is determined, indices in S_i are applied as the desired sampling positions for subspace $\mathbf{G}_i$. In such a way, the overall sampling locations for all subspaces are determined as an index set $S = \bigcup_{i=1}^{J} \{S_i\}$. Samples taken for subspace $\mathbf{G}_i$ can be denoted as a vector

$\widetilde{\mathbf{h}}_{t,i} = [\mathbf{h}_t(s_{i,1}) \ \cdots \ \mathbf{h}_t(s_{i,m_i})]$. Then, the final sample vector can be written as

$$\widetilde{\mathbf{h}}_t = \bigcup_{i=1}^{J} \{\widetilde{\mathbf{h}}_{t,i}\} \tag{4.3}$$

where $\widetilde{\mathbf{h}}_t$ is of length $M \leq \sum_{i=1}^{J} m_i$. M is orders of magnitude smaller than the initial sample size N, which essentially allows for complete 3D surface reconstruction with low sampling density at low computational cost.

4.2.3 Deformation Reconstruction

The final step is to decide which subspace best represnts the deformation and then reconstruct the complete surface in that subspace with the limited samples taken from the designated locations. For J subspaces, there are J options to reconstruct the organ surface. Ideally, the optimal subspace (indexed by i^*) is selected by minimizing the overall reconstruction error (l_2 norm)

$$i^* = \min_{1 \leq i \leq J} (\|\vec{h}_t - \mathbf{G}_i \hat{\vec{c}}_{t,i}\|_2) \tag{4.4}$$

Since $\vec{h}_t$ is not known, it is infeasible to evaluate the overall accuracy. Intuitively, the reconstruction error at all known sampling positions S_i can be used for subspace selection,

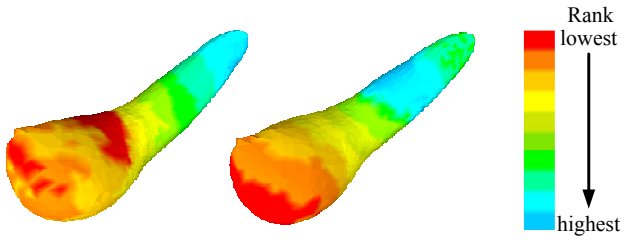

Figure 4.3: Color coded map of deformation levels: different color indicates different deformation levels.

so the objective function is modified as

$$i^* = \min_{1 \le i \le J} (\|\widetilde{\vec{h}}_{t,i} - \widetilde{\mathbf{G}}_i \hat{\vec{c}}_{t,i}\|_2) \tag{4.5}$$

However, Eq. 6.5 intends to minimize the reconstruction error only at S_i, without regulating the reconstruction beyond S_i. A different selection method is adopted. We devide S_i into two subsets $S_i = S_i^{'} \bigoplus S_i^{''}$, where $S_i^{'}$ is used to estimate $\hat{\vec{c}}_{t,i}$ in each subspace, and $S_i^{''}$ that carries reconstruction precision in the area beyond $S_i^{'}$ is applied to select the subspace. Therefore, the first step is to estimate the coefficients in each subspace as

$$\hat{\vec{c}}_{t,i} = (\widetilde{\mathbf{G}}_i^{'T} \widetilde{\mathbf{G}}_i^{'})^{-1} \widetilde{\mathbf{G}}_i^{'T} \widetilde{\mathbf{h}}_{t,i}^{'} (1 \le i \le J) \tag{4.6}$$

and then the subspace is selected according to

$$i^* = \min_{1 \le i \le J} (\|\widetilde{\vec{h}}_{t,i}^{''} - \widetilde{\mathbf{G}}_i^{''} \hat{\vec{c}}_{t,i}\|_2) \tag{4.7}$$

where $\widetilde{\mathbf{G}}_i^{'}$ and $\widetilde{\mathbf{h}}_{t,i}^{'}$ are the sub-matrix and surface samples corresponding to the indices in $S_i^{'}$, and $\widetilde{\mathbf{G}}_i^{''}$ and $\widetilde{\mathbf{h}}_{t,i}^{''}$ corresponding to $S_i^{''}$. Fig. 4.5 shows the reconstruction error in the sampling area (color-coded zone) using different subspaces. According to the error distribution, we can see that, in the sampling area, the reconstruction using the optimal subspace selected by the proposed method (left) has lower error than that using the suboptimal subspace

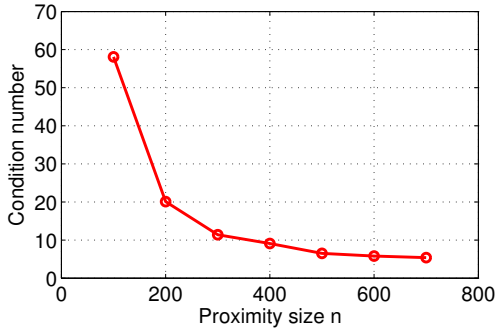

Figure 4.4: Condition number of sub-matrix $\widetilde{\mathbf{G}}_i$ with different proximity size n.

(right).

Once the subspace is selected, all samples indexed by S_{i^*} are used to estimate the coefficient vector $\hat{\vec{c}}_{t,i^*}$. Finally, the deformed surface is reconstructed as

$$\hat{\vec{h}}_t = \mathbf{G}_{i^*}\hat{\vec{c}}_{t,i^*} = \mathbf{G}_{i^*}[(\widetilde{\mathbf{G}}_{i^*}^T\widetilde{\mathbf{G}}_{i^*})^{-1}\widetilde{\mathbf{G}}_{i^*}^T\widetilde{\vec{h}}_{t,i^*}] \tag{4.8}$$

4.2.4 Interior Tracking

For an organ with both interior and exterior surfaces, the above theory can be adapted via the following extensions. First, a sparse surface representation is sought for each multiple-layer surface. Second, the sampling strategies in Section 4.2.2 are adjusted such that samples are taken only from the exterior for overall surface recovery.

4.2.4.1 Extended Sparse Surface Representation

We denote $\vec{x}_k^{\,in}$ and $\vec{x}_k^{\,ex}$ $(1 \le k \le K)$ as the interior and exterior surfaces of each training deformation. As described in the previous chapter, with the extended SRDS method, each training deformation can be sparsely represented with a coefficient vector $\widetilde{\vec{c}}_k$ as

$$\begin{bmatrix} \hat{\vec{x}}_k^{\,in} \\ \hat{\vec{x}}_k^{\,ex} \end{bmatrix} = \mathbf{G}_i\vec{c}_k = \mathbf{G}\widetilde{\vec{c}}_k \tag{4.9}$$

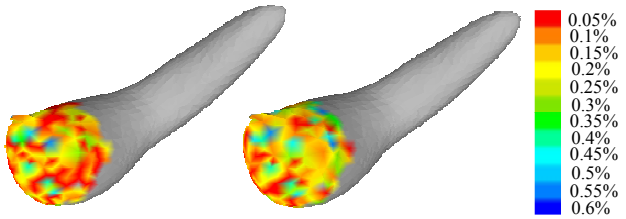

Figure 4.5: Reconstruction errors in the sampling area using different subspaces: (left) reconstruction with the optimal subspace; (right) reconstruction with the suboptimal subspace.

Similary, $\mathbf{G} = \bigcup_{i=1}^{J}\{\mathbf{G}_i\}$ is the desired structured dictionary and $\mathbf{G}_i$ is the subspace. $\widetilde{\vec{c}}_k$ has non-zero values only at the atoms corresponding to its representable subspace.

4.2.4.2 Sampling on the Exterior Surface

We denote $\vec{h}_t = \begin{bmatrix} \vec{h}_t^{in^T} & \vec{h}_t^{ex^T} \end{bmatrix}^T$ as the deformed surface to be reconstructed and subset $\widetilde{\vec{h}_{t,i}^{ex}}$ as the m_i samples to be chosen from the exterior for each subspace. Our underlying assumption is that the identified dictionary $\mathbf{G}$ is generalizable enough to cover the variation occurred in the testing population $\vec{h}_t$. Let $\widetilde{\mathbf{G}_i}$ stand for the sub-matrix containing m_i ($n_i < m_i \ll N_2$) rows of $\mathbf{G}_i$. Similar to the design in Sec. 4.2.2, we apply the "random walk" method to find an index set $S_i = \{s_{i,l} | 1 \leq i \leq m_i\}$ that forms a sub-matrix $\widetilde{\mathbf{G}_i}$ with the smallest condition number among all tries. Each atom $s_{i,l}$ is within $[N_1 + 1 \quad N_1 + N_2]$ on the exterior surface only. Consequently, the corresponding sample set is determined as $\widetilde{\vec{h}_{t,i}^{ex}} = [h_t(s_{i,1}) \ \cdots \ h_t(s_{i,m_i})]$, such that the over-determined linear system

$$\widetilde{\vec{h}_{t,i}^{ex}} = \widetilde{\mathbf{G}_i}\vec{c}_{t,i} \quad \text{for} \quad i = 1 \cdots J \tag{4.10}$$

can be well solved under LS constraints for coefficient vector $\vec{c}_{t,i}$ in each subspace $\mathbf{G}_i$. Then, the approach described in Sec. 4.2.3 can be applied to choose a subspace which yields the least reconstruction error at the known positions as the best-fit subspace for reconstructing the overall surface $\vec{h}_t$.

4.3 Approach

Based on the above theoretical design, we present a framework in this section to implement the proposed approach for real-time 3D visualization of organ deformations. As shown in Fig. 4.1, from the implementation perspective, problems that need to be solved include training/preoperative imaging, live surface sample retrieval with the 3D imaging device, and registration of images from different subjects and different modalities.

4.3.1 Training and Preoperative Imaging

To identify subspaces that capture the potential deformation features of the organ under consideration, a representative training set is required. Images from a number of resources can be applied for the training purpose, such as realistic 3D computer models that account for organ mechanical and physical properties, ex-vivo MRI or CT scans of organs under manual manipulation and in-vivo scans. Except with computer models which export 3D surfaces directly, organ segmentation is required for all imaging modalities, such as MRI or CT, to obtain 3D surfaces of the desired organ. The segmentation precision needs to meet the clinical requirement that anatomical features are correctly captured in the segmented results. In our experiments, the surfaces were manually segmented from the 3D MR scans using Mimics (Materialise) by trained users. We do not have golden standard to evaluate the exact segmentation precision. However, as provided by Ginneken *et al.* in [153], the average human segmentation error is $1.8mm$ in terms of RMS symmetric surface distance. According to our experiment results, this error is tolerable to achieve a reconstruction error below $5mm$.

If the patterns of organ deformations to be reconstructed can be predicted according to the surgical plan, such patterns can be mimicked during the generation of the training data. The resemblance between the training set and the testing set leads to higher reconstruction accuracy. If the deformation pattern cannot be estimated, random manipulation of the organ is statistically reasonable to obtain a representative training set. The training data is generally collected from different subjects.

For the organ to be tracked and visualized, a single preoperative MRI/CT scan of that organ needs to be acquired, used as an initial model for both subspace identification and registration between the preoperative modality and the real-time imaging device.

4.3.2 Sampling with Tracked Optical Sensors

An optical device equipped with structured light, laser or stereo cameras can be utilized to acquire 3D surface samples from the limited field of view, e.g. the laser-scan systems

developed in [154][155]. An example of 3D surgical device can use the ultra-thin and flexible scanning fiber endoscope of [156]. Note that the optical device needs to be tracked such that the real-time motion information can be used for image registration. Further, to meet the requirement of real-time visualization, the optical device needs to provide 3D coordinates of the accessible surface area corresponding to each deformation in real-time. Besides the acquisition speed, the precision of the optical device should be high enough to allow the identification of key anatomical features. To verify the feasibility of the proposed method, an ex-vivo experiment was conducted using a portable laser scanner from NextEngine which samples the organ surface from a restricted view. Details are provided in Sec. 4.4.

4.3.3 Registration

Surface registration is involved in both the training stage and the real-time visualization stage. During training, deformations taken at different time instants or from different subjects need to be aligned to achieve pointwise correspondence after eliminating the linear transformation. In the reconstruction phase, registration is conducted to align the coordinate system of the sampling device with that of the visualization space.

4.3.3.1 Training Surface Correspondence

Surface correspondence is to achieve vertex-wise matching over all training surfaces such that a common SH matrix $\mathbf{Y}$ can be applied during SHR. Fig.4.6 provides an example for illustration. The same colored vertices on deformation 1 and 2 indicate a matching pair.

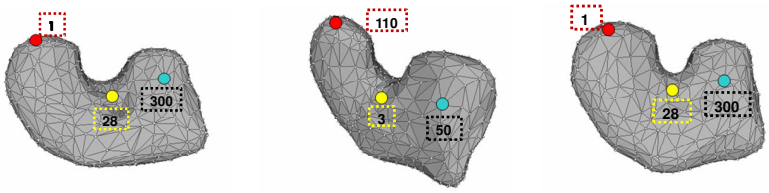

(a) (b) (c)

Figure 4.6: Surface correspondence: (a) vertex index on deformation 1, (b) vertex index on deformation 2 before correspondance, (c) corresponding vertex index on deformation 2

Initially, the ordering of vertices on deformation 1 (left) is independent of that on deformation 2 (middle). Once correspondence is achieved, vertices on deformation 2 (right) can be numbered in the same order as that for deformation 1. Different correspondence methods have been proposed, such as minimum description length [148][157] and SH coefficient alignment [150]. Each correspondence method must be evaluated as a function of the ultimate reconstruction accuracy that can be achieved with the proposed approach. Any correspondence method yields a reconstruction accuracy of less than the desired error is acceptable. In our work, we applied the SH based method for complicated surfaces and the proposed ray casting method for simpler surfaces to achieve surface correspondence. The procedure of surface correspondence starts with rigid registration followed by point-wise matching.

Rigid Registration

The rigid registration is to eliminate the difference across deformations due to rotation R_r and translation T_t. A coarse-to-fine registration procedure is applied, which starts with feature point based registration followed by refinement using Iterative Closest Point (ICP) method [149].

Let $P = \{\vec{p}_i\}_{i=1}^{N_p}$ and $Q = \{\vec{q}_i\}_{i=1}^{N_p}$ be the corresponding "matched" 3D feature points from two shapes to be registered, and N_p is no less than four in this chapter. Those feature points can be identified using method like scale invariant feature transform (SIFT) [152]. A coarse estimation of rotation R_r and translation T_t are achieved by minimizing the following objective function

$$f(R_r, T_t) = \frac{1}{N_p} \sum_{i=1}^{N_p} \parallel \vec{q}_i - R_r \vec{p}_i - T_t \parallel^2 \tag{4.11}$$

Point Correspondence with SH Coefficients

The second step for surface correspondence is performed in the harmonic domain to establish point-to-point matching across different deformations. The method based on the use of the first order ellipsoid achieves correspondence by rotating the parameterization, so that the spherical equator, 0° and 90° longitudes coincide with those of the first order ellipsoid.

Such a parametrization normalization step enables the corresponding surface points across different objects to share the same parameterization. This approach is efficient but works only if the first order ellipsoid is a real ellipsoid, not an ellipsoid of revolution or a sphere. In this chapter, we apply a more general method based on the minimum Root Mean Squared Distance (RMSD) [150].

Initially, the SH coefficient vector of each surface is obtained with a unique parametrization $\mathbf{Y}_k$, i.e., $\vec{x}_k = \mathbf{Y}_k \vec{f}_k^0$. Based on the underlying fact that two points with the same parameter pair when mapped to a sphere are considered to be a corresponding pair, we can fix parametrization of the template and rotate the other parametrization to obtain the surface correspondence. Mathematically, this is achieved by minimizing the RMSD between the SH coefficient vectors of the template $\vec{f}_t$ (with $f_{t,l}$ as elements) and that of the other surface $\vec{f}_k^0$ (with $f_{k,l}^0$ as elements). The RMSD is defined as

$$RMSD = \sqrt{\frac{1}{4\pi} \sum_{l=1}^{(L+1)^2} \|f_{t,l} - f_{k,l}^0\|^2} \tag{4.12}$$

The minimization is solved using the sampling-based strategy proposed in [150] and the result is a rotated vector $\vec{f}_k$ relative to $\vec{f}_k^0$. Consequently, each surface $\vec{x}_k$ can be approximately represented by $\vec{f}_k$ under the same parametrization generated according to the template surface.

Point Correspondence with Ray Casting

The ray-casting approach achieves correspondence by re-sampling the surfaces along the directions of rays which originate from the center of the sphere and end with a vertex on the sphere. Since the angular values of the re-sampled points along the same ray are constant, those re-sampled points correspond to the same points on the sphere. As a result, the re-sampled surfaces automatically possess the same parametrization. However, this method can only be applied to star-like surfaces which have a unique intersection between each ray and the crossing surface. For illustration, Fig.4.7(a) and Fig.4.7(b) depict two different cases of ray-surface intersection in the simplified 2D space. In Fig.4.7(a), there is

only one intersection point (p1 for ray $\overrightarrow{r_1}$ and p2 for ray $\overrightarrow{r_2}$) between each ray and surface S1. In contrast, Fig.4.7(b) gives an example where multiple intersections (p1, p1', p1" for ray $\overrightarrow{r_1}$ and p2 for ray $\overrightarrow{r_2}$) occur between rays and surface S2.

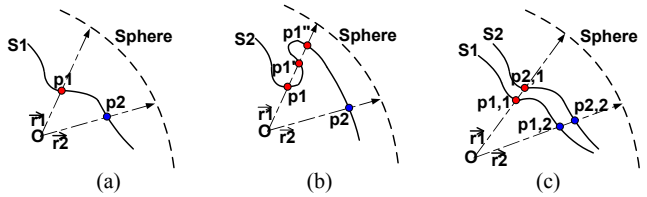

Figure 4.7: Point correspondence with ray casting:(a) unique ray-surface intersection, (b) multiple ray-surface intersections, (c) ray casting on two deformed surfaces

If the condition of single ray-surface intersection applies, deformations after rigid registration can be re-sampled through the following steps:

- Construct an icosahedron of W vertices with radius large enough to embrace the largest deformation volume in the training set; a larger W value results in denser samples to maintain the local details.

- Align the centers of the 3D surfaces to the origin of the icosahedron such that rays casting from the origin can always intersect with the surfaces.

- For each ray segment originating from the center and ending with a vertex on the icosahedron, find the triangle on the object surface mesh that intersects with the segment and use that intersection point as the new sample.

Fig.4.7(c) shows established sample pairs $(p_{1,1}, p_{2,1})$ and $(p_{1,2}, p_{2,2})$ over deformations S1 and S2. Each pair of points possess the same angular value and are mapped to the same point on the sphere. Therefore, as a byproduct, this re-sampling process also establishes an one-to-one mapping between a point on the object and a point on the sphere (icosahedron), which inherently meets the purpose of spherical parametrization. As a result, point-wise correspondence can be achieved across all re-sampled surfaces and a uniform harmonic matrix $\mathbf{Y}$ can be applied for SHR in the training stage. Fig.4.8(a) and Fig.4.8(b) show

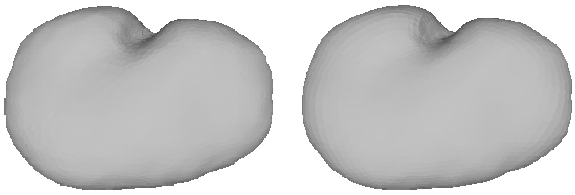

(a) (b)

Figure 4.8: Re-sampled surface with ray casting (a) original surface of kidney, (b) re-sampled surface of kidney

an original kidney surface and the corresponding re-sampled surface. We can see that the ray-casting procedure well maintains the original shape.

4.3.3.2 Multimodal Registration

Since the training and preoperative scans are in a coordinate system different from that of the optical device, the optical images have to be registered to the same coordinate system. The problem of accurately localizing instrumentation tips [42] is beyond the scope of this thesis, so we assume that the 3D optical device is equipped with tracked motion sensors which can provide geometric information to compensate for the linear transformation of the device relative to its initial position. In this thesis, we only consider a small scale transformation between the optical imagery and the training coordinate system during the real-time reconstruction stage after the initial registration.

The initial calibration is based on the registration of the preoperative MRI/CT model and the corresponding optical scan patch acquired when the organ is under the same deformation. The approach described previously of feature-point registration combined with ICP refinement can be applied directly for the calibration. Then the point correspondence can be computed by re-sampling the initial optical patch along the normal directions of vertices on the corresponding MRI surface.

During the real-time sampling and reconstruction phase, the new optical patch is first registered using the initial calibration metrics. Then fine tuning is conducted to compensate for the residual rotation and translation by applying the ICP method. Point correspondence is established via re-sampling the new optical patch along the normal directions of vertices

on the previously processed optical patch. This re-sampling strategy may not be the most efficient one. Other alternative correspondence method can also be applied.

4.4 Experiment

The feasibility of the proposed approach is verified using both FEM data and ex-vivo experiments. The test using the synthetic data is for theoretical verification in terms of reconstruction accuracy relative to the FEM generated model. The ex-vivo experiment on freshly excised porcine kidneys using a 3D MRI machine and a portable laser scanner is for evaluation in practical settings. The algorithm is implemented with MATLAB 7.11 running on a desktop with an Intel Xeon 2.13 GHz CPU and 9 GB memory.

4.4.1 Experiment with FEM Data

Three representative organs are considered in the FEM test: a complicated 3D cortical surface, a gallbladder with a geometrically simple surface, and a bladder consisting of both interior and exterior walls. Deformations of those organs were generated using simulation tools. The initial brain model was deformed with Simulation Open Framework Architecture (SOFA). This method uses multiple interacting geometrical models of the same object, including a mechanical model with mass and constitutive laws, a collision model with simple geometry, and a visual model with detailed geometry and rendering parameters. Gallbladder deformations were generated by a mass-spring surgical simulator [158]. This newly developed simulator incorporates the volumetric force to the mass-spring structure by introducing an equilibrium condition and taking into consideration force and momentum resultants. A bladder model was first imported into MAYA 8.0 (Autodesk, Inc.) for artifact smoothing, under the guidance of an urologist to minimize the numerical calculation error in the subsequent FE analysis. The smooth surface model of the bladder was then sent into ABAQUS 6.8 (ABAQUS, Inc.) and meshed into a FE model. An elasticity modulus of 0.05 MPa and a density of 1030 Kg/m3 were set in the FE model as the material properties of the bladder. Fig.4.9 gives two examples of shape distortions due to the endoscope poking

and grasping the gallbladder.

The parameters used in the tests on the three organs are listed in Table 4.1, including the number of vertices N, the maximum SH level L, the number of deformations for training K and reconstruction T_{rec}. The complicated brain structure requires more vertices and higher SH level for accurate surface representation.

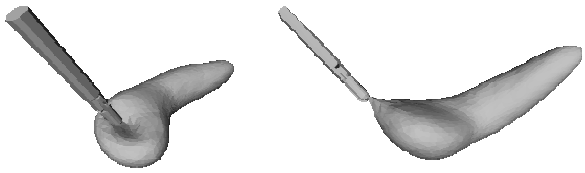

Figure 4.9: Surgical simulation of the gallbladder.

	N	L	K	T_{rec}
Brain	40962	80	35	30
GB	3038	25	250	114
Bladder	N1=4434, N2=4274	30	74	46

Table 4.1: FEM model setup

	Random	Patch	Local
Brain			
Sub. Dim.	13,6,3	13,6,3	13,6,3
Samples	28	3 (n=10)	32 (n=200)
EOF	1.41%	1.42%	1.44%
GB			
Sub. Dim.	57,56,42	57,56,42	57,56,42
Samples	117	5 (n=35)	140 (n=600)
EOF	0.31%	0.40%	0.41%
Bladder			
Sub. Dim.	35,37,35	35,37,35	35,37,35
Samples	90	160 (n=40)	100 (n=400)
EOF	0.102%	0.098%	0.111%

Table 4.2: Test results of brain, gallbladder and bladder models using three sampling methods.

4.4.1.1 Reconstruction Accuracy

The three different sampling strategies described in Sec. 4.2.2 were investigated on the three organs. To examine the reconstruction precision quantitatively, a parameter EOF defined

as the normalized Euclidean distance between the original surface x_n and the reconstructed surface $\hat{x}_n$

$$EOF = \| \hat{x}_n - x_n \|_2 \cdot (\| x_n \|_2)^{-1} \tag{4.13}$$

was applied in the tests. The corresponding surfaces generated by the FEM software were used as ground truth. Table 4.2 summarizes the test results. The three sampling methods are denoted as "Random", "Patch" and "Local", respectively, and "GB" stands for gallbladder.

Brain Deformations: Based on the 35 training deformations of the brain, subspaces on X, Y and Z axes were identified respectively. As shown in Table 4.2, there are 3 subspaces (spanned by 13 basic vectors) in X axis, 2 subspaces (spanned by 6 basic vectors) in Y axis and 1 subspace (spanned by 3 basic vectors) along Z axis. For the three sampling strategies, 28 samples in random sampling, 3 patches (10 samples in each patch) in patch sampling and 32 random samples from a local area (consisting of $n = 200$ vertices) were sufficient for reconstructing the complete brain deformations. The reconstruction accuracy for the three cases are 1.41%, 1.42% and 1.44%, relative to the original FEM surfaces.

Gallbladder Deformations: Relative to the extent of deformations involved in brain simulation, larger shape distortion is taken into consideration in the gallbladder test. After the training process, there are 2 subspaces (spanned by 49 basic vectors) in X axis, 2 subspaces (spanned by 44 basic vectors) in Y axis and 1 subspaces (spanned by 55 basic vectors) in Z axis. For the three different sampling strategies, 117 samples in random sampling, 5 patches (35 samples in each patch) in patch sampling and 140 random samples from a local area (consisting of $n = 600$ vertices) were used for reconstruction. The three sampling methods result in an average EOF of less than 0.41%.

Bladder Deformations: Reconstructing deformations of the interior and exterior walls of the bladder by taking samples from the exterior surface only was studied next. According to Table 4.2, the random sampling results in an EOF of 0.102% with 90 samples uniformly

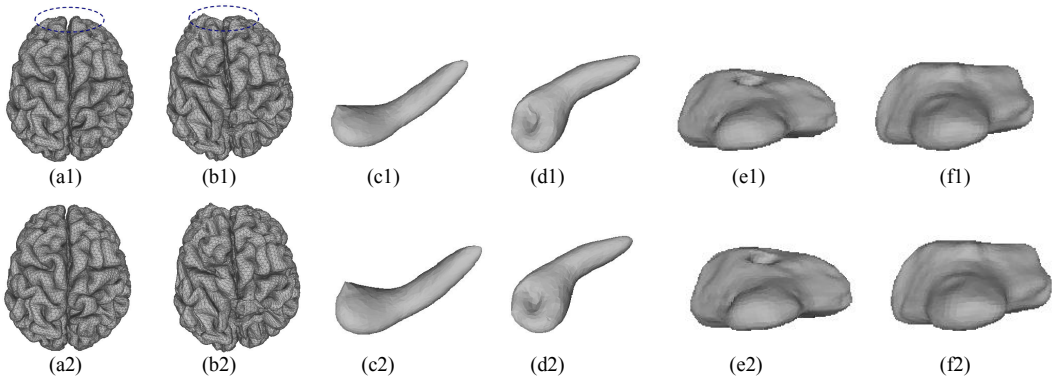

Figure 4.10: Comparison between the FEM generated surfaces (in the first row) and the reconstructed deformations using the proposed method (in the second row): (a&b) two brain deformation examples, (c&d) two gallbladder deformation examples, (e&f) interior and exterior of a bladder deformation example.

distributed on the exterior bladder surface. For patch sampling, four patches with size of 40 were required to achieve an accuracy of 0.098%. With localized sampling, only around 10% (400/4274) of the exterior bladder surface was under monitoring for reconstructing the overall shape at an EOF of 0.111%.

Fig. 4.10 compares the surfaces generated by the FEM software (first row) with the reconstructed surfaces using the proposed approach. Circles on the brains mark a typical deformation area. Sub-figure (e) and (f) corresponds to the interior and exterior surface of the bladder model. We can see that there is little observable difference between two sets of surfaces. Those test results on three different organs show that the accuracy achieved by the proposed method matches that of the complex FE modeling technique. The feasibility of reconstruction with samples retrieved from restricted areas demonstrates the applicability during the MIS operation when only limited access and field-of-view is available. Further, the proposed method potentially allows surgeons to see into the organ and observe the deformed structure on the interior wall, which certainly will lower the surgical risks in MIS.

4.4.2 Ex-vivo Experiment

To evaluate the proposed approach in practical settings, an ex-vivo experiment using freshly excised porcine kidneys was conducted at the Center for Interdisciplinary Applications in

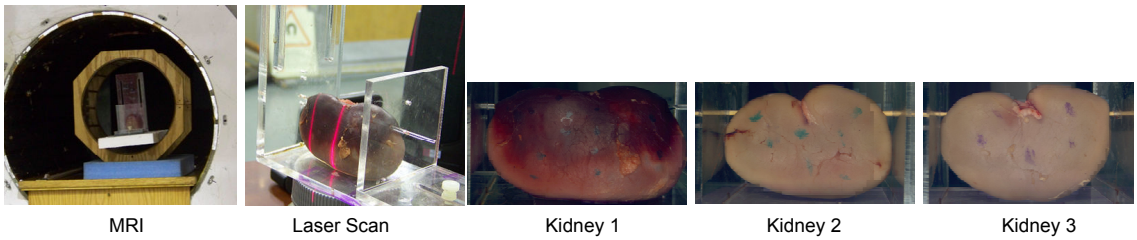

Figure 4.11: Experiment setup with MRI and laser scanner and three tested kidneys

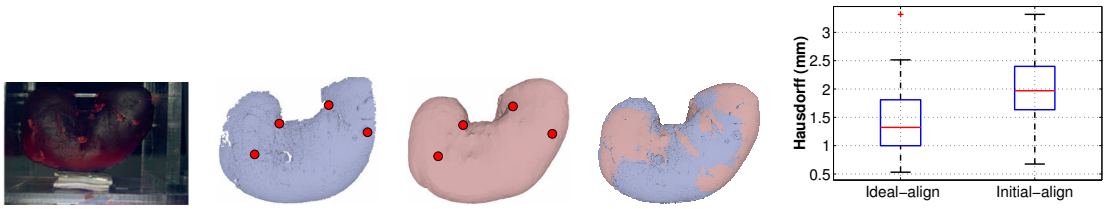

(a) (b) (c) (d) (e)

Figure 4.12: Registration of MRI model and optical image: (a) camera image, (b) optical patch, (c) MRI patch, (d) registered two patches, (e) boxplots of registration errors

Magnetic Resonance of University of Minnesota. A portable laser scanner with $0.13mm$ resolution was used to take live samples from a single side of the kidney.

The deformations imposed to the kidneys were generated in a random fashion with a non-magnetic device consisting of flexible components that can elongate or squeeze the organ at different locations. Each deformation was held still during the MRI and laser scanning as shown in Fig. 4.11. Each deformed kidney shape was scanned using a 3D MRI machine with isotropic spatial resolution of $1.2mm$ to serve as the training set or the ground truth for evaluating reconstruction precision. Samples retrieved with the laser scanner from a single-sided view or from even smaller patches of the deformed kidney were used for complete surface reconstruction. Fig. 4.11 shows the experimental setup, including the MRI machine, the laser scanner and three tested kidneys. The maximum SH degree L of the organ representation is 20, and each 3D MRI kidney mesh after surface correspondence has $N = 4002$ uniformly distributed vertices.

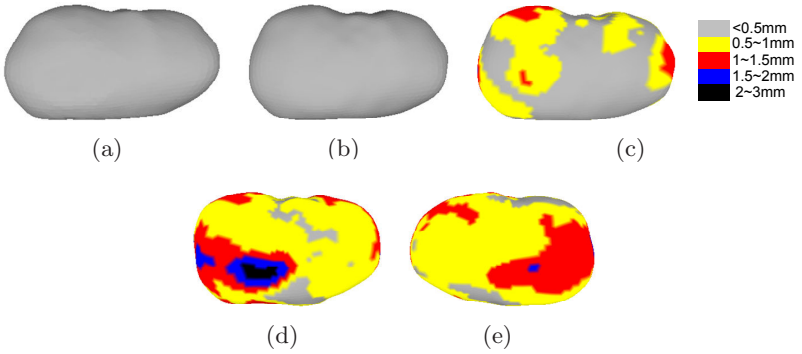

Figure 4.13: Intra-model test error: (a) MRI model as ground truth, (b) reconstructed surface on hidden side, (c) point errors between (a) and (b); (d) 90% reconstruction error on the hidden side, (e) 90% reconstruction error on the observable side.

4.4.2.1 Experimental Results

We first examine the registration error and then evaluate the reconstruction accuracy under two types of tests. In the intra-model test, both training and testing deformations were from the same kidney. The subsequent inter-model experiment utilized two out of the three kidneys plus a single MRI scan of the third kidney for training. The remaining deformations of the third kidney were used for testing the reconstruction accuracy. Three metrics are used for examining the reconstruction error: The EOF as a percentage measurement, the Hausdorff distance as a physical measurement of the maximum error and the RMS distance as an average distance error.

Registration Precision

The registration method described in Sec. 4.3.3.2 was applied to align the coordinate system of the real-time optical images and that of the initial MRI model. Registration under two different conditions was considered. The first is named as "ideal-align" in the following context. It registers each optical patch to the corresponding MRI deformation assuming that the ground truth is known. The second is labeled as "initial-align" which registers the optical patch to the MRI scan based on the preoperative MRI only using the proposed method. "Ideal-align" provides a lower bound to evaluate the registration accuracy of "initial-align" which is the practical solution.

Fig. 4.12(a) is the camera image of the single-sided view of the kidney seen by the laser

scanner, Fig. 4.12(b) is the corresponding 3D patch from the laser scanner, and Fig. 4.12(c) is the counterpart from MRI model. The highlighted feature points were used for the initial registration. Fig. 4.12(d) shows the superimposed view of two patches from different modalities after alignment. Over the three kidneys, the registration errors, evaluated as average Hausdorff distance between the MRI surfaces and the corresponding optical patches, are $2.1 \pm 0.64mm$ using "initial-align" as opposed to $1.4 \pm 0.67mm$ with "ideal-align", as shown in Fig. 4.12(e). The "initial-align" achieves good registration accuracy, but there is still room for improvement to further reduce the registration error.

Intra-model Testing

Kidney 1 was used for the intra-model experiment in which 26 randomly selected deformations were used for training and the remaining 5 were for the reconstruction test. Four types of measurements are evaluated, as shown in Table 4.3. The first measurement "Subspace Projection" is the accuracy of projecting deformations onto the structured dictionary. It examines the generalizability of training subspaces. The second measurement "MRI" is the reconstruction error when acquiring samples from MRI models directly within the restricted view seen by the laser scanner. It measures ideal reconstruction accuracy without any registration error. The third and fourth measurements, denoted as "ideal-align" and "initial-align", evaluate the reconstruction precision using optical samples using the aforementioned two different registration conditions.

	EOF(%)	Haus.(mm)	RMS(mm)
Sub. Proj.	0.65	0.69 ± 0.19	0.15 ± 0.03
MRI	1.31	1.47 ± 0.73	0.32 ± 0.08
Ideal-align	1.70	1.64 ± 0.59	0.42 ± 0.10
Initial-align	2.23	1.83 ± 0.56	0.51 ± 0.15

Table 4.3: Reconstruction accuracy in intra-model experiment

First, we observe that the low projection error (the first row) in Table 4.3 demonstrates the good generalizability of the identified subspaces to the deformations beyond the training set. This essentially enables the next accurate reconstruction using samples from the restricted field of view. Second, the reconstruction error under "initial-align" relying on

a single preoperative MRI scan is comparable to that under ideal registration. In terms of Hausdorff distance, there is only an average of $0.19mm$ degradation in "initial-align" compared to "ideal-align", and an average of $0.37mm$ difference from the "MRI" reconstruction. We believe that a better multi-modality registration approach can further bridge those gaps.

Fig. 4.13(a) and Fig. 4.13(b) are the MRI model and the corresponding reconstructed surface on the hidden side of the kidney. Fig. 4.13(c) is the color-coded error at each vertex on the unobserved side. For this particular reconstruction, the maximum error on the hidden side is below $1.5mm$. Fig. 4.13(d) and Fig. 4.13(e) show the 90% reconstruction errors on both sides, that is, 90% of all the tested intra-model deformations have point reconstruction errors no larger than the values shown in the figures. This is a near-worst measurement but it avoids bias due to potential outliers. We can see that errors on the hidden side (Fig. 4.13(d)) are slightly larger than that on the side exposed to the laser scanner (Fig. 4.13(e)).

Inter-model Testing

Two inter-model tests were conducted using the three kidneys. Test "Kidney 2" trained on Kidney 1 and 3 plus an initial frame of Kidney 2 and reconstructed the remaining deformations of Kidney 2; test "Kidney 3" trained on Kidney 1 and 2 plus an initial frame of Kidney 3 and reconstructed the remaining deformations of Kidney 3. The dimensions of the identified subspaces on X, Y and Z axes for these two inter-model tests are illustrated in Table. 4.4. We can see that the numbers J of subspaces required to reconstruct the kidney surfaces are small and the subspace dimensionalities are also low.

	J	X	Y	Z
Kidney 2	2 2 2	[39 48]	[41 45]	[40 47]
Kidney 3	3 2 2	[36 14 43]	[42 46]	[41 42]

Table 4.4: Subspace dimension in inter-model test

Consistent with the evaluations in the intra-model experiment, Table 4.5 and Table 4.6

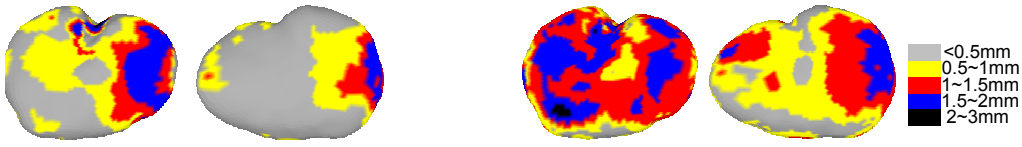

(a) (b)

Figure 4.14: Color coded reconstruction error for Kidney 2: (a) example reconstruction; (b) 90% reconstruction error field

list four types of errors for the two inter-model tests. First of all, the low projection errors demonstrate the feasibility of generalizing deformation variations based on different subjects. Further, the reconstruction accuracy with "initial-align" registration is relatively larger than that under the ideal condition. However, with "initial-align", the overall reconstruction error is always below $3mm$. Specifically, the Hausdorff distance in test Kidney 2 is $2.10 \pm 0.32mm$ with a maximum $2.88mm$, and $1.88 \pm 0.36mm$ with a maximum $2.51mm$ for Kidney 3. The corresponding RMS distance is below 1mm across all reconstructions. We find that the reconstruction error for Kidney 3 is slightly smaller than that of Kidney 2. In fact, the reconstruction error is mainly affected by two factors: (1) the generalizability of identified subspaces, indicated by "Subspace Projection" error in the table; and (2) the registration accuracy between the MRI and the optical imagery. The subspace projection error in the test of Kidney 3 ($0.66 \pm 0.17mm$, Hausdorff) is smaller than that for Kidney 2 ($0.89 \pm 0.06mm$, Hausdorff). This contributes to its higher reconstruction accuracy.

	EOF(%)	Haus.(mm)	RMS(mm)
Sub. Proj.	1.16	0.89 ± 0.06	0.13 ± 0.02
MRI	2.31	1.72 ± 0.37	0.45 ± 0.12
Ideal-align	2.70	2.23 ± 0.44	0.56 ± 0.11
Initial-align	3.92	2.10 ± 0.32	0.70 ± 0.07

Table 4.5: Results of inter-model experiment of Kidney 2

	EOF(%)	Haus.(mm)	RMS(mm)
Sub. Proj.	0.86	0.66 ± 0.17	0.10 ± 0.03
MRI	1.62	1.30 ± 0.45	0.29 ± 0.07
Ideal-align	2.22	1.44 ± 0.40	0.37 ± 0.07
Initial-align	2.74	1.88 ± 0.36	0.47 ± 0.05

Table 4.6: Results of inter-model experiment of Kidney 3

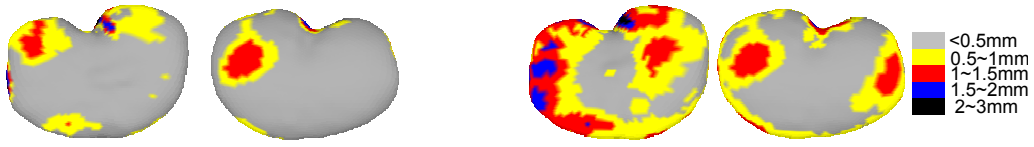

(a) (b)

Figure 4.15: Color coded reconstruction error for Kidney 3: (a) example reconstruction; (b) 90% reconstruction error field

Fig. 4.14(a) shows the color-coded error distribution of one example reconstruction of Kidney 2 for both the hidden and observed sides. Fig. 4.14(b) shows the 90% reconstruction errors. Both figures indicate that the errors on the hidden side (left) are relatively larger than those on the sampled side (right). Similar results are shown in Fig. 4.15(a) and Fig. 4.15(b) for reconstructing Kidney 3. Comparing Fig. 4.15(b) with Fig. 4.14(b) for the 90% reconstruction errors, we can see that better reconstruction precision is achieved in the test of Kidney 3.

According to the above results, we find that the error in the intra-model test is smaller than that in the inter-model experiments. This indicates that the inherent homology in the training and testing sets originating from the same object leads to better reconstruction accuracy. A good training set must be sufficiently large and representative of the organs that will be seen during the surgery. This also explains why the error evaluated in the FEM test is lower than that in the ex-vivo experiment in terms of EOF. The former has perfectly aligned training deformations from the same object. However, under the ex-vivo settings, noise caused by correspondence and registration errors between multiple modalities can lower the reconstruction accuracy. Further investigation will be dedicated towards the improvement of these factors.

Patch Sampling from Single-sided View In real laparoscopic surgery scenarios, due to the restricted and limited field of view or occlusion from other instruments, the visible surface patches could be smaller than the area of one side of the kidney, so the feasibility of using patch sampling from a single side of the kidney surface was also verified. The patch sampling strategy described in Sec. 4.2.2 was applied on the side of the kidney observable

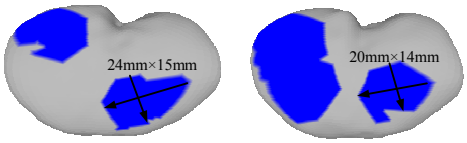

Figure 4.16: Selected patches restricted on one side of the kidney: (left) two patches, (right) three patches.

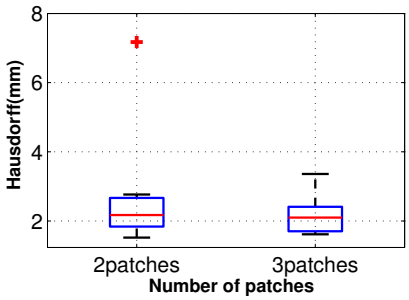

Figure 4.17: Reconstruction error as Hausdorff distance.

to the optical device. After determining the location of the desired patches, the laparoscope probes only need to focus on those particular zones, instead of the whole side area.

Fig. 4.16 illustrates two sampling cases using two patches (left) and three patches (right), corresponding to the scenarios when two or three laparoscope probes are available. In the right sub-figure, two of the three patches are connected so the boundary separating them is not observable. Each patch contains 170 samples, with the approximated physical size varying between $20mm \times 14mm$ and $24mm \times 15mm$. Fig. 4.17 shows the reconstruction accuracy in terms of the Hausdorff distance under the two cases. The average error with two patches is $2.67 \pm 1.74mm$, higher than $2.17 \pm 0.58mm$ - the error with three patches. In particular, with two patches, there is one outlier reconstruction leading to an error of $7.17mm$. Therefore, in general, with larger sampling patches or more sampling probes, the reconstruction of the deformations intends to be more robust.

Interior Structure Reconstruction

We also performed an experiment to track interior kidney features using data acquired on the exterior kidney surface only. Due to the resolution limitation of the ex-vivo experimental data, this test was conducted in the 2D space. Seventeen MRI image slices of Kidney 3 provided high enough resolution on the interior to allow consistent segmentation of the

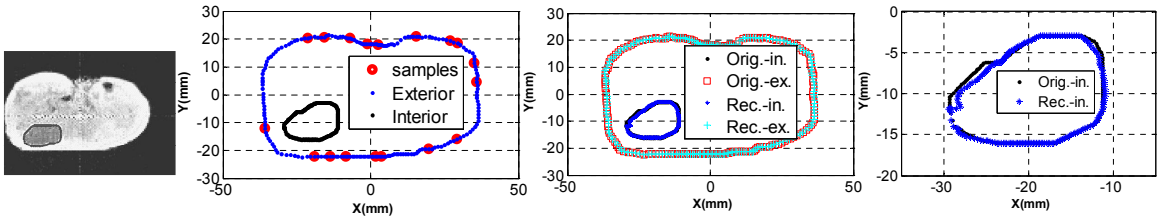

(a) (b) (c) (d)

Figure 4.18: Interior tracking: (a) original MRI image with highlighted area as interior feature, (b) segmented contour of the exterior (blue) and the interior feature (black), red dots are samples used for reconstruction, (c) reconstructed contour of interior (blue) and exterior (cyan) compared to ground truth of interior (black) and exterior (red), (d) enlarged view of reconstructed interior (blue) superimposed on the ground truth (black).

internal structures corresponding to different deformations. In each cross validation, 15 of the segmented contours were randomly selected as the training set and two remaining ones were used for the reconstruction test. The MRI scans were registered to identify the correspondence among contours.

Over the 20 cross validation tests that we performed as described above, the mean reconstruction error as Hausdorff distance for all interior contours is $1.33 \pm 0.20mm$ with a maximum of $1.77mm$ and RMS error of $0.32 \pm 0.06mm$. The maximum reconstruction error for the corresponding exterior contours is $1.39mm$ with a mean Hausdorff distance of $1.08 \pm 0.16mm$ and RMS error of $0.57 \pm 0.09mm$. Fig. 4.18 shows an example of reconstructed cross section. To the best of our knowledge, this is the first reported instance of a complete reconstruction of both the exterior and interior structures based on limited external samples only.

4.4.3 Computational Cost

The computational cost associated with surface reconstruction involves subspace selection (Eq. 4.6 and Eq. 4.7) followed by surface rendering (Eq. 4.8) in the selected subspace. The computationally intensive procedures including spherical harmonic representation, subspace identification, and random walk for sub-matrix determination are only used during the off-line training stage.

Since the dimensionality of $\widetilde{\mathbf{G}_i}$ is $m_i \times n_i$, the complexity of matrix inverse in Eq. 4.6

for all J subspaces is $O(J \times (n_i^3 + n_i^2 \times m_i))$. This computational cost is orders of magnitude lower than that involved in Eq. 5.2 during the training stage considering the massive size of $\mathbf{Y}$ ($n_i, m_i \ll N$ or $(L+1)^2$). The matrix multiplication in Eq. 4.8 leads to a complexity of $O(N \times n_i)$. Consequently, the total computational complexity in terms of multiplication is $O(N \times n_i + J \times (n_i^3 + n_i^2 \times m_i))$, with memory allocation of $O(J(N \times n_i + m_i \times n_i))$. Therefore, the overall complexity during reconstruction depends on the surface vertex number N, the subspace dimensions n_i, the sample number m_i and subspace number J, but is independent of the SH level L.

Table 4.7 summarizes the memory cost and reconstruction speed during the FEM experiment and the ex-vivo experiment using the proposed method, where "Intra_kidney" refers to the intra-model test on kidney 1, and "Inter_kidney2" and "Inter_kidney3" refer to the two inter-model tests, respectively. The interior structure reconstruction was conducted in the 2D space, so the cost is not included in the table. For consistent evaluations and fair comparisons, we applied the same randomly sampling strategy and set the number of samples used for reconstruction to be 150 for all the tests listed in Table 4.7. The reconstruction speed refers to the time used to actually reconstruct the surface, and does not include the laser scanning time. A 3D laparoscope system with high frame rates [155] should be used ideally.

In general, due to the low dimensionality of subspaces identified from the training data, our method results in low memory cost and achieves real-time reconstruction speed. Specifically, the maximum memory usage is below 5MB for all tests. The reconstruction speed is measured in *milliseconds* per surface reconstruction. The frame rate is the inverse of reconstruction speed, so it measures the number of surfaces reconstructed per second. As shown in Table 4.7, the frame rate varies between 10 frames/sec and 39 frames/sec, achieving real-time performance. We expect to further increase the frame rate after translating the implementation from MATLAB to *C*.

	Memory cost (MB)	Reconstruction speed(msec)	Frame rate (frames/sec)
Brain	3.6	33	30
GB	2.4	30	33
Bladder	4.3	104	10
Intra_kidney	1.4	28	35
Inter_kidney2	2.5	79	12
Inter_kidney3	2.5	77	13

Table 4.7: Computational cost of FEM test and ex-vivo experiment

4.4.4 *Error Propagation*

Table 4.8 and Table 4.9 show assessments of the error levels introduced by the main steps during the whole procedure. This provides insights into error propagation and guidance on how to further improve the accuracy of reconstructions. Measurement of each column in Table 4.8 (for test of Kidney 2) and Table 4.9 (for test of Kidney 3) from left to right are defined according to Fig. 4.19 as:

- $S1 - S0$: compare the represented surface after SHD with the surface segmented from MRI scans. This comparison captures the error introduced by SHD process;
- $S2 - S1$: compare the surface projected into the best-fit subspace with the SH represented surface. This comparison evaluates the generalizability of identified subspaces;
- $S3 - S2$: compare the reconstructed surface using sparse samples from the true MRI surface with that after subspace projection. This comparison measures the reconstruction accuracy if the tested surface lies in the selected subspace perfectly;
- $S3 - S0$: compare the reconstructed surface using sparse samples from the segmented MRI surface with the original MRI surface. This comparison evaluates the overall reconstruction error if the sparse samples are noise free;
- $S4 - S2$: compare the reconstructed surface using optical samples with that after subspace projection. This comparison is similar to $S3 - S2$ but uses samples from the optical device under the "initial-align" condition;

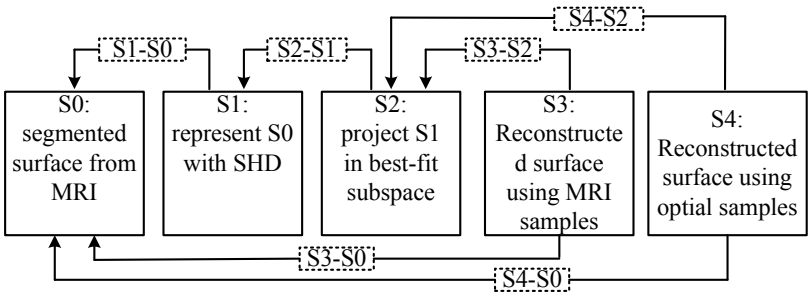

Figure 4.19: Evaluated step errors in reconstruction procedure.

- $S4 - S0$: compare the reconstructed surface using optical samples with the MRI surface. This comparison evaluates the overall reconstruction error with optical samples registered under the "initial-align" condition.

The error at each step is measured in terms of the maximum Hausdorff distance, average Hausdorff distance, maximum RMS distance and average RMS distance. We can see that the factors affecting the overall reconstruction precision include SHD accuracy, generalizability of the learned subspaces, reconstruction accuracy and signal quality of the samples from the optical device. Generally, the error at any step does not propagate linearly, e.g., $(S3-S0)^2 \neq (S1-S0)^2 + (S2-S1)^2 + (S3-S2)^2$. The largest error comes from the reconstruction step (shown as $S3 - S2$ and $S4 - S2$). The difference between columns of $S3 - S2$ (or $S3 - S0$) and $S4 - S2$ (or $S4 - S0$) indicates that the noise in optical samples due to the registration error relative to MRI scans leads to the lower reconstruction accuracy. We notice that, in Table 4.8, the maximum Hausdorff distance of step $S4 - S2$ is even larger than that of the overall error $S4-S0$, which is different from the trend observed in the other three measurements. Therefore, the averaged results are more representative of the overall performance than the worst-case measurement. Comparing the test on Kidney 2 (Table 4.8) with that on Kidney 3 (Table 4.9), we can see that the higher SHD accuracy ($S1 - S0$), better subspace generalizability ($S2 - S1$) and lower reconstruction error ($S3 - S2$) leads to higher overall precision in Kidney 3.

		$S1-S0$	$S2-S1$	$S3-S2$	$S3-S0$	$S4-S2$	$S4-S0$
Haus.(mm)	Max	0.63	1.01	1.94	2.48	2.61	2.56
Haus.(mm)	$Mean$ $\pm std$	0.40 ± 0.11	0.79 ± 0.12	1.46 ± 0.25	1.72 ± 0.37	1.94 ± 0.37	2.10 ± 0.32
RMS(mm)	Max	0.06	0.24	0.48	0.64	0.77	0.80
RMS(mm)	$Mean$ $\pm std$	0.06 ± 0.004	0.18 ± 0.04	0.36 ± 0.09	0.45 ± 0.12	0.61 ± 0.10	0.70 ± 0.07

Table 4.8: Breakdown of contributions to reconstruction error from major steps of the procedure for Kidney 2.

		$S1-S0$	$S2-S1$	$S3-S2$	$S3-S0$	$S4-S2$	$S4-S0$
Haus.(mm)	Max	0.25	0.86	1.57	1.94	2.45	2.51
Haus.(mm)	$Mean$ $\pm std$	0.20 ± 0.04	0.63 ± 0.16	1.07 ± 0.34	1.30 ± 0.45	1.44 ± 0.40	1.88 ± 0.36
RMS(mm)	Max	0.03	0.19	0.30	0.38	0.48	0.57
RMS(mm)	$Mean$ $\pm std$	0.02 ± 0.002	0.14 ± 0.03	0.23 ± 0.06	0.29 ± 0.07	0.42 ± 0.04	0.47 ± 0.05

Table 4.9: Breakdown of contributions to reconstruction error from major steps of the procedure for Kidney 3.

4.4.5 *Comparison with PCA*

The proposed method is also compared with the PCA approach [105] that intends to generalize the deformation with a single subspace spanned by the principle components of the variations in the training set. The random sampling strategy was applied to the ex-vivo kidney data in this comparison. Specifically, Kidney 1 and 2 plus an initial frame of Kidney 3 (51 deformations) were used as training data and the remaining deformations (19 deformations) of Kidney 3 were used for reconstruction testing.

Four different cases were evaluated: (1) PCA retaining all training components as a subspace, denoted by "PCA" in the chapter, (2) truncated PCA with reduced subspace dimensionality, denoted by "PCA-trun", (3) reconstruction using the proposed method with subspaces selected using sparse samples, denoted by "ISI-samp", (4) reconstruction using the proposed method under optimal subspace selection assuming known ground truth, denoted by "ISI-opt". The number of the most significant components retained in the truncated PCA was equal to the largest subspace size identified using the proposed method. The 4^{th} "ISI-opt" case provides an accuracy boundary that can be achieved only if the

proposed method always selects the optimal subspace (in the sense of least reconstruction error) using limited sparse samples. The sample number varied from 60 to 400 (out of 4002) during the test.

Fig. 4.21 shows the reconstruction errors in terms of the EOF and Hausdorff distance using different number of samples. The errors in the figure are average values across all the reconstructions. In general, the proposed subspace based method outperforms the PCA approach when the sample size is small and achieves similar accuracy when the sample size increases. Specifically, when the sample size is 60, the mean EOF error and mean Hausdorff distance are 2.85% and 3.0mm for "PCA", as opposed to 1.65% and 1.9mm for "ISI-samp" using our method. Meanwhile, the truncated PCA method lowers the EOF to 2.10% and the Hausdorff distance to 2.3mm but tends to have larger errors when the sample size increases due to reduced generalizability. As for "ISI-opt", the achievable reconstruction EOF and Hausdorff errors with a sample size of 60 are 1.57% and 1.5mm. This suggests that our method can be further improved with a better subspace selection strategy.

Fig. 4.22 shows the point error distribution in different ranges using 80 random samples. Errors below 1.25mm are not listed to avoid blurring the contrast among the four cases for errors above 1.25mm. We can see that in each error bracket, the counts for PCA based method are almost always larger than that for the ISI based approach. Quantitatively, in this reconstruction test, 14.4% of the surface points have errors larger than 1.25mm for "PCA", 10.5% for "PCA-trun", 8.62% for "ISI-samp" and 5.17% for "ISI-opt". Fig. 4.20 provides a direct visual comparison among the four cases. It shows the 90% errors from two different perspectives. Consistent with the previous numerical analysis, we can see that there are more errors above 1.5mm in the PCA method than while using the ISI based method. Specifically, in Fig. 4.20, the maximum error with PCA is 4.6mm as opposed to 3.0mm using "ISI-samp".

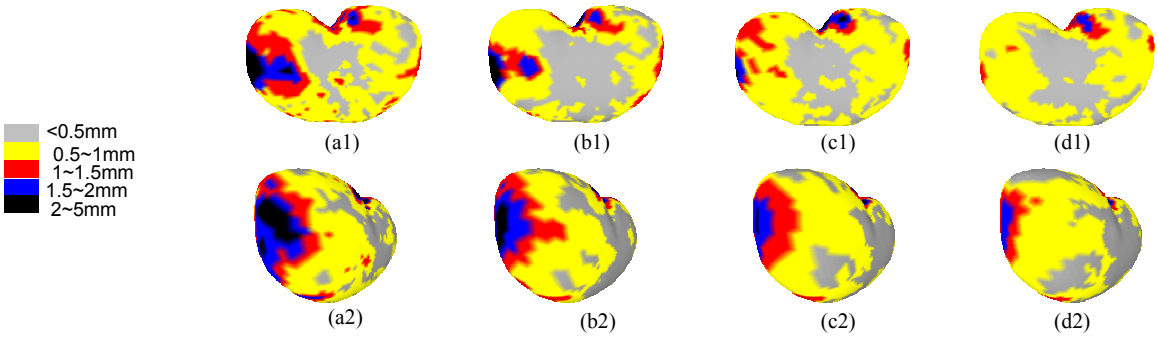

Figure 4.20: 90% reconstruction error field using 80 samples from two different perspectives: (a) PCA, (b) truncated PCA, (c) ISI with sub-optimal subspace selection, (d) ISI with optimal subspace selection.

4.5 Conclusion

This chapter presents a novel approach for real-time 3D visualization of organ deformations using a single preoperative MRI scan and optical patch imaging from a limited field of view. Evaluation with FEM data and ex-vivo experiments demonstrated that the design achieves real-time 3D reconstruction of organ deformations with spatial resolution better than $3mm$ in terms of the Hausdorff distance. This algorithm has the potential to reconstruct the interior structure of the organ by only sampling the exterior surface sparsely. This was demonstrated in the preliminary tests in the 2D space.

In our experiment, due to no accessibility to an appropriate medical devices, we used a low-end laser scanner with acquisition speed of about 1 minutes/scan, field of view of $9.7cm \times 12.9cm$ and resolution of $0.13mm$. For a typical 3D laser scan endoscope system as designed by Hayashibe, *et al.* [155], the frame rate is 5-6 frames per second, much higher than the speed of the portable laser scanner. As demonstrated in Sec. 4.4.3, our reconstruction algorithm can keep up with this scanning speed. The field of view and accuracy of the actual laparoscope system depends on the distance between the organ and the instrument. In laparoscopic surgery, the distance between the laparoscope and the object is usually $10 - 15cm$. In this range, using the system in [155], the maximum error is estimated to be $1.0 - 1.5mm$, and the scanned area can vary between $8cm^2$ and $20cm^2$. The typical size of the porcine kidney in our experiment is $94mm \times 46mm \times 36mm$, so the

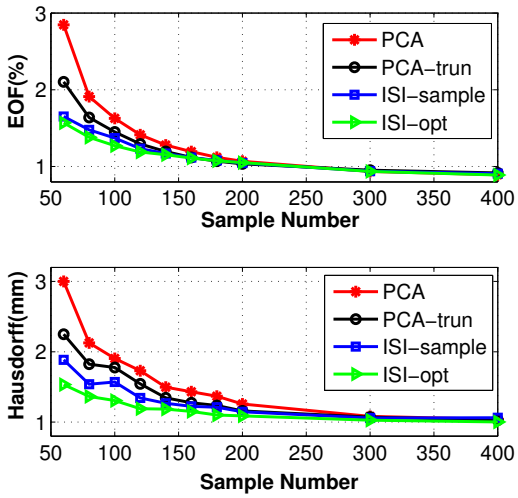

Figure 4.21: Reconstruction error as EOF and Hausdorff distance with different number of samples.

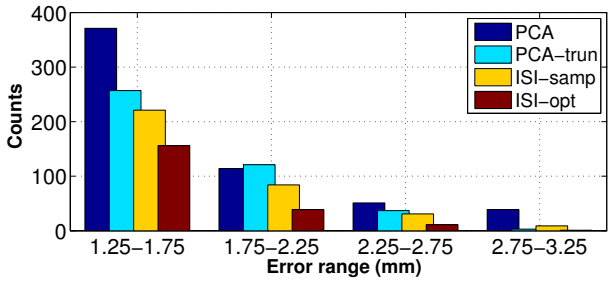

Figure 4.22: Point error distribution for reconstruction using 80 sparse samples.

view of the system in [155] can almost cover one side of the kidney. When the field of view from the single probe is small, e.g. $3cm^2$, two or three probes might be required to apply the patch sampling strategy for reconstruction. As shown in Sec. 4.4.2.1, by applying the patch sampling strategy on one side of the kidney using multiple probes, with patch size of $24mm \times 15mm$, it is still possible to reconstruct the complete surface.

Our proposed approach involves sparse surface representation and surface recovery from sparse samples. This bears similarities to compressed sensing [135] that seeks to acquire signals - known to have sparse representations in a domain - using a minimal number of measurements. However, compressed sensing theory requires that measurements are random linear combinations of all signal samples. In other words, the entire signal space must be

accessible although the number of acquired measurements is small. This is difficult to meet when only a part of the signal is within the acquisition range. Meanwhile, approaches for 3D scan completion or surface inpainting have been developed to fill small holes [139][136] existing in the scanned data. Example-based approaches can recover relatively large missing portion using patch warping and stitching [140] from an extensive 3D model library. These approaches still require the majority of surface information to be available. Besides, the warping and matching procedures are too computationally demanding to be implemented in real-time. In contrast, the proposed approach identifies a structured sparse representation of each 3D surface. This allows the procedure to reconstruct arbitrary organ deformations using very limited observed data with high accuracy.

Although only optical imaging was used in this thesis, other modalities used for MIS, such as X-ray and 3D ultrasound, can also be used to acquire the real-time surface samples. In general, the sampling device needs to have high accuracy. Ultrasound is an obvious candidate considering that it can provide samples on the hidden surface. Use of ultrasound may be hampered by gas insufflation during MIS. We have not conducted any experiment for 3D reconstruction by taking samples from ultrasound devices only. However, in Chapter 5, we will present an approach to improve 3D ultrasound image resolution based on a structured dictionary by fusing optical 3D image patches from a limited field of view and ultrasound images. The fusion process applies proper weights to account for resolution and noise differences between different modalities.

Chapter 5

Ultrasound Image Enhancement

5.1 Chapter Introduction

This chapter proposes a method that integrates the intraoperative ultrasound images with the optical imaging patches from a limited field of view to construct complete 3D organ surfaces in real-time with enhanced resolution as the organ deforms during the surgery. This method is another application of the SRDS theory introduced in the Chapter 3. In Chapter 4, we proposed an approach to reconstructing organ deformations including both interior and exterior surfaces using sparse samples from the limited field of view. Specifically, we presented three sampling strategies are designed to reconstruct the overall surface under different sampling conditions. Some practical issues, such as deformable surface registration, are also addressed. However, Chapter 4 does not consider reconstructions when data from different modalities are available. Furthermore, the subspace identification method used in our previous works assumes that all SH coefficients contribute equally to the reconstructed surface, which can lead to reduced generalization of the identified subspaces and lower accuracy in the reconstructed organ surfaces. Those limitations will be addressed in this chapter. The main contributions of the chapter include the following aspects.

1. We present a novel segmented training approach to improving the generalization of the identified subspaces to the potential deformations of the considered organ;

2. We propose an algorithm to enhance 3D ultrasound image resolution by fusing coarse ultrasound samples with fine optical scans obtained from the limited field of view of the organ surface;

3. Ex-vivo experimental results are demonstrated to verify that the algorithm can enhance the ultrasound image by revealing important surface details that are not visible on the original 3D ultrasound images on the surface area that is unobservable to the optical device.

This chapter is organized as follows. Section 6.2 describes the proposed algorithm of 3D ultrasound image enhancement. Section 6.3 presents some verification results of an ex-vivo experiment using ultrasound and optical devices. Finally, in Section 5.4, we finish the chapter with discussions and conclusions.

5.2 Algorithm

Fig. 5.1 outlines the framework of the proposed design for ultrasound image enhancement. The 3D high resolution endoscope observes the organ surface from a limited field of view while the 3D ultrasound is monitoring the surface simultaneously from a field of view larger than that of the endoscope. The trained subspaces in the structured dictionary are learned off-line from a representative set of training surfaces that can consist of images from different sources including MRI scans, CT scans and realistic computer models. The optical

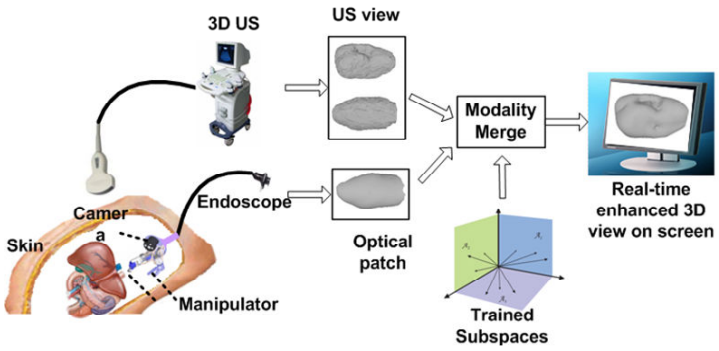

Figure 5.1: Outline of proposed ultrasound imaging enhancement method.

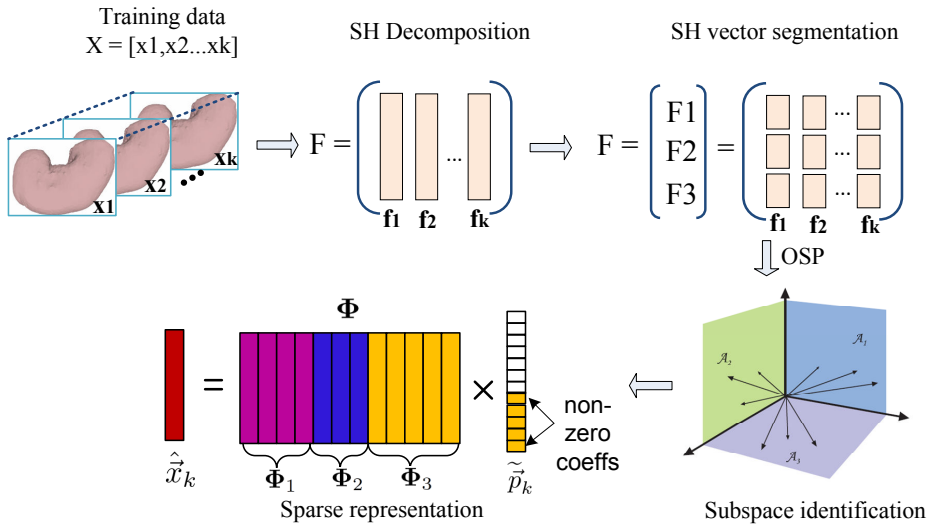

Figure 5.2: Procedures of the proposed segmented training method including SH decomposition, SH vector segmentation, subspace identification and sparse surface representation.

samples from the observable surface area together with the ultrasound samples on the area unseen by the optical device are merged under different weights to reconstruct the complete surface in the structured dictionary with resolution higher than the ultrasound image. The fusion algorithm accounts for differences in resolution and noise levels between the various modalities. The enhanced 3D visualization is displayed on a screen in real-time to assist the surgeons during MIS operations. The following subsections detail the design of the proposed approach, including three main steps: segmented training, multi-modal reconstruction and iterative correction.

5.2.1 Segmented Training

The training stage accomplishes the task of identifying low dimensional subspaces to form a structured dictionary in which deformations of the organ can be sparsely represented with high accuracy. Fig. 5.2 provides an overview of the training process. The training surfaces are first transformed into the harmonic domain via SH decomposition to decrease the dimensionality of training vectors and generate smoother surfaces with less noise and better homology. Then, each SH coefficient vector corresponding to each training surface is segmented into a number of subvectors according to the different significance levels. After

vector segmentation, subspaces are identified in each subvector set to form the deformation subspaces and the structured dictionary for sparse surface representation. Comparing to the training approach in [141][146], this new segmented training method is designed to improve the generalization of the subspaces learned from the limited training data. The following three steps illustrate the design details of the segmented training method.

5.2.1.1 Step1: SH Decomposition

Suppose that there are K training surfaces, and each surface $\vec{x}_k$ $(1 \leq k \leq K)$ consists of N vertices. With spherical parameterization [91][92], each $\vec{x}_k$ can be represented with SH as

$$\vec{x}_k = \mathbf{Y}\vec{f}_k \tag{5.1}$$

where $\mathbf{Y}$ of size $N \times (L+1)^2$ is the SH basis matrix with L as the maximum harmonic degree, and $\vec{f}_k$ with length $(L+1)^2$ is the coefficient vector. The linear system is approximately solved with Least Square (LS) constraints, so $\vec{f}_k$ is estimated as

$$\vec{f}_k = (\mathbf{Y}^T\mathbf{Y})^{-1}\mathbf{Y}^T\mathbf{x}_k \tag{5.2}$$

For the set of K deformed training surfaces $\mathbf{X}$, since the k^{th} surface is represented by $\vec{f}_k$ after SH decomposition, the group of training deformations can be described by a coefficient matrix $\mathbf{F}$

$$\mathbf{F} = \left| \begin{array}{cccc} \vec{f}_1 & \vec{f}_2 & \cdots & \vec{f}_K \end{array} \right|_{(L+1)^2 \times K} \tag{5.3}$$

in the transformed harmonic domain as

$$\begin{aligned} \mathbf{X} &= \left| \begin{array}{cccc} \mathbf{x}_1 & \mathbf{x}_2 & \cdots & \mathbf{x}_K \end{array} \right|_{N \times K} \\ &= \mathbf{YF} \end{aligned} \tag{5.3}$$

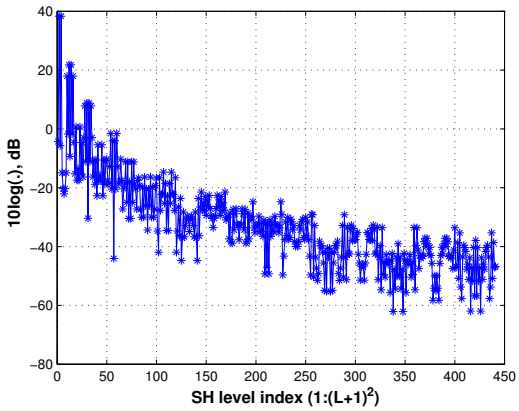

Figure 5.3: SH coefficient values as harmonic order increases.

5.2.1.2 Step2: Segmented Subspace Pursuit

Unlike the subspace pursuit method in [141][146] which does not differentiate the contribution of each SH component (each element in the vector $\vec{f_k}$) to the representation, we present here a new training method based on the observation that **the SH coefficients corresponding to the lower harmonic components are much more significant than those corresponding to the higher degree of harmonics. Therefore, the lower harmonic components play a more significant role in the accuracy of the final reconstructed surface.** Fig 5.3 demonstrates the significance levels of the coefficient values on a logarithmic scale. Based on this fact, our new method is to increase the precision at those significant components during subspace pursuit and thus obtain more precise surface representations in the structured dictionary. The details of the segmented subspace pursuit process is described as follows.

First, each $\vec{f_k}$ is segmented into a number of subvectors according to the significance of each harmonic coefficient. The mean of all the training SH coefficient vectors is obtained as

$$\overline{\vec{f}} = \frac{1}{K}\sum_{i=k}^{K}\vec{f_k} \tag{5.4}$$

where vector $\overline{\vec{f}}$ consists of elements $\overline{f}_i$ with $1 \leq i \leq (L+1)^2$. $\{\overline{f}_i\}_{i=1}^{(L+1)^2}$ is sorted out in

a descending order and the ordering indices are recorded as set $\{g_i\}_{i=1}^{(L+1)^2}$. Then both the harmonics (columns) in $\mathbf{Y}$ and elements in each $\vec{f}_k$ are re-ordered according to the index sequence in $\{g_i\}_{i=1}^{(L+1)^2}$. To avoid involving too many symbols, we still use $\mathbf{Y}$ for SH basis matrix and $\vec{f}_k$ for SH coefficient vectors even after this re-ordering process.

With element rearrangement based on the average SH vector $\overline{\vec{f}}$, subvectors are generated by partitioning $\vec{f}_k$. Without loss of generality, an example of dividing $\vec{f}_k$ into three subvectors is used for illustration. In this case, $\vec{f}_k$ is divided as $\vec{f}_k = \begin{bmatrix} \vec{f}_{k,1}^T & \vec{f}_{k,2}^T & \vec{f}_{k,3}^T \end{bmatrix}^T$, where $\vec{f}_{k,i}$ $(i = 1, 2, 3)$ are the three subvectors, each comprises α_i coefficients at the corresponding harmonic degrees, and T means matrix transpose. The first subvector contains the most significant coefficients followed by the second subvector with less significance, and the third subvector consists of the remaining ones. The size α_1 and α_2 depend on the number of training data K, and $\alpha_1 + \alpha_2 + \alpha_3 = (L+1)^2$ applies. For instance, with $K = 45$, $(L+1)^2 = 441$, $\vec{f}_k = [f_{k,1} f_{k,2} ... f_{k,441}]^T$, we can set $\alpha_1 = \alpha_2 = 50$ and $\alpha_3 = 341$, such that

$$\begin{aligned} \vec{f}_{k,1} &= [f_{k,1}\ f_{k,2}\ \cdots\ f_{k,50}]^T \\ \vec{f}_{k,2} &= [f_{k,51}\ f_{k,52}\ \cdots\ f_{k,100}]^T \\ \vec{f}_{k,3} &= [f_{k,101}\ f_{k,102}\ \cdots\ f_{k,441}]^T \end{aligned}$$

In this example, the size α_i is set as 50 in the first two training subvectors, slightly larger than $K = 45$. Our experiments show that if the subvector size $\alpha_i (i = 1, 2)$ is equal to K, the matrices that arise during surface reconstruction using samples from a limited field of view tend to have large condition numbers. Therefore subvector size α_i is usually set larger than training surface number K to achieve numerical stability. With the fragmentation of $\vec{f}_k$, the SH description matrix F of training surfaces is accordingly divided into three subvector sets as $F = \begin{bmatrix} F_1^T & F_2^T & F_3^T \end{bmatrix}^T$ with $F_i = [\vec{f}_{1,i}\ \vec{f}_{2,i}\ ...\ \vec{f}_{K,i}]$ $(i = 1, 2, 3)$ containing the corresponding subvectors.

The OSP method [121] is applied to each training subvector set F_i. The identified subspaces in each set are denoted as $\{\mathbf{U}_i^{\omega_i}\}_{1 \le i \le 3}^{1 \le \omega_i \le J_i}$, where J_i is the number of subspaces

learned from F_i. Consequently, each subvector $\vec{f}_{k,i}$ can be represented in the chosen subspace with a low dimensional vector $\vec{p}_{k,i}$ as

$$\hat{\vec{f}}_{k,i} = \mathbf{U}_i^{\omega_i} \vec{p}_{k,i} \tag{5.2}$$

By concatenating $\vec{p}_{k,i}$ resulted from each subvector to form $\vec{p}_k = \begin{bmatrix} \vec{p}_{k,1}^T & \vec{p}_{k,2}^T & \vec{p}_{k,3}^T \end{bmatrix}^T$, the original SH coefficient vector $\vec{f}_k$ is represented as

$$\hat{\vec{f}}_k = \begin{bmatrix} \mathbf{U}_1^{\omega_1} & 0 & 0 \\ 0 & \mathbf{U}_2^{\omega_2} & 0 \\ 0 & 0 & \mathbf{U}_3^{\omega_3} \end{bmatrix} \vec{p}_k \tag{5.3}$$

where $1 \leq \omega_1 \leq J_1$, $1 \leq \omega_2 \leq J_2$ and $1 \leq \omega_3 \leq J_3$.

5.2.1.3 Step3: Efficient Surface Representation

Based on the above procedures of SH decomposition (Eq. 6.1) and subspace pursuit (Eq. 5.3) in the transformed harmonic domain, each training deformation is approximately represented in the original spatial domain as:

$$\begin{aligned} \hat{\vec{x}}_k &= \begin{bmatrix} \mathbf{Y_1} & \mathbf{Y_2} & \mathbf{Y_3} \end{bmatrix} \begin{bmatrix} \mathbf{U}_1^{\omega_1} & 0 & 0 \\ 0 & \mathbf{U}_2^{\omega_2} & 0 \\ 0 & 0 & \mathbf{U}_3^{\omega_3} \end{bmatrix} \vec{p}_k \\ &= \begin{bmatrix} \mathbf{Y_1}\mathbf{U}_1^{\omega_1} & \mathbf{Y_2}\mathbf{U}_2^{\omega_2} & \mathbf{Y_3}\mathbf{U}_3^{\omega_3} \end{bmatrix} \vec{p}_k \end{aligned} \tag{5.3}$$

where $\mathbf{Y_i}$ consists of harmonics corresponding to the components included in subvector $\vec{f}_{k,i}$, that is, in this three subvector example $\mathbf{Y_1}$ and $\mathbf{Y_2}$ contain the first and second 50 columns of $\mathbf{Y}$ (after re-ordering), and $\mathbf{Y_3}$ contains the remaining columns. Finally, the

desired deformation subspaces are formed as

$$\mathbf{\Phi}_\eta = \left[\begin{array}{ccc} \mathbf{Y_1}\mathbf{U}_1^{\omega_1} & \mathbf{Y_2}\mathbf{U}_2^{\omega_2} & \mathbf{Y_3}\mathbf{U}_3^{\omega_3} \end{array} \right] \tag{5.4}$$

where $1 \leq \eta \leq J$ and $J = J_1 \times J_2 \times J_3$ is the total number of subspaces. The subspace dimension of each $\mathbf{\Phi}_\eta$ is $N \times \mu_\eta$. Consequently, the structured dictionary is constructed via concatenation as $\mathbf{\Phi} = \bigcup_{\eta=1}^{J}\{\mathbf{\Phi}_\eta\}$, and each deformation can be sparsely represented in the dictionary as

$$\hat{\vec{x}}_k = \mathbf{\Phi}_\eta \vec{p}_k = \mathbf{\Phi}\widetilde{\vec{p}}_k \tag{5.5}$$

where $\widetilde{\vec{p}}_k$ is a block sparse vector with non-zero values only at the positions corresponding to the chosen subspace for representation. As shown in the second row of Fig. 5.2 where the sparse representation involves a dictionary consisting of three subspaces. In this example, $\vec{x}_k$ lies in subspace $\mathbf{\Phi}_3$ which is spanned by 8^{th} to 12^{th} columns in $\mathbf{\Phi}$, then $\widetilde{\vec{p}}_k$ has nonzero values only at the positions indexed by [8 12].

It is worth noting that, according to Eq. 5.4, the dimension of $\mathbf{\Phi}_\eta$ depends on the number of subvectors into which $\vec{f}_k$ is segmented and the subspace size identified in each subvector set. Meanwhile, the total number of deformation subspaces J is determined by the number of identified subspaces in each subvector set. Empirically, larger number of subvectors and subspaces tends to improve the generalization of the structured dictionary in terms of higher deformation representation accuracy in $\mathbf{\Phi}$. However, as shown in Section 5.2.2, the dimension of each $\mathbf{\Phi}_\eta$ and the number of subspaces J both affect the computational complexity of the reconstruction procedure. Therefore, there is a tradeoff between good dictionary generalization (high reconstruction accuracy) and the efficiency of surface reconstruction.

5.2.2 Multi-modal Reconstruction

The second stage is to reconstruct the overall surface based on the structured dictionary $\mathbf{\Phi}$, utilizing fine samples obtained with the high resolution imaging modality (e.g. optical

device) from the limited field of view and coarse samples obtained with the ultrasound device from the hidden area observable to the ultrasound only. Those samples are fused under proper weights considering the different resolution and noise levels of different modalities. The surface reconstructed in the corresponding best-fit subspace has higher resolution compared to the original ultrasound image, not only on the area observable to the optical device but on the side beyond the view of the optical device.

Without loss of generality, we consider an example case involving two imaging modalities for illustration. The approach can be generalized straightforwardly to the applications involving more than two modalities. Surface samples are denoted by $\vec{x}^I = [x_1^I \ x_2^I \ ... \ x_N^I]^T$ with $I = a, b$ differentiating the two modalities. Since samples only from restricted area are available, the sample indices corresponding to the accessible field of view for different modalities are recorded as $S^I = \{s_j^I \mid 1 \leq j \leq m^I, s_j^I \in [N_1^I \ \ N_2^I]\}$, where m^I ($\mu_\eta < m^I \leq N$, for any η) is the number of available samples from the limited sampling area which is defined by $[N_1^I \ \ N_2^I]$ with $0 \leq N_1^I \leq N_2^I \leq N$. Therefore, the actual retrievable samples of the partial surface are formed as $\tilde{\vec{x}}^I = [x_{s_1^I}^I \ x_{s_2^I}^I \ ... \ x_{s_{m^I}^I}^I]^T$ for $I = a, b$.

In order to reconstruct the surface in the best-fit subspace, the first step is to estimate the coefficient vector in each subspace. This is achieved by solving the joint over-determined linear system defined in the two modalities for $\vec{p}_\eta$

$$\tilde{\vec{x}}^a = \tilde{\mathbf{\Phi}}_\eta^a \vec{p}_\eta \ \text{ and } \ \tilde{\vec{x}}^b = \tilde{\mathbf{\Phi}}_\eta^b \vec{p}_\eta \tag{5.6}$$

where submatrix $\tilde{\mathbf{\Phi}}_\eta^I$ ($I = a, b$) comprises the rows from $\mathbf{\Phi}_\eta$ corresponding to the sample indices in S^I. To solve the set of linear equations, we define the cost function $\mathbf{\Delta}$ to be minimized over $\vec{p}_\eta$ as

$$\mathbf{\Delta} = \sum_{i=1}^{m^a} \frac{\|(x_{s_i^a}^a - \Phi_\eta^{a,i} \vec{p}_\eta)\|^2}{(\sigma_i^a)^2} + \sum_{j=1}^{m^b} \frac{\|(x_{s_j^b}^b - \Phi_\eta^{b,j} \vec{p}_\eta)\|^2}{(\sigma_j^b)^2} \tag{5.7}$$

where $(\sigma_i^I)^2 (I = a, b)$ is the variance of the errors at the corresponding vertex for each

modality, accounting for differences in resolution and noise levels of samples from the two different image resources. $\Phi_\eta^{a,i}$ (or $\Phi_\eta^{b,j}$) is the i^{th} (or j^{th}) row of $\tilde{\mathbf{\Phi}}_\eta^a$ (or $\tilde{\mathbf{\Phi}}_\eta^b$). Generally, the variance $(\sigma_i^I)^2$ can be learned from the training data set. In this chapter, we use the optical scans ($I = a$) as the ground truth, so the corresponding error variance is set as $(\sigma_i^a)^2 = 1$ for all $i = 1,\ ...,\ m^a$. The contribution of each ultrasound sample is inversely weighted by $(\sigma_j^b)^2$ ($j = 1,\ ...\ m^b$) that can be estimated as the average registration error between the training ultrasound surfaces and the corresponding optical scans at each vertex. Therefore, by setting the first derivative of cost function $\mathbf{\Delta}$ as zero, the coefficient vector $\vec{p}_\eta$ can be estimated as

$$\hat{\vec{p}}_\eta = \left(\sum_{i=1}^{m^a} \frac{\Phi_\eta^{a,i^T} \Phi_\eta^{a,i}}{(\sigma_i^a)^2} + \sum_{j=1}^{m^b} \frac{\Phi_\eta^{b,j^T} \Phi_\eta^{b,j}}{(\sigma_j^b)^2} \right)^\dagger * \left(\sum_{i=1}^{m^a} \frac{\Phi_\eta^{a,i} x^a_{s_i^a}}{(\sigma_i^a)^2} + \sum_{j=1}^{m^b} \frac{\Phi_\eta^{b,j} x^b_{s_j^b}}{(\sigma_j^b)^2} \right) \tag{5.7}$$

where $A^\dagger$ is the pseudo inverse of matrix A. In the above deduction, all retrievable samples from different modalities are utilized for fusion and reconstruction. In practice, as demonstrated in the next experiment section, if the empirical error variances estimated from the training data at certain locations are too large (above a predefined level), the corresponding samples are excluded from the sample set, which can effectively prevent the reconstruction from being polluted by those extremely noisy samples.

Once the coefficient vector in each subspace is obtained, the next step is to decide which subspace the current deformation best fits in and then reconstruct the entire surface in the selected subspace. Among the J deformation subspaces, we choose the subspace which leads to the least reconstruction error at the known locations observable to the high resolution modality as the best-fit subspace. Mathematically, the best subspace indexed by $\eta^\star$ is determined according to

$$\eta^\star = \min_{1 \le \eta \le J} (\|\tilde{\vec{x}}^a - \tilde{\mathbf{\Phi}}_\eta^a \hat{\vec{p}}_\eta\|_2) \tag{5.8}$$

where $I = a$ corresponds to the optical imagery. Then the overall surface can be reconstructed as

$$\hat{\vec{x}} = \mathbf{\Phi}_{\eta^\star} \hat{\vec{p}}_{\eta^\star}. \tag{5.9}$$

5.2.3 Iterative Correction

An iterative correction process is conducted to further increase the reconstruction precision based on the structured dictionary. The underlying principle is similar to the rules of image denoising relying on a trained dictionary. After training, we know that any deformation of the considered organ lies in one of the identified subspaces $\mathbf{\Phi}_\eta$ in dictionary $\mathbf{\Phi}$. Therefore, by projecting the progressively corrected reconstruction into the subspace, it is expected to bring the new reconstruction closer to the ground truth. This iterative correction concept is illustrated by Fig. 5.4 in the 2D space. The red line is the ground truth and the n^{th} iteration leads to the reconstruction (blue curve). Before the next iteration, the reconstruction from n^{th} iteration is partially updated by replacing the samples with true values at the locations where the ground truth is known. The updated result is noted in black in Fig. 5.4, with the lower straight line section partially coincident with the red line and the upper curving part coincident with the blue line. This updated signal (black curve) is further projected in the selected subspace during the $(n+1)^{th}$ iteration to obtain an improved signal shown

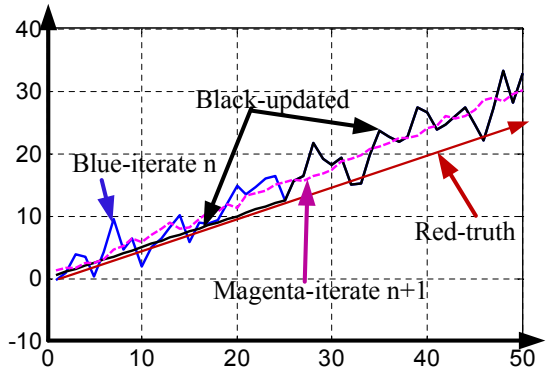

Figure 5.4: Illustration of iterative correction in 2D.

in magenta.

Based on the above concept, in the case of 3D surface reconstruction using ultrasound and optical devices, for each iteration, the current reconstructed surface is updated by replacing the vertices at the locations observable to the optical scanner with those optical coordinates as true values. This new surface with partial exact samples and partial estimated samples is then re-projected to the chosen subspace to obtain a new reconstruction. This iterative procedure stops either when the maximum allowed iteration times N_{iter} is reached or the precision enhancement speed at those known optical locations is below a predefined threshold ρ. The following steps generalize the iterative correction process, where modality indexed by $I = a$ corresponds to the optical imagery.

- Initialization when $n = 1$

  - initial reconstruction $\hat{\vec{x}}_n = \mathbf{\Phi}_{\eta^\star} \hat{\vec{p}}_{\eta^\star}$;

  - initial error at known locations

  $\tau_n = RMS(\hat{\vec{x}}_{n,S^a}, \tilde{\vec{x}}^a)$, $\tau_{n-1} = 0$;

- While $(n < N_{iter})$ & $(\tau_n - \tau_{n-1} > \rho)$

  - save current reconstruction $\hat{\vec{x}}_{n-1} = \hat{\vec{x}}_n$;

  - update current reconstruction with known true values:

  $$\hat{\vec{x}}^{up}_{n-1} = \left\{ \begin{array}{cc} \hat{x}_{n-1,j} & j \notin S^a \\ \tilde{\vec{x}}^a & j \in S^a \end{array} \right\}$$

  - save current error $\tau_{n-1} = \tau_n$

  - re-project the updated reconstruction:

  $\hat{\vec{x}}_n = Pro(\hat{\vec{x}}^{up}_{n-1}, \mathbf{\Phi}_{\eta^\star})$

  - calculate new error $\tau_n = RMS(\hat{\vec{x}}_{n,S^a}, \tilde{\vec{x}}^a)$

  - $n = n + 1$

where $\hat{\vec{x}}_{n,S^a}$ are the reconstructed surface samples at the locations indexed by S^a, $\tau_n = RMS(\hat{\vec{x}}_{n,S^a}, \tilde{\vec{x}}^a)$ is the root mean square distance between the true optical samples $\tilde{\vec{x}}^a$ and the corresponding points on the reconstructed surface during n^{th} iteration, and $Pro(\hat{\vec{x}}^{up}_n, \mathbf{\Phi}_{\eta^\star})$ is the operation of projecting updated surface $\hat{\vec{x}}^{up}_n$ in subspace $\mathbf{\Phi}_{\eta^\star}$.

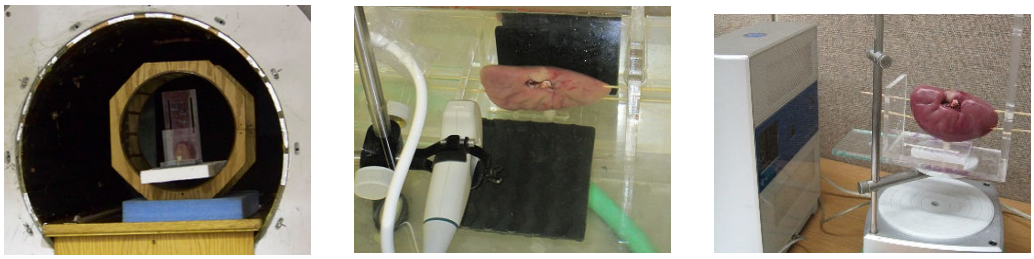

(a) (b) (c)

Figure 5.5: Experiment setup: (a) MRI, (b) ultrasound, (c) optical (laser) scanner

5.3 Evaluation

To verify the feasibility of the proposed approach, an ex-vivo experiment on freshly excised porcine kidneys was conducted using a 3D MRI machine, a 3D ultrasound apparatus (Ultrasonix RP) and a portable laser scanner (NextEngine). Fig 5.5 shows the setup of the devices during the experiment. Deformations of three different kidneys were scanned using a 1.5 Tesla MR machine with isotropic spatial resolution of 1.2 mm, and the collected data were used for training. Each deformation was generated randomly and remained static using a non-magnetic mechanical device during the MRI scanning, as shown in Fig 5.5(a). Deformations of the fourth kidney were imaged by both the laser scanner (of 0.38 mm resolution) and the ultrasound device as illustrated in Fig 5.5(b) and Fig 5.5(c). A 3D stepper motor positioning system was used to move the convex probe during ultrasound imaging.

Surfaces segmented from the MRI scans of the first three kidneys plus several randomly selected optical scans of the fourth kidney were used as the training data set. The remaining deformations of the fourth kidney were used for enhancement test. Specifically, we aim to reconstruct the complete deformable surfaces of the fourth kidney with resolution higher than the original ultrasound image. This is achieved by using the high resolution optical samples from a **single-side** view and lower resolution ultrasound samples from the area outside the view of the optical device. Those training surfaces from different kidneys were registered using iterative closest point method followed by the SH coefficient alignment as introduced in Chapter 4. Each surface consists of $N = 4002$ vertices and maximum SH degree involved in decomposition is $L = 20$. The result averaged over all the reconstructions

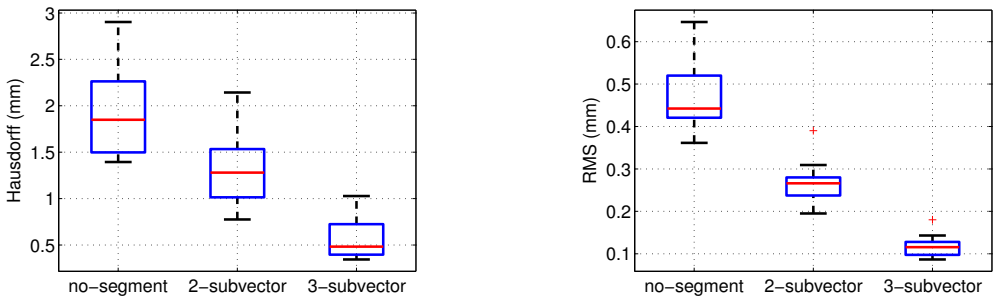

(a) (b)

Figure 5.6: Projection error using both non-segment and segmented training methods: (a) Hausdorff distance, (b) RMS distance.

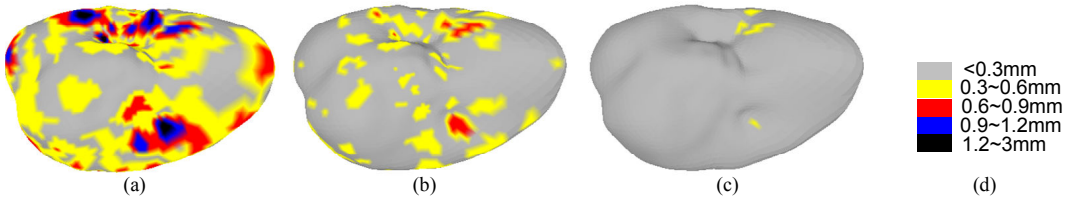

(a) (b) (c) (d)

Figure 5.7: Subspace projection example: (a) no-segment training, (b) 2-subvector training, (c) 3-subvector training, (d) color legend

is used for evaluation, in terms of Hausdorff and RMS distance. The former evaluates the maximum distance between the reconstructed surface and the ground truth, and the latter examines the mean error.

5.3.1 Projection Accuracy

Since how generalizable the identified subspaces are to the deformations beyond the training set is critical for accurate deformation reconstructions, the generalization of the structured dictionary from the training stage is first examined. This is evaluated as subspace projection errors of the surfaces to be reconstructed. The results using both traditional non-segmented training method and the proposed segmented training approach are provided for comparison.

The box plots in Fig. 5.6 and Table 5.1 illustrate the projection error in subspaces identified with non-segmented (left), two-subvector (middle) and three-subvector (right) training methods, respectively, in terms of Hausdorff distance and RMS error. Specifically,

Table 5.1: Projection error using both non-segment and segmented training methods

	(mm)	Min	Max	Mean	Std
Haus	No-segment	1.39	2.90	1.93	0.49
	2-subvector	0.78	2.14	1.34	0.48
	3-subvector	0.34	1.03	0.59	0.24
RMS	No-segment	0.36	0.65	0.48	0.1
	2-subvector	0.20	0.39	0.27	0.06
	3-subvector	0.09	0.18	0.12	0.03

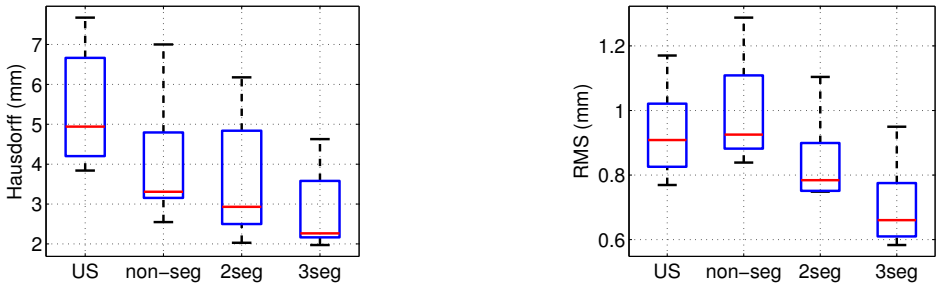

(a) (b)

Figure 5.8: Reconstruction error resulting from non-segmented and segmented training methods compared to the original ultrasound registration error: (a) Hausdorff distance, (b) RMS distance.

the projection errors as Hausdorff distance are 1.93 ± 0.49 mm, 1.34 ± 0.48 mm and 0.59 ± 0.24 mm with the three training strategies, with RMS of 0.48 ± 0.1 mm, 0.27 ± 0.06 mm and 0.12 ± 0.03 mm. Therefore, relative to the non-segmented training case, the three-subvector training significantly decreases the maximum error, from 2.90 mm to 1.03 mm, and achieves more than 1 mm improvement for the mean Hausdorff distance. Fig. 5.7 illustrates the color coded projection errors at each vertex under the three different training conditions. According to the color spread, we can see that the three-subvector training leads to the least error. For this particular example of deformation projection in Fig. 5.7, with the three-subvector training, the maximum projection error is reduced to 0.5 mm, as opposed to 2.4 mm in the non-segmented training case. Those results show that the segmented training method leads to better generalization of the deformation subspaces in the structured dictionary than that with the original non-segmented training method.

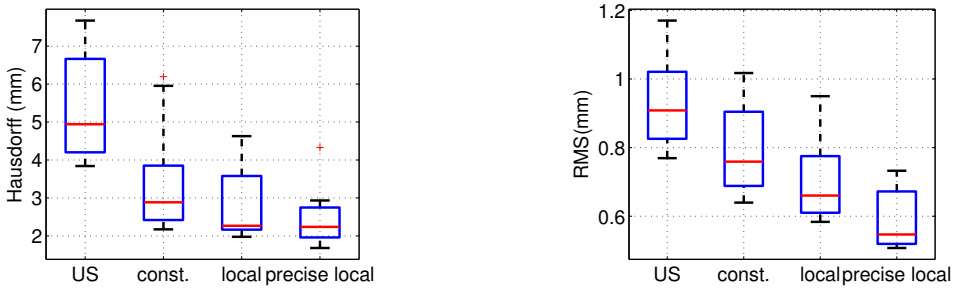

(a) (b)

Figure 5.9: Ultrasound registration error and reconstruction error under different weighting methods: (a) Hausdorff distance, (b) RMS distance.

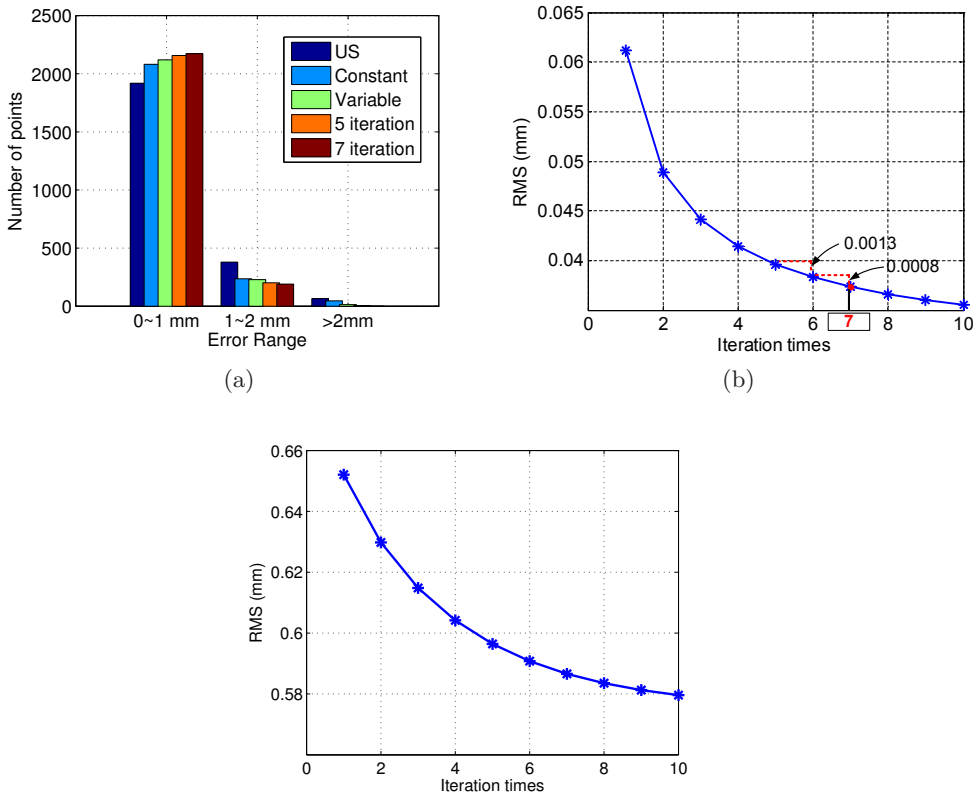

(a) (b)

(c)

Figure 5.10: (a) Error distribution of registered ultrasound and reconstruction under different iterations, (b) RMS reconstruction error on the side observable to optical device, indicating when the iteration stops, (c) RMS reconstruction error on the hidden side visible to ultrasound only.

5.3.2 Reconstruction Accuracy

The reconstruction error, particularly on the hidden side of the kidney that is only visible to the ultrasound device, is evaluated to examine the performance of the proposed enhancement method. We will demonstrate the contributions of the segmented training method and the weighting strategies to the final reconstruction precision.

5.3.2.1 Reconstruction with segmented training

Under the same weighting strategy, the two main factors affecting the reconstruction accuracy are the generalization of the subspaces learned from the training data set and the numerical stability during the operation of matrix pseudo inverse as shown in Eq.5.7. Since good subspace generalization contributes to a higher reconstruction accuracy, according to the projection error shown in Fig.5.6, it is expected to see that reconstruction using the segmented training method will outperform the non-segmented method if the problem is well conditioned. Due to the orthogonality of each subspace $\mathbf{\Phi}_\eta$, the condition number of the matrix in Eq. 5.7 is small, so numerical stability is achieved.

Table 5.2: Reconstruction error with non-segmented and segmented training methods

	(mm)	Min	Max	Mean	Std
Haus	US	3.84	7.68	5.30	1.40
	No-segment	2.54	7.00	4.06	1.53
	2-subvector	2.03	6.17	3.56	1.41
	3-subvector	1.97	4.62	2.78	0.94
RMS	US	0.77	1.17	0.94	0.13
	No-segment	0.84	1.28	1.00	0.17
	2-subvector	0.74	1.10	0.83	0.12
	3-subvector	0.58	0.94	0.70	0.12

Fig. 5.8 and Table 5.2 show the reconstruction accuracy under different training methods. The ultrasound image registration accuracy is also included as a baseline for comparison. As for mean Hausdorff distance, the reconstruction using three subvectors for training leads to the lowest error of 2.78 ± 0.94 mm as opposed to 4.06 ± 1.53 mm with the non-segmented training and 3.56 ± 1.41 mm with the two subvector training. The ultrasound

image registration error is 5.30 ± 1.40 mm. Particularly, the three subvector training case decreases the maximum error from 7.68 mm (ultrasound) to 4.62 mm. From the evaluation of RMS error, reconstruction using non-segmented training approach leads to an error of 1.00 ± 0.17 mm versus 0.94 ± 0.13 mm for the ultrasound images. Therefore, from the perspective of RMS error, the non-segmented training approach fails to improve the precision of the original ultrasound images. In contrast, the segmented training with two subvectors and three subvectors results in RMS distance of 0.83 ± 0.12 mm and 0.70 ± 0.12 mm, markedly lower than that of the ultrasound images. These results demonstrate that the segmented training method does outperform the non-segmented method due to its better generalization of the identified subspaces.

5.3.2.2 Reconstruction with different weighting methods

Three different weighting strategies were evaluated for reconstruction accuracy. The first strategy denoted as "const." in Fig. 5.9 and Table 5.3 applies constant weight $(\sigma_j^b)^2 = \sigma_{US}^2$ $(j = 1, \ ... \ m^b)$ for each ultrasound sample. The second strategy named as "local" estimates each local $(\sigma_j^b)^2$ as the average registration error between the ultrasound scans and the corresponding optical scans of the training surfaces, and the points with registration error larger than 1.5 mm were excluded from the ultrasound sample pool during reconstruction. The third case noted as "precise local" assumes that the ground truth is known and $(\sigma_j^b)^2$ is equal to the normalized error between the ultrasound coordinate and the true value at each vertex. The third strategy is not implementable in practice but it provides the low bound of the reconstruction error achievable by the proposed method. In the experiment, we set the maximum iteration time $N_{iter} = 10$, and the step improvement threshold $\rho = 0.001$ mm.

Fig. 5.9 and Table 5.3 demonstrate the reconstruction precision under the three different weighting strategies. The ultrasound registration error is provided as a baseline for comparison. In general, reconstruction using the weighted samples from different modalities

Table 5.3: Reconstruction error under different weighting methods

	(mm)	Min	Max	Mean	Std
Haus	US	3.84	7.68	5.30	1.40
	const.	2.17	6.19	3.41	1.55
	local	1.97	4.62	2.78	0.94
	precise local	1.68	4.33	2.49	0.79
RMS	US	0.77	1.17	0.94	0.13
	const.	0.64	1.02	0.80	0.13
	local	0.58	0.94	0.70	0.12
	precise local	0.51	0.73	0.59	0.09

can significantly enhance the ultrasound image resolution, and the advantage is better pronounced as more accurate weighting strategy is applied. Specifically, as shown in Fig. 5.9(a) and Table 5.3 in terms of Huasdorff distance, the second strategy based on "local" weights that are estimated from the training set results in an average error of 2.78 ± 0.94 mm, providing an improvement of 2.52 mm as opposed to the raw ultrasound imagery (5.30 ± 1.40 mm). Comparatively, the first constant weighting method leads to a higher error rate of 3.41 ± 1.55 mm, but still achieves an enhancement of 1.89 mm. The best achievable enhancement indicated by the error rate of the third "precise local" strategy is 2.49 ± 0.79 mm, close to the error rate of "local" weights. Similar trend is observed in the evaluation of RMS measurements as shown in Fig. 5.9(b) and Table 5.3. The "const.", "local" and "precise local" weighting strategies lead to RMS errors of 0.80 ± 0.13 mm, 0.70 ± 0.12 mm and 0.59 ± 0.09 mm, respectively, lower than the error of ultrasound images (0.94 ± 0.13 mm). Those results prove that the proposed approach can effectively improve the ultrasound image resolution by more than 2 mm and the empirical weights learned from the training data set are good estimates of the actual weights for fusing data from different modalities.

5.3.2.3 Effect of iterative correction

The advantage of the iterative enhancement procedure is demonstrated by comparing the reconstruction precision achieved with non-iterative and iterative approaches. The results

are shown in Fig. 5.10 and Fig. 5.11. Fig. 5.10(a) shows the distribution of point errors within three different ranges, considering the following five cases: (1) ultrasound registration, (2) reconstruction with constant weights, (3) non-iterative reconstruction with "local" weights, (4) reconstruction with "local" weights after five iterations and (5) reconstruction with "local" weights after seven iterations. We can see that, the original ultrasound images have the most large errors (above 1 mm) among the five cases, and more errors start to fall into the range of less than 1 mm as the iterative correction process takes effect. In particular, after seven iterations with the "local" weighting method, errors above 2 mm are eliminated on the reconstructed surface. Fig. 5.10(b) illustrates the evolving reconstruction error in terms of RMS distance under different number of iterations on the side observable to the optical device. As indicated in the figure, the step improvement between the 6^{th} and 7^{th} iteration is 0.0008 mm, below the threshold of 0.001 mm, so iteration in fact stops after the 7^{th} iteration, although the curve shows results till the 10^{th} iteration for complete illustration. Fig. 5.10(c) is the corresponding RMS distance of the reconstruction on the area observable to the ultrasound device only. Similarly, the error rate decreases and tends to slow down as iteration takes place. Fig. 5.11 provides the pictorial illustration of the iterative progress from the surface side that is unseen by the optical device. According to the color spread in the figure from the left to the right, we can see that the "local" weighting method is more effective than using constant weights, and the advantage is more pronounced as iteration goes on. After seven iterations, all the errors above 3 mm (in black) are corrected on this side area.

Fig. 5.12 shows a typical reconstructed deformation using the proposed enhancement method. Specifically, it compares the optical scan image (Fig. 5.12(a)) as ground truth, the corresponding 3D ultrasound image(Fig. 5.12(b)), and the reconstructed surface (Fig. 5.12(c)) on the side where optical samples are assumed to be unavailable during reconstruction. We can see that, in Fig. 5.12(c), details pointed by the arrows that are not shown in the original ultrasound image are clearly visible in the enhanced image. Fig. 5.12(d) and Fig. 5.12(e) provide the color-coded point errors of the registered ultrasound image and the reconstructed

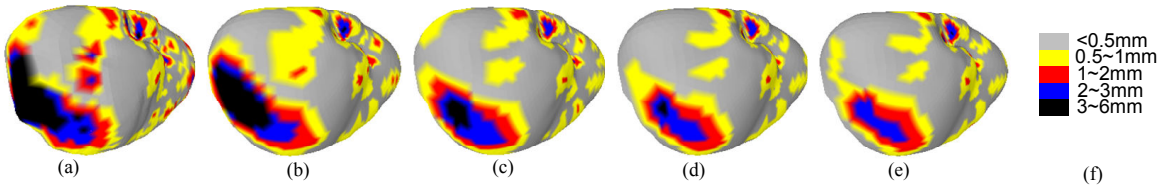

Figure 5.11: Reconstruction error with iterations:(a) Ultrasound registration, (b) Reconstruction using constant weights, (c) Reconstruction with "local" weights without iteration, (d) Reconstruction with "local" weights with 5 iterations, (e) Reconstruction with "local" weights with 7 iterations, (f) Color legend for the error.

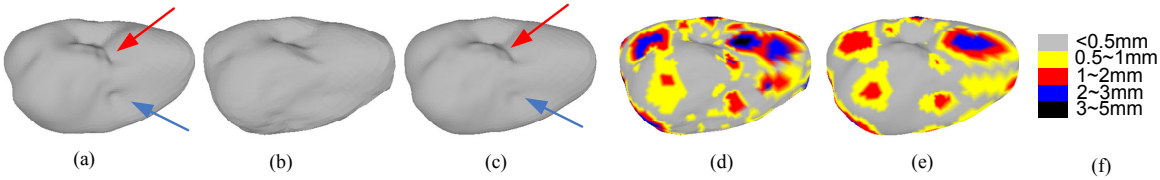

Figure 5.12: Reconstruction on the hidden side: (a) optical, (b) ultrasound, (c) reconstruction, (d) registration error of ultrasound, (e) error on the reconstructed surface, (f) color legend for the error.

surface from the side view. In this example reconstruction, 87% of errors above 3 mm on the hidden area (unobservable to the optical device) are removed by applying the proposed iterative approach.

5.4 Conclusion

This chapter presents a structured dictionary based approach of improving 3D intraoperative ultrasound image resolution. This is achieved by fusing the high resolution image patches with the lower resolution ultrasound samples. In this approach, the fine image samples are retrieved using a high precision imaging modality from a limited field of view and the ultrasound samples corresponds to the surface area that is unobservable to the high resolution device. The proposed segmented training method improves the generalization of the identified subspaces by taking into account the different significance levels of the SH coefficients. During the reconstruction process, samples are fused with proper weights considering the differences in resolution and noise levels between the different modalities. Ex-vivo experiment with freshly excised porcine kidneys using a 3D MRI machine, a 3D

ultrasound device and an optical scanner demonstrated that (1) the proposed segmented training method results in a higher reconstruction accuracy compared with the training approach proposed in Chapter 3.4; (2) the reconstruction method achieves an error of below 3 mm in terms of average Hausdorff distance, yielding a mean accuracy improvement of 2.52 mm compared to the ultrasound images; (3) the fusion strategy using "local" weights estimated as the registration error of the ultrasound images relative to the corresponding optical images in the training set is superior to that using constant weights in terms of higher reconstruction accuracy.

When applying the proposed method, one needs to be aware of the tradeoff between the number of sub-vectors used for segmented training and the efficiency of the reconstruction procedure. In general, the more the subvectors are involved in the training stage, the more computationally complex the reconstruction procedure will be due to larger subspace number and higher subspace dimension. Future work will be dedicated to extending the verification to the scenarios involving different organs and under both ex-vivo and in-vivo test conditions.

Chapter 6

Surgical Simulator

6.1 Chapter Introduction

Real time surgical simulation [159] has become an important tool in the field of surgery for operation planning, training of surgeons in the image-guided surgery or minimally invasive surgery, etc. The simulation tool is attractive because it avoids the use of patients for skill practice and ensures that trainees have had some practice before treating humans.

The techniques developed for surgical simulation have evolved quickly [160]. Most of of those methods fall into the following three categories. The first type is heuristic methods, including deformable splines [161], spring-mass models [162] and linked volume [163]. These methods usually integrate elastic properties and are simpler than alternatives like Finite Element Methods (FEM) at the cost of limited realism. The second category is based on the laws of continuum mechanics, including FEM [164] and boundary element methods (BEM) [165]. In practice, the ideal mechanical models have to be simplified significantly in order to obtain real-time performance. The third hybrid methods aim to combine the merits of the above two approaches. Based on the expected kind of interaction, the hybrid methods divide a deformable object into different sections, each of which is modeled with an appropriate model to increase the overall simulation efficiency.

Each of the aforementioned methods has its strengths and weaknesses in terms of computational cost, simulation realism and general applicability under various conditions. The currently widely used spring-mass model is superior to others from the perspective of simulation speed due to its simple mesh structure. Further, the mesh simplicity also allows for any topological manipulations like incisions. However, the drawbacks of spring-mass model are the slow global propagation of deformations and predisposition to oscillate during the iteration process. The continuum mechanic methods achieve more realism by sacrificing the computational speed. Although fast finite element (FFE) method and tensor precomputation method alleviate the computational burden by pre-computing the inversion of the stiffness matrix, they are limited to models with constant topologies so they don't accommodate the common procedures such as cutting or stitching. Regular FEM and BEM considering dynamic mesh structures are usually hampered by the large amount of computing capacity for massive matrix inversion, which prevents the implementation of real time simulation, especially when the element number of the topology is large. Recently, model reduction techniques [166][167] are proposed to achieve real time simulation by reducing the degree of freedom of the model. These methods, however, suffer from limited generalizability of the model.

Realizing the current challenges, this chapter proposes a new approach for real time surgical simulation by bringing in the merits of structured dictionary. It integrates the sparse surface representation algorithm in Chapter 3 into the traditional element based simulation model to reduce the computational cost.

6.2 Algorithm

The proposed algorithm applies the technique of structured surface representation into the traditional surface modeling approaches like mass-spring model. The goal is to reduce the number of surface vertices whose displacements in each iteration need to be updated by solving the ordinary differential equation (ODE). The majority of vertices' displacements are calculated by surface reconstruction in a best-fit subspace with efficiency higher than

ODE method.

Fig. 6.1 outlines the framework of the method. The flowchart in the upper rectangular illustrates the training procedures. Spherical harmonic representation (SHR) transforms the training data set into the harmonic domain where orthogonal subspace pursuit (OSP) method [121] is conducted to identify the subspaces to generalize the deformation model. Consequently, each surface x can be represented in the structured dictionary $\mathbf{G}$ with a block sparse vector c. The bottom part of Fig. 6.1 illustrates the real time simulation process. According to the trained subspaces, the sparse points are selected (red nodes), and displacements at those points are updated by the ODE solver. Deformations at other points (blue nodes) are reconstructed based on a surface reconstruction algorithm.

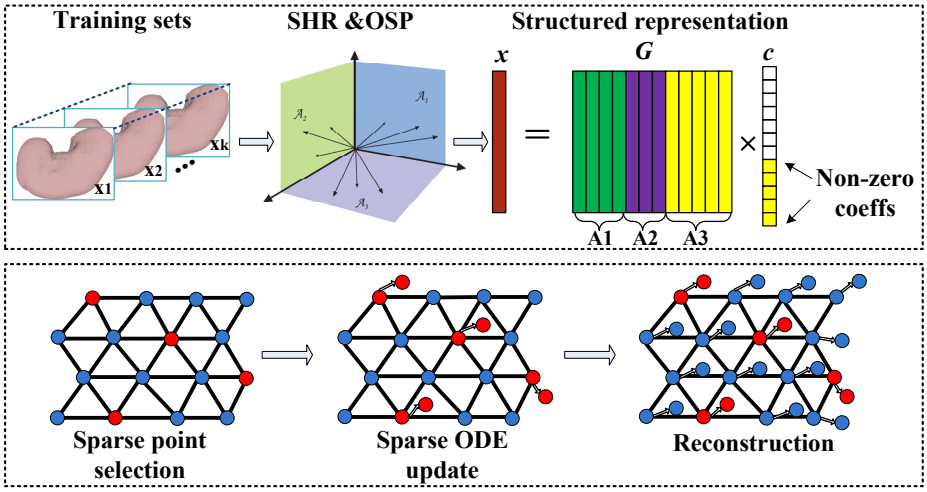

Figure 6.1: Framework of real time 3D surgical simulation based on structured dictionary.

6.2.1 Training

The main steps involved in the training stage are: (1) SHR to decrease the length of surface descriptor and filter out the high frequency noise for achieving better homology among the training surfaces; (2) OSP to identify the subspaces that can generalize the deformation to be simulated. The training data set can be obtained by running the traditional surgical simulator offline.

Suppose that there are K training surfaces, and each surface $\vec{x}_k$ $(1 \leq k \leq K)$ contains

N vertices. According to [146], each $\vec{x}_k$ can be expanded as

$$\vec{x}_k = \mathbf{Y}\vec{f}_k \tag{6.1}$$

where $\mathbf{Y}$ of size $N \times (L+1)^2$ denotes the SH basis matrix with L as the maximum harmonic degree, and $\vec{f}_k$ is the coefficient vector. Then K training frames can be characterized by $F = [\vec{f}_1 \ \vec{f}_2 \ ... \ \vec{f}_K]$ in the transformed harmonic domain.

OSP method is then applied to the set of coefficient vectors $\vec{f}_k$. If there are totally J subspaces identified from $\mathbf{F}$, a structured dictionary constructed by concatenating all deformation subspaces is established as $\mathbf{D} = \bigcup_{i=1}^{J}\{\mathbf{A}_i\}$, with dimension $I = \sum_{i=1}^{J} n_i$. Since each vector $\vec{f}_k$ lies in one of the subspaces, $\vec{f}_k$ can be represented in the structured dictionary with a block sparse vector $\tilde{\vec{c}}_k$. Consequently, $\mathbf{F}$ can be factorized as

$$\mathbf{F} \quad = \quad \mathbf{DC} \tag{6.2}$$

where $\mathbf{C} = \left| \begin{array}{cccc} \tilde{\vec{c}}_1 & \tilde{\vec{c}}_2 & \cdots & \tilde{\vec{c}}_K \end{array} \right|_{I \times K}$ is the corresponding coefficient matrix with block sparsity.

Integrating the above two steps, each deformation $\vec{x}_k$ can be sparsely represented in the original spatial domain as:

$$\vec{x}_k = \mathbf{YD}\tilde{\vec{c}}_k = \mathbf{G}\tilde{\vec{c}}_k = \mathbf{G}_i\vec{c}_k$$

where $\mathbf{G} = \mathbf{YD}$ with size of $N \times I$ is the desired structured dictionary in the spatial domain and $\vec{c}_k$ is the non-zero coefficients of $\tilde{\vec{c}}_k$. $\mathbf{G}$ is inherently structured by subspaces of $\mathbf{G} = \bigcup_{i=1}^{J}\{\mathbf{G}_i\}$ with $\mathbf{G}_i = \mathbf{YA}_i$ of size $N \times n_i$.

6.2.2 Real time simulation

After obtaining the subspaces to generalize the deformation model to be simulated, the real time simulation stage generates the dynamic deformation series based on the initial

condition that stimulates the model. Specifically, it includes the following three steps: sparse position selection, sparse ODE update and complete deformation reconstruction.

6.2.2.1 Sparse Position Selection

The first step during the real time simulation stage is to determine the surface point locations where displacements are updated with the ODE solver. This selection is only performed once before the real time simulation. The principle is to find a well conditioned sub-matrix $\widetilde{\mathbf{G}}_i$, such that the coefficient vector $\vec{c}$ can be stably estimated with the least square (LS) estimator from the following linear system

$$\widetilde{\vec{x}} \;=\; \widetilde{\mathbf{G}}_i \vec{c} \tag{6.2}$$

where $\widetilde{\vec{x}}$ is the m sparse surface samples (m must be larger than maximum n_i) and $\widetilde{\mathbf{G}}_i$ stands for the sub-matrix containing corresponding m rows of $\mathbf{G}_i$. More detailed description of how the sparse points are selected is provided in Chapter 4.2.2. $S = \{s_1, s_2, ..., s_m\}$ denotes the m indices of the selected points, highlighted as red nodes in Fig. 6.1. Notice that the surface index k is neglected in Eq. 6.2 for illustration convenience. As a result, the deformation $\vec{x}$ can be reconstructed completely in the proper subspace with estimated coefficients $\hat{\vec{c}}$.

6.2.2.2 Sparse ODE Update

The second step is to compute the displacements at those selected positions S. Without loss of generalization, the spring-mass model is applied in this chapter to illustrate how the efficiency of the simulation is improved using the structured dictionary. Each point (node) x^j $(1 \leq j \leq N)$ on surface $\vec{x}$ is connected to the direct neighbors with springs. According to the Newton's law of motion, the force equilibrium for each point j of the mesh can be established as

$$m^j \frac{d^2 x^j}{dt^2} + \gamma \frac{dx^j}{dt} + f^j_{int} = f^j_{ext} \tag{6.3}$$

where m^j is the mass of each node, x^j is the current coordinate, γ is the viscous friction coefficient, f^j_{ext} is the external force acting on node j, and f^j_{int} is the internal force trying to combat the external force and preserve the initial position. f^j_{int} is defined as

$$f^j_{int} = \Sigma_{n\in\Gamma_j} k^j_n \frac{|x^n - x^j| - |l^j_n|^0}{|x^n - x^j|}(x^n - x^j) \tag{6.4}$$

where Γ_j is the indices of neighbors of x^j, k^j_n evaluates the rigidity of the spring between the nodes n and j, and $|l^j_n|^0$ is the natural length of the spring.

The set of differential equations are solved by a discretization of time into small intervals ∇t, typically with finite Euler differences. In order to converge, the stiffer the simulated object is intended to be, the smaller the ∇t needs to be. Explicit Euler difference is applied in this thesis. Specifically, the following equations are applied on each point for numerical integration.

$$\begin{aligned} f^j_t &= m^j \times a^j_t \\ v^j_t &= \nabla t \times a^j_t + v^j_{t-1} \\ x^j_t &= \nabla t \times v^j_t + x^j_{t-1} \end{aligned} \tag{6.5}$$

where f^j_t, a^j_t, v^j_t and x^j_t are the overall force, acceleration, velocity and coordinate of point j at time step t. The simulation model is driven by setting up the initial value of forces at certain nodes. Other numerical approach such as RungeKutta that permits the selection of a greater time step ∇t can also be applied for more efficiency. For simplicity, explicit Euler method is implemented in this thesis.

With the traditional spring-mass simulation method, the set of ODE for all nodes is solved by the numerical approach at each time step. In our proposed method, ODE update at each iteration is involved only at the selected nodes indexed by S. Deformations at other nodes are estimated by reconstructing the complete deformation in the best-fit subspace, as detailed in the next step.

6.2.2.3 Complete Deformation Reconstruction

The updated coordinates at the selected sparse nodes are the input to the complete deformation reconstruction. Considering the time factor during the simulation course, the linear system in Eq. 6.2 at time step $t+1$ is written as

$$\widetilde{\vec{x}}^{\,t+1} = \widetilde{\mathbf{G}}_i \vec{c}^{\,t+1} \tag{6.4}$$

Since the selection of sparse position S ensures the above linear system is well-conditioned, the equation system can be solved by applying the LS constraint. The remaining question is to determine the best-fit subspace for reconstruction. This is achieved by evaluating the reconstruction error at positions indexed by S in each subspace and choosing the subspace with the least reconstruction error as the best-fit subspace. Mathematically, the best-fit subspace i^* is selected by

$$i^* = \min_{1 \le i \le J} (\|\widetilde{\vec{x}}^{\,t+1} - \widetilde{\mathbf{G}}_i \hat{\vec{c}}^{\,t+1}\|_2) \tag{6.5}$$

Finally, the complete deformation is reconstructed as

$$\widehat{\vec{x}}^{\,t+1} = \mathbf{G}_{i^*} \widehat{\vec{c}}^{\,t+1} \tag{6.6}$$

To summarize the proposed algorithm, the sequential steps are further outlined as follows.

- *Step0:* Initialization: $t = 0$, $\vec{x} = \vec{x_0}$, set f_{ext}^j at designated nodes with initial values;
- *Step1:* t=t+1, compute $\widetilde{\vec{x}}^{\,t+1}$ at selected position S according to previous $\vec{x}^{\,t}$ with ODE solver;
- *Step2:* Reconstruct $\widehat{\vec{x}}^{\,t+1}$ with the structured dictionary;
- *Step3:* Replace $\widehat{\vec{x}}^{\,t+1}$ at locations indexed by S with known values $\widetilde{\vec{x}}^{\,t+1}$;
- *Step4:* Go back to Step1 until iteration is terminated.

6.3 Evaluation

To verify the feasibility of the proposed approach, we implemented the algorithm in MATLAB. Initially, a porcine kidney model is segmented from a set of 3D magnetic resonance images with isotropic spatial resolution of 1.2 mm. The maximum spherical harmonic level L is set as 30, and number of vertices N is 4002. The simulation accuracy is evaluated in terms of Hausdorff distance and $EOF = ||\hat{\vec{x}} - \vec{x}||_2/||\vec{x}||_2$ as the normalized Euclidean distance between the estimated surface relative to the ground truth. The simulated deformations generated by the traditional spring-mass model with the same initial condition and parameters are used as the ground truth for comparison.

6.3.1 Subspace Generalization

Since the generalization of the identified subspaces indicated by the representation precision of the surfaces to be simulated is critical for high accuracy simulation, the subspace projection error is first evaluated. There are five subspaces on X and Y axes respectively, and three subspaces on Z axis, with maximum subspace size of 100. Note that, the low dimensionality of the trained subspace enables fast deformation simulation. The upper subplot in Fig. 6.2 shows the projection error in terms of EOF, and the bottom plot corresponds to the Hausdorff distance. Specifically, the average EOF error is $0.82\% \pm 0.39\%$ and the Hausdorff distance is 0.25 ± 0.11mm. This low error rate demonstrates the good generalization of the

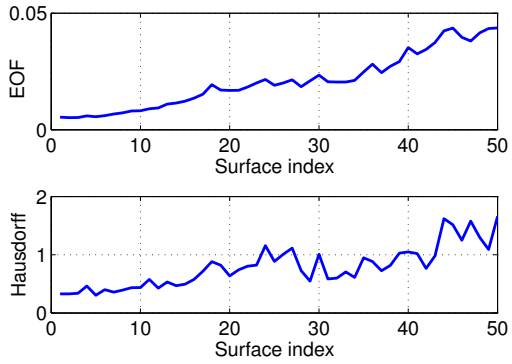

Figure 6.2: Projection error in terms of EOF and Huasdorff distance.

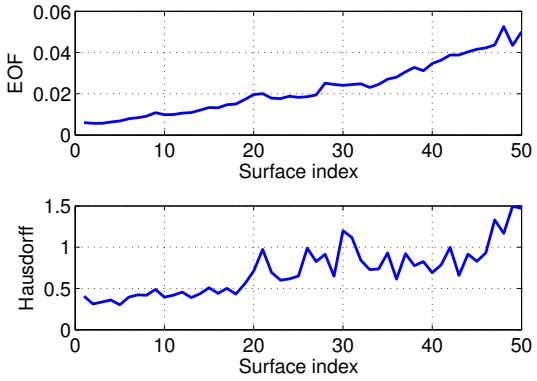

Figure 6.3: Simulation error in terms of EOF and Huasdorff distance.

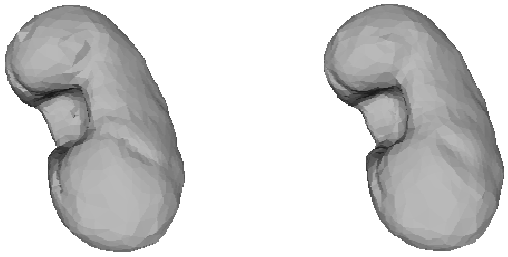

Figure 6.4: Example of ODE generated deformation (left) and corresponding simulated deformation using the proposed method.

subspaces in the structured dictionary to the deformations to be simulated.

6.3.2 Simulation Accuracy

The simulated deformations generated using the proposed method is compared with the corresponding surfaces simulated with the traditional spring-mass model. Similarly, the upper subplot in Fig. 6.3 shows the simulation error in terms of EOF, and the bottom plot demonstrates the Hausdorff distance. The X axis corresponds to the surface indices as time evolves. The average EOF error is $2.3\% \pm 1.3\%$ with a maximum error of 5.3% and the Hausdorff distance is 0.71 ± 0.30mm with a maximum error of 1.50mm. Fig. 6.4 provides an example of the deformation generated by the traditional ODE model (left) and the corresponding simulated deformation using the proposed method (right). We can see that the two surfaces are very similar. These experiment results demonstrate that the accuracy of the proposed simulation algorithm is close to that of the mass-spring model.

6.3.3 Simulation Accuracy with Periodic Correction

From Fig. 6.3, we can see an increasing error as simulation takes place. This is because the reconstruction error at each time step accumulates and propagates to the next step. Ideally, the simulation generated using our proposed method should be corrected periodically to decrease the error. Fig. 6.5 and Fig. 6.6 show the simulation error with periodic correction. Specifically, the simulated frames are corrected every 10 deformations in Fig. 6.5 and every 20 deformations in Fig. 6.6 using the corresponding surface generated with the traditional model. From these two figures, we observe that the simulation error is effectively brought down with the correction to prevent error overaccumulation. Although realizing the necessity of periodic correction, we are still investigating this issue.

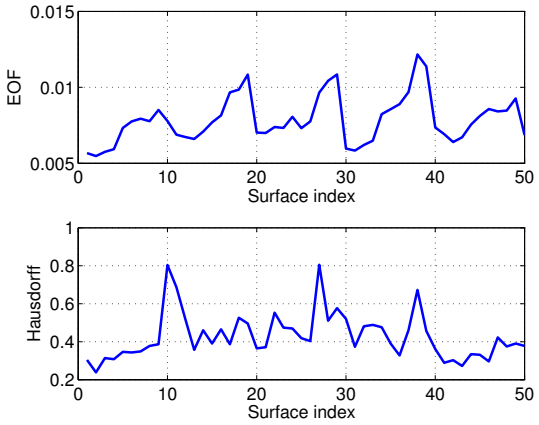

Figure 6.5: Simulation error in terms of EOF and Huasdorff distance with periodic correction every 10 frames.

6.4 Discussion

This chapter proposed an algorithm of real time 3D surgical simulation of deformable organs. It applies the technique of structured surface representation to achieve high simulation efficiency by reducing the computational cost involved in the regular ODE solver. Majority of the deformation is estimated by surface reconstruction in the best-fit subspace. The experimental results demonstrated the feasibility of the method. It achieves an accuracy

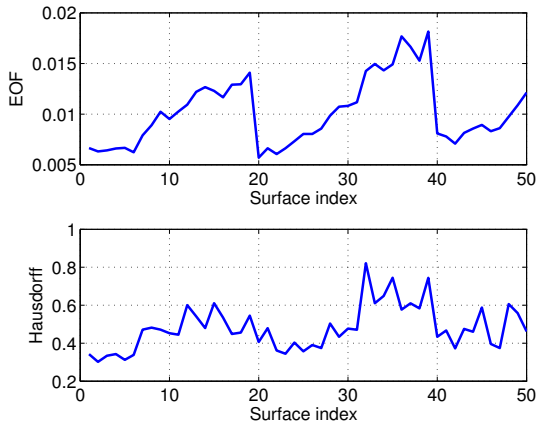

Figure 6.6: Simulation error in terms of EOF and Huasdorff distance with periodic correction every 20 frames.

of less than 2mm in terms of Hausdorff distance. The remaining challenge of the proposed method is the error propagation issue as shown in the preliminary results.

Chapter 7

Conclusion

7.1 Summary

The work presented in the preceding chapters has concentrated on investigating new ideas and techniques for enhancing the visualization quality of surgeons performing image-guided interventions by reconstructing the complete organ deformations during the surgery. The main contributions of this thesis can be summarized as follows.

- In Chapter 3, we introduced an algorithm for block sparse representation of deformable organ surfaces. The proposed SRDS design first identifies the deformation subspaces from the training data set in the transformed spherical harmonic domain, and then represents each deformed surface with a block sparse vector in the structured dictionary. SRDS is generalized to applications involving organs with multiple surface layers, such as bladder. SRDS serves as the foundation for the next three contributions.

- Chapter 4 presents a new approach for real-time 3D visualization of organ deformations based on optical imaging patches with limited field of view and a single preoperative MRI or CT scan. This approach aims to provide surgeons with real-time 3D visualization of complete organ deformations with high accuracy. The idea for

reconstruction is motivated by the SRDS theory introduced in Chapter. 3, which indicates that the spherical harmonic coefficients corresponding to distorted surfaces of a given organ lie in lower dimensional subspaces in a structured dictionary that can be learned from a set of representative training surfaces. The preoperative MRI or CT scan is used for registration and dictionary building, while the intraoperative optical patch images from limited views are used for real-time deformation reconstruction based on the trained dictionary. Evaluation with FEM data and ex-vivo experiments demonstrated that the design achieves real-time 3D reconstruction of organ deformations with spatial resolution better than $3mm$ in terms of Hausdorff distance. This algorithm has the potential to reconstruct the interior structure of the organ by only sampling the exterior surface sparsely.

- Chapter 5 presented a structured dictionary based approach of improving 3D intraoperative ultrasound image resolution. This is achieved by fusing the high resolution image patches with the lower resolution ultrasound samples. In this approach, the fine image samples are retrieved using a high precision imaging modality from a limited field of view and the ultrasound samples correspond to the surface area that is unobservable to the high resolution device. The proposed segmented training method improves the generalization of the identified subspaces by taking into account the different significance levels of the SH coefficients. During the reconstruction process, samples are fused with proper weights considering the differences in resolution and noise levels between the different modalities. Ex-vivo experiment with freshly excised porcine kidneys using a 3D MRI machine, a 3D ultrasound device and an optical scanner demonstrated that the reconstruction method achieves an error of below 3 mm in terms of average Hausdorff distance, yielding a mean accuracy improvement of 2.52 mm compared to the ultrasound images.

- Chapter 6 proposes an efficient algorithm for real-time surgical simulation. This

method relies on the structured surface representation technique to improve the simulation efficiency by reducing the computational cost involved in the traditional ODE-based approach. Specifically, only nodes at sparse locations are deformed by the ODE solver, and majority of the deformation is estimated by surface reconstruction in the best-fit subspace. The preliminary experimental results demonstrate the feasibility of the method. It achieves an accuracy of less than 2mm in terms of Hausdorff distance.

7.2 Future Work

The preliminary research of this project has shown promising advantages in tests using both synthetic data and real ex-vivo experiment. As part of future work, we would like to investigate further from the following perspectives.

7.2.1 Training and Refining

The proposed sparse representation approach relies on the use of a training dictionary that captures the deformation variability of the organ to be considered. Consequently, a key question is to determine the size of the training data set needed to ensure that a universal dictionary, not refined for a specific subject, will yield the desired reconstruction accuracy when applied to a subject that is not in the training data set.

To this aim, we will develop and compare strategies that identify subspaces to capture the deformation variations from the limited data. We will also study the distribution of the representation coefficients in the subspaces identified. If the coefficients cluster in well defined patterns, the patterns can be further exploited to enhance reconstruction accuracy, particularly in the presence of noisy data. At the level of implementation and training data selection, we will compare training based on (1) detailed 3D computer models that account for organ mechanical and physical properties, and (2) training based on CT scans of organs coming from different animals and subjected to different deformations that are kept static during CT scanning.

If a universal dictionary is not obtainable, the procedure of refining dictionary has to be considered. In particular, insufflation and a sequence of minimally invasive static interventions would be needed to deform the organs and acquire CT scans of the deformed organs prior to live surgery. If training on the actual subject is found to be necessary, we will identify and characterize the minimal number of organ deformations that are needed to refine the dictionary.

Furthermore, we want to test the generalization of the subspaces that are learned from the training on ex-vivo organs. Specifically, we will check whether the interactions between organs alters the identified subspaces during the in-vivo operation.

7.2.2 Surface Correspondence and Registration

Based on the preliminary experiments, we learned that some steps in the design remain to be improved, especially in the area of surface correspondence and registration.

For surface correspondence, the goal is to match vertices across different deformations to achieve better homology during the training stage. The currently employed method aligns the spherical harmonic coefficients in the transformed domain so that the ridges of the first order ellipsoid coincide. Evidently, the correspondence of surfaces with rotational symmetry in the first order ellipsoid is ambiguously defined. According to the evaluation in [157], both Minimum Description Length (MDL) [148] and covariance determinant (DetCov) outperform the spherical method with more robust pixel-wise correspondence. We are in the process of implementing MDL approach for more evaluations.

As far as registration is concerned, we will study the sensitivity of the reconstruction accuracy to small variations in the positions and orientations of the 3D scanner. Further, in the experiment, the laser scanner is relatively fixed in the physical space. Apparently, freely moving the scanner can impose more challenge for real-time registration, so we will also consider this issue in the future experiment.

7.2.3 Assessment in In-vivo Experiments

The clinical aspects of this project include two phases, with the first phase using ex-vivo models for bench top testing and analysis as shown in the preliminary experiments, and the second phase taking place in the animal surgical suite.

During the in-vivo test, live animals will be utilized to test the proposed 3D visualization technique in an operating room setting. Specifically, we will conduct randomized study to compare the imaging properties of the proposed 3D system with laparoscopic ultrasound utilizing porcine models. Animals will be injected with gelatin lesions into the right lobe, the left lobe and a mid portion of the liver with imaging guidance. CT images of the lesions will be taken for each animal after injection. Lesions will then be randomly assigned to resection under the proposed 3D imaging guidance or laparoscopic ultrasound guidance, and the margins will be assessed by a pathologist who is blind to the group assignments. Margins ¿ 1 mm on the formaldehyde fixated mass will be regarded as negative (R0 resection). Then we compare the number of R0 resections using the proposed 3D imaging guidance with that using the laparoscopic ultrasound guidance. If the proposed system leads to a 10% difference in negative margins over the laparoscopic ultrasound guidance, we will claim that significant improvement is achieved in the in-vivo experiments. The sample size needed for the study is based on the requirement for McNemar's test for correlated proportions.

Bibliography

[1] D. Rattner, A. Kalloo, Surgery, "ASGE/SAGES Working Group on Natural Orifice Transluminal Endoscopic Surgery", Surgical Endoscopy, vol.63(2), pp.329-333, 2006.

[2] G.W. Fischer, R. Garcia-Villanueva, A. C. Anyanwu, and D. H. Adams, "Multimodal Sonographic Approach for Assessing Left Ventricular Outflow Tract Gradient", Journal of the American Society of Echocardiography, vol. 22(7), pp. 864.e1-864.e3, 2009.

[3] Y. Matsumura, T. Hozumi, K. Arai, K. Sugioka, et. al, "Non-invasive assessment of myocardial ischaemia using new real-time three-dimensional dobutamine stress echocardiography: comparison with conventional two-dimensional methods", Eur Heart J, vol. 26(16), pp. 1625C1632, 2005

[4] D. Maulik, N. C. Nanda, V. Singh, H. Dod, et. al, "Live three-dimensional echocardiography of the human fetus", Echocardiography - A Journal of Cardiovascular Ultrasound and Allied Techniques, vol. 20(8), pp. 715C721, 2003

[5] R. S. von Bardeleben, H. P. Kuhl, S. Mohr-Kahaly, A. Franke, "Second-generation real-time threedimensional echocardiography - Finally on its way into clinical cardiology", Zeitschrift Fur Kardiologie, vol. 93(Suppl. 4), pp. 56C64, 2004

[6] J. Shen, E.S. Ebbini, "Filter-based coded-excitation system for high-speed ultrasonic imaging", IEEE Transaction on Medical Imaging, vol. 17(6), pp. 923C934, 1998

[7] J. Harms, H. Feussner, M. Baumgartner, A. Schneider, M. Donhauser, and G. Wessels, "Three-dimensional navigated laparoscopic ultrasonography: first experiences with a

new minimally invasive diagnostic device", Surg Endosc, vol.15(12), pp.1459-1462, Dec 2001.

[8] M. Nakamoto, H. Hirayama, Y. Sato, K. Konishi, Y. Kakeji, M. Hashizume, and S. Tamura, "Recovery of respiratory motion and deformation of the liver using laparoscopic freehand 3d ultrasound system", Med Image Anal, vol.11(5), pp.429-442, Oct 2007.

[9] S. Beller, M. Hnerbein, S. Eulenstein, et al., "Feasibility of navigated resection of liver tumors using multiplanar visualization of intraoperative 3D ultrasound data", Annals of Surgery, vol.246(2), pp.288-294, 2007.

[10] Masahiko N., Yoshinobu S., Masaki M., et al., "3D Ultrasound System Using a Magneto-optic Hybrid Tracker for Augmented Reality Visualization in Laparoscopic Liver Surgery", Medical Image Computing and Computer-Assisted Intervention (MICCAI), pp.148-155, 2002.

[11] P. Hildebrand, M. Kleemann, U. J. Roblick, L. Mirow, C. Burk, H. P. Bruch, "Technical aspects and feasibility of laparoscopic ultrasound navigation in radiofrequency ablation of unresectable hepatic malignancies", J Laparoendosc Adv Surg Tech A, vol.17(1), pp.53-57, 2007.

[12] P. Bao, T. K. Sinha, C. C. Chen, J. R. Warmath, et al., "A prototype ultrasound-guided laparoscopic radiofrequency ablation system", Surg Endosc, vol.21(1), pp.74-79, 2007.

[13] Huang, X., et al., "Dynamic 3D ultrasound and MR image registration of the beating heart", Med Image Comput Comput Assist Interv, vol.8(2), pp.171-178, 2005.

[14] Linte, C., et al. "An augmented reality environment for image-guidance of off-pump mitral valve implantation", San Diego, CA, USA: SPIE, 2007.

[15] M. Handke, G. Heinrichs, U. Moser, F. Hirt, F. Margadant, et al., "Transesophageal real-time three-dimensional echocardiography methods and initial in vitro and human in vivo studies", J Am Coll Cardiol, vol.48(10), pp.2070-2076, 2006.

[16] S.G. Yuen, S.B. Kesner, N.V. Vasilyev, P.J. Del Nido, R.D. Howe, "3D ultrasound-guided motion compensation system for beating heart mitral valve repair", Med. Image Comput. Comput. Assist. Interv. pp.711-719, 2008.

[17] S. Ghofrani, M. R. Jahed-Motlagh, A. Ayatollahi, "An adaptive speckle suppression filter based on Nakagami distribution", EUROCON'2001, International Conference on Trends in Communications , vol. 81, pp. 84-87, 2001

[18] V. Dutt, J. F. Greenleaf, "Adaptive speckle reduction filter for log-compressed B-scan images", IEEE Transactions on Medical Imaging, vol. 15(6), pp. 802-813, 1996

[19] T. Loupas, W. N. McDicken, P. L. Allan, "An adaptive weighted median filter for speckle suppression in medical ultrasonic images", IEEE Transactions on Circuits and Systems, vol. 36, pp. 129-135, 1989

[20] A. Lopes, R. Touzi, E Nezry, "Adaptive speckle filters and scene heterogeneity", IEEE Transactions on Geoscience and Remote Sensing , vol. 28, pp. 992-1000, 1990

[21] I. M. Johnstone, B. W. Silverman, "Wavelet Threshold Estimators for Data with Correlated Noise", Journal of the Royal Statistical Society. Series B (Methodological), vol. 59, pp. 319-351, 1997

[22] J. C. Lazaro, J. L. San Emeterio, A. Ramos, J. L. Fernadez-Marron, "Influence of thresholding procedures in ultrasonic grain noise reduction using wavelets", Ultrasonics, vol. 40, pp. 263-267, 2002

[23] E. Pardo, J. L. San Emeterio, M. A. Rodriguez, A. Ramos, "Noise reduction in ultrasonic NDT using undecimated wavelet transforms", Ultrasonics, vol. 44, pp. 1063-1067, 2006

[24] A. Abbate, J. Koay, J. Frankel, S. C. Schroeder, P. Das, "Signal detection and noise suppression using a wavelet transform signal processor: application to ultrasonic flaw detection", IEEE Transactions on Ultrasonics, Ferroelectrics and Frequency Control, vol. 44, pp. 14-26, 1997

[25] P. Renbin, C. Hao, P. K. Varshney, J. H Michels, "Stochastic resonance: An approach for enhanced medical image processing", Life Science Systems and Applications Workshop, 2007.

[26] V. P. Rallabandi, "Enhancement of ultrasound images using stochastic resonance-based wavelet transform", Computerized Medical Imaging and Graphics, vol. 32, pp. 316-320, 2008.

[27] K. Kihara, S. Kawakami, Y. Fujii, H. Masuda, F. Koga, "Gasless single-port access endoscopic surgery in urology: minimum incision endoscopic surgery, MIES ", Int J Urol, vol.16(10), pp.791-800, 2009.

[28] O. A. Chiesa, J. von Bredow, H. Li, and M. Smith, "Isobaric (gasless) laparoscopic liver and kidney biopsy in standing steers", Can J Vet Res, vol.73(1), pp.42-48, 2009.

[29] C. D. Choi, A. R. Skovoroda, S. Y. Emelianov, M. O'Donnell, "An integrated compliant balloon ultrasound catheter for intravascular strain imaging", IEEE Trans Ultrason Ferroelectr Freq Control, vol.49(11), pp.1552-1560, 2002.

[30] F. Contijoch, L. F.-d.-M., Tri Ngo, et al., "Increasing Temporal Resolution of 3D Transesophageal Ultrasound by Rigid Body Registration of Sequential Temporally Offset Sequences", IEEE International Symposium on Biomedical Imaging (ISBI), pp.328-331, 2010.

[31] W. Wein, S. Brunke, A. Khamene, M.R. Callstrom, N. Navab, "Automatic CT-ultrasound registration for diagnostic imaging and image-guided intervention", Med Image Anal, vol.12(5), pp.577-585, 2008.

[32] P. Bao, J. Warmath, R. Galloway, and A. Herline, "Ultrasound-tocomputer-tomography registration for image-guided laparoscopic liver surgery", Surg Endosc, vol. 19(3), pp.424-429, Mar 2005.

[33] A. J. Herline, J. L. Herring, J. D. Stefansic, W. C. Chapman, R. L. Galloway, and B. M. Dawant, "Surface registration for use in interactive, image-guided liver surgery", Comput Aided Surg, vol.5(1), pp.11-17, 2000.

[34] F.A. Jolesz, "Future perspectives for intraoperative MRI", Neurosurg Clin N Am, vol.16(1), pp.201-213, 2005.

[35] D. Gering, A. Nabavi,R. Kikinis, et al., "An Integrated Visualization System for Surgical Planning and Guidance Using Image Fusion and an Open MR", Journal of Magnetic Resonance Imaging, 2001

[36] J. Lesniak, J. Tokuda, R. Kikinis, et al., "A device guidance method for organ motion compensation in MRI-guided therapy", Physics in Medicine and Biology, 2007

[37] J. Tokuda, M, Hirano, T. Tsukamoto, T. Dohi and N. Hata, "Real-Time Organ Motion Tracking and Fast Image Registration System for MRI-Guided Surgery", Systems and Computers in Japan, 37(1), 2006

[38] M. Baumhauer, M. Feuerstein, H. P. Meinzer, J. Rassweiler, "Navigation in endoscopic soft tissue surgery: perspectives and limitations", J Endourol, vol.22(4), pp.751-766, 2008.

[39] Rassweiler, J., M. Baumhauer, U. Weickert, H.P. Meinzer, et al., "The role of imaging and navigation for natural orifice translumenal endoscopic surgery", J Endourol, vol.23(5), pp.793-802, 2009.

[40] G. Coughlin, S. Samavedi, K.J. Palmer, V.R. Patel, "Role of image-guidance systems during NOTES", J Endourol, vol.23(5), pp.803-812, 2009.

[41] V. Karimyan, M. Sodergrena, J. Clarka, G.Z. Yangb, A. Darzia, "Navigation systems and platforms in natural orifice translumenal endoscopic surgery (NOTES)", Int J Surg, vol.7(4), pp.297-304, 2009.

[42] T. C. Poon, and R. N. Rohling, "Comparison of calibration methods for spatial tracking of a 3-D ultrasound probe", Ultrasound Med Biol, vol.31(8), pp.1095-108, 2005.

[43] M. Feuerstein, T. Reichl, J. Vogel, J. Traub, and N. Navab, "Magneto-Optical Tracking of Flexible Laparoscopic Ultrasound: Model-Based Online Detection and Correction of Magnetic Tracking Errors", IEEE Transactions on Medical Imaging, vol.28(6), pp.951-967, 2009.

[44] C. Rickers, M. Jerosch-Herold, X. Hu, N. Murthy, X. Wang, et al., "Magnetic resonance image-guided transcatheter closure of atrial septal defects", Circulation, vol.107, pp.132-138, 2003.

[45] C. L. Truwit, W. A. Hall, "Intraoperative magnetic resonance imaging-guided neurosurgery at 3-T", Neurosurgery, vol.58(4), pp.338-345, 2006.

[46] S. Mittal, P. M. Black, "Intraoperative magnetic resonance imaging in neurosurgery: the Brigham concept", Acta Neurochir, vol.98, pp.77-86, 2006.

[47] T. Yasunaga, K. Konishi, S. Yamaguchi, et al., "Mr-compatible laparoscope with a distally mounted ccd for mr imageguided surgery," International Journal of Computer Assisted Radiology and Surgery, vol.2, pp.11-18, 2007.

[48] N. Foroglou, A. Zamani, P. Black, "Intra-operative MRI (iop-MR) for brain tumour surgery", British Journal of Neurosurgery, vol.23(1), pp.14-22, 2009.

[49] J. Tokuda, S. Morikawa, H. A. Haque, et al., "New 4-D Imaging for Real-Time Intraoperative MRI: Adaptive 4-D Scan", International Conference on Medical Image Computing and Computer-assisted Intervention, pp.454-61, 2006.

[50] J. Kettenbach, T. Wong, D. Kacher, et al., "Computer-based imaging and interventional MRI: applications for neurosurgery", Comput. Med. Imaging Graph, vol.23, pp.245-258, 1999.

[51] N. Foroglou, A. Zamani, P. Black, "Intra-operative MRI (iop-MR) for brain tumour surgery", Br. J. Neurosurg, vol.23, pp.14-22, 2000.

[52] J. H. Siewerdsen, D. J. Moseley, S. Burch, S. K. Bisland, A. Bogaards, B. C.Wilson, and D. A. Jaffray, "Volume CT with a flat-panel detector on a mobile, isocentric c-arm: Pre-clinical investigation in guidance of minimally invasive surgery", Med. Phys., vol.32(1), pp.241-254, 2005.

[53] M. Feuerstein, T. Mussack, S. M. Heining, and N. Navab, "Intraoperative laparoscope augmentation for port placement and resection planning in minimally invasive liver resection", IEEE Transactions on Medical Imaging, vol.27(3), pp.355-369, 2008.

[54] N. Navab, S.M. Heining, J. Traub, "Camera AugmentedMobile C-arm (CAMC): calibration, accuracy study and clinical applications", IEEE Trans. Med. Imaging, vol.29(7), pp. 1412-1423, 2010.

[55] M. Kranzfelder, M. Dobritz, D. Wilhelm, et al., "CT-navigated real-time ultrasonography: evaluation of registration accuracy for clinical application", Biomedical Engineering, vol.53(6), pp.279-84, 2008.

[56] T. Lange, S. Eulenstein, M. Hunerbein, H. Lamecker, P.M. Schlag, "Augmenting intraoperative 3D ultrasound with preoperative models for navigation in liver surgery", In: Proc. MICCAI, pp.534-541, 2004.

[57] R.M. Comeau, A.F. Sadikot, A. Fenster, T.M. Peters, "Intraoperative ultrasound for guidance and tissue shift correction in image-guided neurosurgery", Med. Phys., vol.27, pp.787-800, 2000.

[58] D. Gobbi, B. Lee, T.M. Peters,“ Correlation of pre-operative MRI and intra-operative 3D ultrasound to measure brain tissue shift”, Proc. SPIE, vol.4319, pp.264-271, 2001.

[59] I. Reinertsen, M. Descoteaux, K. Siddiqi, D.L. Collins, “Validation of vessel-based registration for correction of brain shift”, Med. Image Anal., vol.11, pp.374-388, 2007.

[60] K.S. Rhode, M. Sermesant, D. Brogan, S. Hegde, J. Hipwell, et al., “A system for real-time XMR guided cardiovascular intervention”, IEEE Trans. Med. Imaging, vol.24, pp.1428-1440, 2005.

[61] J.A. Bracken, P. Komljenovic, P.V. Lillaney, R. Fahrig, J.A. Rowlands, “Closed-bore XMR (CBXMR) systems for aortic valve replacement: x-ray tube imaging performance”, Med. Phys. vol.36, pp.1086-1097, 2009.

[62] L. Brzozowski, A. Ganguly, M. Pop, Z. Wen, R. Bennett, et al., “Compatibility of interventional x-ray and magnetic resonance imaging: feasibility of a closed bore XMR (CBXMR) system”, Med. Phys., vol.33, pp.3033-3045, 2006.

[63] F. A. Jolesz, N. McDannold, “Current Status and Future Potential of MRI-Guided Focused Ultrasound Surgery”, Journal of Magnetic Resonance Imaging, vol.27, pp.391-399, 2008.

[64] B. Senneville, C. Mougenot, C. T. W. Moonen, “Real-time adaptive methods for treatment of mobile organs by MRI-controlled high-intensity focused ultrasound”, Magnetic Resonance in Medicine, vol.57(2), pp.319-330, 2007.

[65] M. Ferrant, A. Nabavi, B. Macq, F.A. Jolesz, R. Kikinis, S.K. Warfield, “Registration of 3-D intraoperative MR images of the brain using a finite-element biomechanical model”, IEEE Trans Med Imaging, vol.20, pp.1384-1397, 2001.

[66] S.K. Warfield, F. Talos, A. Tei, A. Bharatha, A. Nabavi, M. Ferrant, et al., “Real-time registration of volumetric brain MRI by biomechanical simulation of deformation during image guided neurosurgery”, Comput Visual Sci, vol.5, pp.3C11, 2002.

[67] A. Hagemann, K. Rohr, H.S. Stiehl, U. Spetzger, J.M. Gilsbach, "Biomechanical modeling of the human head for physically based, nonrigid image registration", IEEE Trans Med Imaging, vol.18, pp875-884, 1999.

[68] K.D. Paulsen, M.I. Miga, F.E. Kennedy, P.J. Hoopes, A. Hartov, D.W. Roberts, "A computational model for tracking subsurface tissue deformation during stereotactic neurosurgery", IEEE Trans Biomed Eng., vol.46, pp.213-225, 1999.

[69] M.I. Miga, K.D. Paulsen, P.J. Hoopes, F.E. Kennedy, A. Hartov, D.W. Roberts, "In vivo quantification of a homogeneous brain deformation model for updating preoperative images during surgery", IEEE Trans Biomed Eng., vol.47, pp.266-273, 2000.

[70] T. J. Carter, M. Sermesant, D. M. Cash, D. C. Barratt, C. Tanner, and D. J. Hawkes, "Application of soft tissue modelling to image-guided surgery", Med Eng Phys, vol.27(10), pp.893-909, Dec 2005.

[71] H. Huang, R. Zhang, R. Makedon, et al., "A Spatio-Temporal Modeling Method for Shape Representation", 3D Data Processing, 3DPVT, pp.1034-1040, 2006.

[72] H. Timinger, S. Krueger, J. Borgert, and R. Grewer, "Motion compensationfor interventional navigation on 3d static roadmaps based on an affine model and gating", Phys Med Biol, vol.49(5), pp.719-732, Mar 2004.

[73] T. Ortmaier, M. Groger, D.H. Boehm, V. Falk, G. Hirzinger, "Motion estimation in beating heart surgery", IEEE Trans Biomed Eng, vol.52(10), pp.1729-1740, 2005.

[74] A. Hostettler, S. Nicolau, C. Forest, et al., "Real Time Simulation of Organ Motions Induced by Breathing: First Evaluation on Patient Data", Biomedical Simulation, pp.9-18, 2006.

[75] J. Tanga, S. Dieterichb, K. Clearya, "Respiratory Motion Tracking of Skin and Liver in Swine for CyberKnife Motion Compensation", Proc. SPIE 5367, 729, 2004.

[76] K. Mori, D. Deguchi, T. Kitasaka, Y. Suenaga, et al., "Bronchoscope tracking based on image registration using multiple initial starting points estimated by motion prediction", Med Image Comput Comput Assist Interv, vol.9, pp.645-652, 2006.

[77] O. Skrinjar, A. Nabavi, and J. Duncan, "Model-driven brain shift compensation", Med Image Anal, vol.6(4), pp.361-373, Dec 2002.

[78] D. M. Cash, M. I. Miga, S. C. Glasgow, B. M. Dawant, L. W. Clements, Z. Cao, R. L. Galloway, and W. C. Chapman, "Concepts and preliminary data toward the realization of image-guided liver surgery", J Gastrointest Surg, vol.11(7), pp.844-859, Jul 2007.

[79] D. M. Cash, M. I. Miga, T. K. Sinha, R. L. Galloway, and W. C. Chapman, "Compensating for intraoperative soft-tissue deformations using incomplete surface data and finite elements", IEEE Trans Med Imaging, vol.24(11), pp.1479-1491, Nov 2005.

[80] Rassweiler, J., et al., "The role of imaging and navigation for natural orifice translumenal endoscopic surgery", J Endourol, vol.23(5), pp.793-802, 2009.

[81] Coughlin, G., et al., "Role of image-guidance systems during NOTES", J Endourol, vol.23(5), pp.803-12, 2009.

[82] Karimyan, V., et al., "Navigation systems and platforms in natural orifice translumenal endoscopic surgery (NOTES)", Int J Surg, vol.7(4), pp.297-304, 2009.

[83] M. Lustig, D. Donoho, and J. Pauly, "Sparse MRI: The application of compressed sensing for rapid MR imaging", Magnetic Resonance in Medicine, vol.58(6), pp.1182-1195, 2007.

[84] G.L. Xu, Q. Zhang, "A general framework for surface modeling using geometric partial differential equations", Computer Aided Geometris Design, vol.25(3), pp.181-202, 2008.

[85] G. Zeng, S. Paris, L. Quan, Francois Sillion, "Accurate and Scalable Surface Representation and Reconstruction from Images", IEEE Transaction on Pattern Analysis and Machine Intelligence, vol.29(1), pp.141 158, 2007.

[86] A. Matheny, D. B. Goldgof, “The use of three- and four-dimensional surface harmonics for rigid and nonrigid shape recovery and representation”, IEEE Transaction on Pattern Analysis and Machine Intelligence, vol.17(10), pp.967-981, 1995.

[87] C. W. Chen, T. S. Huang, M. Arrott, ”Modeling, Analysis, and Visualization of Left Ventricle Shape and Motion by Hierarchical Decomposition”, IEEE Transaction on Pattern Analysis and Machine Intelligence, vol.16(4), pp.342-356, 1994.

[88] J. L. Dillenseger, H. Guillaume, J. J. Patard, “Spherical Harmonics Based Intrasubject 3-D Kidney Modeling/Registration Technique Applied on Partial Information”, IEEE Transactions on Biomedical Engineering, vol.53(11), pp.2185-193, 2006.

[89] M. K. Chung, K. M. Dalton, L. Shen, A.C. Evans, R.J. Davidson, “Weighted Fourier Series Representation and Its Application to Quantifying the Amount of Gray Matter”, IEEE Transactions on Medical Imaging, vol.26(4), pp.566-581, 2007.

[90] M. K. Chung, K. M. Dalton, R. J. Davidson, “Tensor-Based Cortical Surface Morphometry via Weighted Spherical Harmonic Representation”, IEEE Transactions on Medical Imaging, vol.27(8), pp.1143-1151, 2008.

[91] Ch. Brechbhler, G. Gerig, O. Kbler, “Parametrization of Closed Surfaces for 3-D Shape Description”, Computer Vision and Image Understanding, vol.61(2), pp.154-170, 1995.

[92] L. Shen, F. Makedon, “Spherical mapping for processing of 3D closed surfaces”, Image and Vision Computing, vol.24(7), pp.743-761, 2006.

[93] X.F. Gu, Y.L. Wang, T.F. Chan, P. Thompson, S.T. Yau, “Genus Zero Surface Conformal Mapping and Its Application to Brain Surface Mapping”, IEEE Transaction on Medical Imaging, vol.23(8), pp.949-958, 2004.

[94] A. Gelb,“The resolution of the gibbs phenomenon for spherical harmonics”, Mathematics of Computation, vol.66, pp.699-717, 1997.

[95] L. Shen, M. K. Chung, "Large-Scale Modeling of Parametric Surfaces using Spherical Harmonics", International Symposium on 3D Data Processing, Visualization and Transmission, 2006.

[96] H. Huang, L. Shen, J. Ford, F. Makedon, L. Gao, J. Pearlman, "Functional Analysis of Cardiac MR Images Using SPHARM Modeling", Image Processing, Proceedings of SPIE, 2005.

[97] H. Huang, R. Zhang, F. Makedon, L. Shen, J. Pearlman, "Spatio-Temporal Modeling Method for Shape Representation", International Symposium on 3D Data Processing, Visualization, and Transmission, pp.1034-1040, 2006.

[98] H. Huang, L. Zhang, D. Samaras, L. Shen, R. Zhang, F. Makedon, J. Pearlman, "Hemispherical Harmonic Surface Description and Applications to Medical Image Analysis", International Symposium on 3D Data Processing, Visualization, and Transmission, pp.381-388, 2006.

[99] H. Huang, L. Shen, R. Zhang, F. Makedon, B. Hettleman,J. Pearlman, "Surface Alignment of 3D Spherical Harmonic Models: Application to Cardiac MRI Analysis", Medical Image Computing and Computer Assisted Intervtion, pp.67-74, 2005.

[100] A. Makadia, K. Daniilidis, "Rotation Recovery from Spherical Images without Correspondences", IEEE Transaction on Pattern Analysis and Machine Intelligence, vol.28(7), pp.1170-1175, 2006.

[101] M. Kazhdan, "An Approximate and Efficient Method for Optimal Rotation Alignment of 3D Models", IEEE Transaction on Pattern Analysis and Machine Intelligence, vol.29(7), pp.1221-1229, 2007.

[102] H. Huang, F. Makedon, J. Ford, L. Shen, Y. Wang, T. Steinberg, "Efficient Similarity Retrieval for Temporal Shape Sequences: A Case Study using Cardiac MR Images", IEEE Conference of Engineering in Medicine and Biology Society, pp.3250-3253, 2004.

[103] D. Chen, X. Tian, Y. Shen, M. Ouhyoung, "On Visual Similarity Based 3D Model Retrieval", Computer Graphics Forum, pp.223-232, 2003.

[104] T. Funkhouser, P. Min, M. Kazhdan, J. Chen, A. Halderman, D. Dobkin, "A Search Engine for 3D Models", ACM Transactions on Graphics, vol.22, pp.83-105, 2003.

[105] K. T. Rajamania, M. A. Stynerb, H. Taliba, G. Y. Zheng, L. P. Noltea, M. A. Ballester, "Statistical deformable bone models for robust 3D surface extrapolation from sparse data ", Medical Image Analysis, vol.11, pp.99-109, 2007.

[106] C. Basso, T. Vetter, "Statistically Motivated 3D Faces Reconstruction", The 2nd International Conference on Reconstruction of Soft Facial Parts, Remagen, Germany, 2005.

[107] J. Feng, H.s. Ip, "A multi-resolution statistical deformable model (MISTO) for soft-tissue organ reconstruction", Journal of Pattern Recognition, vol.42, pp.1543-1558, 2009.

[108] T. Albrecht, R. Knothe, T. Vetter, "Modeling the Remaining Flexibility of Partially Fixed Statistical Shape Models", Workshop on the Mathematical Foundations of Computational Anatomy, USA, 2008.

[109] G. Y. Zheng, S. Gollmerb, S. Schumanna, X. Dong, T. Feilkasb, M. A. G. Ballester, "A 2D/3D correspondence building method for reconstruction of a patient-specific 3D bone surface model using point distribution models and calibrated X-ray images ", Medical Image Analysis, vol.13, pp.883-899, 2009.

[110] B. K. Natarajan, "Sparse approximate solutions to linear systems", SIAM J. Comput., vol.24(2), pp.227-234, 1995.

[111] G. Davis, S. Mallat, and M. Avellaneda, "Greedy adaptive approximation", J. Constr. Approx., vol.13, pp.57-98, 1997.

[112] P. J. Huber. "Projection pursuit", The Annals of Statistics, vol.13(2), pp.435-475, 1985.

[113] R. DeVore and V. Temlyakov, "Some remarks on greedy algorithms", Advances in Computational Mathematics, vol.5(1), pp.173-187, 12 1996.

[114] S. Mallat, G. Davis, and Z. Zhang, "Adaptive time-frequency decompositions", SPIE Journal of Optical Engineering, vol.33, pp.2183C2191, 1994.

[115] Y. C. Pati, R. Rezaifar, and P. S. Krishnaprasad, "Orthogonal matching pursuit: recursive function approximation with applications to wavelet decomposition", in 27th Asilomar Conf. on Signals, Systems and Comput., 1993.

[116] S. Chen, S. A. Billings, and W. Luo, "Orthogonal least squares methods and their application to non-linear system identification", International Journal of Control, vol.50(5), pp.1873C1896, 1989.

[117] S. Chen, C. Cowan, P. Grant, "Orthogonal least squares learning algorithm for radial basis function networks", IEEE Transactions on In Neural Networks, vol.2(2), pp.302-309, 1991.

[118] S. Chen and D. Donoho, "Atomic decomposition by basis pursuit", SIAM Journal on Scientific Computing, vol.20(1), pp.33-61, 1998.

[119] I.F. Gorodnitsky and B.D. Rao, "Sparse signal reconstruction from limited data using focuss: a re-weighted minimum norm algorithm", Signal Processing, IEEE Transactions on, vol.45(3), pp.600-616, 1997.

[120] T. Blumensath and M.E. Davies, "Gradient pursuits", Signal Processing, IEEE Transactions on, vol.56(6), pp.2370-2382, 2008.

[121] B. V. Gowreesunker, A. H. Tewfik, "Learning Sparse Representation Using Iterative Subspace Identification", IEEE Transactions on Signal Processing, vol.58(6), pp.3055-3065, 2010.

[122] B. A. Olshausen and D. J. Field, "Sparse coding with an overcomplete basis set: A strategy employed by v1", Vision Research, vol.37, pp.3311-3325, 1998.

[123] K. Engan, S. O. Aase, and J. H. Husy, "Multi-frame compression: Theory and design", EURASIP Signal Process, vol.80, pp.2121-2140, 2000.

[124] J. F. Murray and K. Kreutz-Delgado, "An improved focuss-based learning algorithm for solving sparse linear inverse problems", In Conference Record of the 35rd Asilomar Conference on Signals, Systems and Computers, 2001.

[125] M. Aharon, M. Elad, A. Bruckstein, "The k-svd: An algorithm for designing of over-complete dictionaries for sparse representation", IEEE Transaction on Signal Processing, vol.54(11), pp.4311-4322, 2006.

[126] Y.C. Eldar, P. Kuppinger and H. Bolcskei, "Block-Sparse Signals: Uncertainty Relations and Efficient Recovery", Signal Processing, IEEE Transactions on, vol.58(6), pp.3042-3054, 2010.

[127] Y. C. Eldar, "Uncertainty relations for shift-invariant analog signals", IEEE Trans. Inf. Theory, vol.55(12), pp.5742C5757, 2009.

[128] B.L. Sturm, J.J. Shynk, and S. Gauglitz, "Agglomerative clustering in sparse atomic decompositions of audio signals", In Acoustics, Speech and Signal Processing, IEEE International Conference on, pp.97-100, 2008.

[129] F. Parvaresh, H. Vikalo, S. Misra, and B. Hassibi, "Recovering sparse signals using sparse measurement matrices in compressed DNA microarrays", IEEE J. Sel. Topics Signal Process., vol.2(3), pp.275-285, Jun. 2008.

[130] M. Mishali and Y. C. Eldar, "Blind multi-band signal reconstruction: Compressed sensing for analog signals", IEEE Trans. Signal Process., vol.57(3), pp.993-1009, 2009.

[131] M. Mishali and Y. C. Eldar, "Reduce and boost: Recovering arbitrary sets of jointly sparse vectors", IEEE Trans. Signal Process., vol.56(10), pp.4692-4702, Oct. 2008.

[132] Y. C. Eldar and H. Rauhut, Average case analysis of multichannel sparse recovery using convex relaxation, IEEE Trans. Inf. Theory, vol.56(1), pp.505-519, Jan. 2010.

[133] M. Elad and M. Aharon, "Image Denoising Via Learned Dictionaries and Sparse representation", Computer Vision and Pattern Recognition, 2006 IEEE Computer Society Conference on, pp.895 - 900, 2006.

[134] M. Zibulevsky, B. A. Pearlmutter, "Blind Source Separation by Sparse Decomposition in a Signal Dictionary", Neural Computation, vol.13, pp.863-882, 2000.

[135] D.L. Donoho, "Compressed Sensing", Manuscript, September 2004.

[136] M. Mahmoudi and G. Sapiro, "Sparse Representation For Three-dimenstional Range Data Restoration", IMA, 2009.

[137] H. Tang, Y.F. Sun, B.C. Yin and Y. Ge, "3D face recognition based on sparse representation", The Journal of Supercomputing, vol.58(1), pp.84-95, 2011.

[138] X. Li, T. Jia, H. Zhang, "Expression-insensitive 3d face recognition using sparse representation", Proc of computer vision and pattern recognition, pp.2575-2582, 2009.

[139] J. Davis, S.R. Marschner, M. Garr, M. Levoy, "Filling Holes in Complex Surfaces using Volumetric Diffusion", 3D Data Processing, Visualization, and Transmission, 2002.

[140] M. Pauly, N.J. Mitra, J. Giesen, et al., "Example-Based 3D Scan Completion", Symposium on Geometry Processing, 2005.

[141] D. Wang, A. H. Tewfik, "Sparse Representation of Deformable Organs", IEEE International Symposium on Biomedical Imaging (ISBI), pp.887-890, 2009.

[142] D. Wang, A.H. Tewfik, "In Vivo Tracking of 3D Organs Using Spherical Harmonics and Subspace Clustering", IEEE International Conference on Image Processing, pp.817-820, 2009 .

[143] D. Wang, A. H. Tewfik, "Real-time Tracking of Exterior and Interior Organ Surfaces Using Sparse Sampling of the Exterior Surfaces", International Conference on Acoustics, Speech and Signal Processing, pp.1022-1025, 2010.

[144] D. Wang, A. H. Tewfik, "Real Time Tracking of 3D Organ Surfaces Using Single MR Image and Limited Optical Viewing", IEEE International Symposium on Biomedical Imaging (ISBI), pp.620-623, 2010.

[145] D. Wang, A. Casper, A. H. Tewfik, E. S. Ebbini, "Enhanced ultrasound imaging resolution with 3D optical patch imagery", IEEE International Symposium on Biomedical Imaging (ISBI), pp.21-24, 2011.

[146] D. Wang, A. H. Tewfik, Y. Zhang, and Y. Shen, "Sparse Representation of Deformable 3D Organs with Spherical Harmonics and Structured Dictionary, International Journal of Biomedical Imaging, 2011.

[147] D. Wang and A. H. Tewfik, "Real Time 3D Visualization of Intra-operative Organ Deformations Using Structured Dictionary", IEEE Transaction on Medical Imaging, 2012.(to appear)

[148] R.H. Davies, C.J. Twining, T.F. Cootes, J.C. Waterton, C.J. Taylor, "A minimum description length approach to statistical shape modeling", IEEE Transactions on Medical Imaging, vol.21(5), pp.525-537, 2002.

[149] P.J. Besl, N.D. McKay, "A method for registration of 3-D shapes", IEEE Transaction on Pattern Analysis and Machine Intelligence, vol.14(2), pp.239-256, 1992.

[150] L. Shen, H. Farid, M.A. McPeek, "Modeling Three-Dimentional Morphological Structures Using Spherical Harmonics", Journal of Organic Evolution, vol.63(4), pp.1003-1016, 2009.

[151] L. Najman, J. Cousty, M. Couprie, H. Talbot, S. Clment-Guinaudeau, T. Goissen, J. Garot, "An open, clinically validated database of 3d+t cine-mr images of the left ventricle with associated manual and automated segmentations", Insight Journal, special issue entitled ISC/NA-MIC Workshop on Open Science, 2007.

[152] D. Lowe, "Distinctive image features from scale-invariant keypoints", International Journal of Computer Vision, vol.2(60), pp.91-110, 2004.

[153] B. Ginneken, T. Heimann, and M. Styner, "3D Segmentation in the Clinic: A Grand Challenge", MICCAI Workshop, pp.7-15, 2007.

[154] T.P. Rauth, P.Q. Bao, R.L. Galloway, J. Bieszczad, et al., "Laparoscopic surface scanning and subsurface targeting: implications for image-guided laparoscopic liver surgery", Surgery, vol.142(2), pp.207-214, 2007.

[155] M. Hayashibe, N. Suzuki, Y. Nakamura, "Laser-scan endoscope system for intraoperative geometry acquisition and surgical robot safety management", Medical Image Analysis, pp.509-519, 2006.

[156] http://www.hpl.washington.edu/research/sfep/.

[157] M. A. Styner, K. T. Rajamani, L. Nolte, et al., "Evaluation of 3d correspondence methods for model building", Information Processing in Medical Imaging, vol.2732, pp.62-75, 2003.

[158] Y. Shen, X. Zhou, N. Zhang, K. Tamma, and R. Sweet, "Realistic Soft Tissue Deformation Strategies for Real Time Surgery Simulation", Studies in Health Technology and Informatics, vol.132, pp.457-459, 2008.

[159] S. Cotin, H. Delingette, N. Ayache, "Real-time elastic deformations of soft tissues for surgery simulation", IEEE Transactions on Visualization and Computer Graphics, vol.5(1), pp.62-73, 1999.

[160] U. Meier, O. Lopez, C. Monserrat, M.C. Juan, M. Alcaniz, "Real-time deformable models for surgery simulation: a survey", Computer Methods and Programs in Biomedicine, vol.77, pp.183-197, 2005.

[161] D. Terzopoulos, et al., "Elastically deformable models", Comput.Graph, vol.21(4), pp.205-214, 1987.

[162] Y. Lee, D. Terzopoulos, K. Waters, "Realistic modeling for facial animation", Comput. Graph., vol.29(1), pp.55-62, 1995.

[163] S.F.F. Gibson, "Using linked volumes to model object collisions, deformation, cutting, carving, and joining", IEEE Trans. Visualization Comput. Graph. vol.5(4), pp.333-348, 1999.

[164] M. Bro-Nielsen, "Finite Element Modelling in Surgical Simulation", Proc. IEEE, vol.86(3), pp.490-503, 1998.

[165] C. Monserrat, U. Meier, M. Alcaniz, F. Chinesta, M.C. Juan, "A new approach for the real-time simulation of tissue deformations in surgery simulation", Comp. Meth. Progr. Biomed., pp.77-85, 2001.

[166] S. Niroomandia, I. Alfaroa, E. Cuetoa, F. Chinestab, "Real-time deformable models of non-linear tissues by model reduction techniques", Computer Methods and Programs in Biomedicine, vol.91(3), pp. 223-231, 2008.

[167] C. Audouze, F. De Vuyst, P. B. Nair, "Reduced-order modeling of parameterized PDEs using time-pace-parameter principal component analysis", Int. J. Numer. Meth. Engng, vol.80, pp.1025C1057, 2009.

Appendix A

Kernel Matlab Code for Schemes in LBC Evaluation

In this part, we list some key code for the implemmentation of connectivity based localizatoin algorithms. Three funtions are recorded in the following that cover the aspects of MDS calculation, coordinate rotation and scaling (uniform), and the LS used in DV-Hop (and many of the other scenarios).

A.1 MDS Calculation

A.2 Coordinate Rotation and Scaling

A.3 DV-Hop LS